

SHAPE MEMORY ALLOY ACTUATOR
FOR CROSS-FEED IN TURNING
OPERATION

T. OTIENO

2012

SHAPE MEMORY ALLOY ACTUATOR FOR CROSS-FEED IN
TURNING OPERATION

By

Timothy Otieno

Submitted in fulfilment of the requirements for the degree of
Masters: Engineering in the Faculty of Engineering, the Built
Environment and Information Technology at the Nelson Mandela
Metropolitan University

January 2012

Promoter/Supervisor: Prof. Khaled Abou-El-Hossein

Acknowledgments

Particular thanks to the Technology Innovation Agency / Department of Science and Technology of South Africa for the financial help to obtain the materials for the work and Prof. K. Abou-El-Hossein for his guidance and support throughout the work.

Declaration

I, Timothy Otieno, student number 206035139, hereby declares that the dissertation for MEng Mechatronics is my own work and that it has not previously been submitted for assessment or completion of any postgraduate qualification to another University or for another qualification.

Timothy Otieno

Table of Contents

	Page
Abstract.....	xi
Chapter 1. Introduction	1
1.1 Background.....	1
1.2 Shape Memory Alloys.....	2
1.3 Problem Statement	3
1.4 Objective	3
1.5 Scope	4
1.6 Methodology.....	4
1.7 Structure.....	5
Chapter 2. Literature Review.....	6
2.1 Shape Memory Alloy Functions	6
2.2 Thermal Cycle	7
2.3 Material Composition.....	9
2.4 Shape Memory Alloy Actuators	10
2.5 Design Considerations for Shape Memory Alloy Actuator Wires	20
2.6 Heating and Cooling	22
2.7 Modelling and Control	24
2.8 Metal Cutting.....	29

Chapter 3. Design and Development.....	34
3.1 Design Requirements	34
3.2 Forces in Aluminium Turning	35
3.3 Wire Selection	36
3.4 Wire Bundle.....	38
3.5 Stroke	40
3.6 Cycle Rate	40
3.7 Bias Force	41
3.8 Power Supply.....	43
3.9 Control Method.....	44
3.10 Switching Circuit	46
3.11 Sensors.....	46
3.12 Data Acquisition.....	47
3.13 Software.....	49
3.14 Forced Cooling	49
3.15 Physical Structure	49
3.16 Actuator Control System	53
Chapter 4. Experiments and Testing.....	56
4.1 Test Stand.....	56
4.2 Experimental Setup	57

4.3	Safety and Operation	65
Chapter 5.	Results and Discussions	69
5.1	Test Stand.....	69
5.2	Open Loop Experiments.....	70
5.2.1	Maximum Stroke Tests	70
5.2.2	Forced Cooling Tests	79
5.2.3	Radial Force Tests	90
5.3	Closed Loop Experiments.....	92
5.3.1	Controlled Position Tests	92
5.3.2	Steady-State Position Errors	99
5.4	Recommended Operating Parameters	101
Chapter 6.	Conclusions	104
References	107
Appendix A:	Labview Programs	113
Appendix B:	Drawings	116
Appendix C:	Finite Element Analysis Report.....	126

List of Figures

	Page
Figure 2.1: SMA thermo-mechanical hysteresis between martensite and austenite [7]	8
Figure 2.2: Bias force mechanisms [1]	11
Figure 2.3: Two-way SMA actuator [10]	12
Figure 2.4: Hydraulic valve SMA actuator [11]	12
Figure 2.5: Starsys Research and APL mini-actuator [12]	13
Figure 2.6: Antagonistic SMA linear actuator [13]	13
Figure 2.7: SMA beam actuator [14]	14
Figure 2.8: SMA mirror actuator prototype [15]	15
Figure 2.9: SMA drive system [16]	15
Figure 2.10: Positioning actuator prototype [17]	16
Figure 2.11: MigaOne linear SMA actuator [18]	17
Figure 2.12: SMA tool clamp [19]	18
Figure 2.13: Power/weight ratio vs. weight of different actuators. Schematic representation of power density as a function of weight for the most common actuator technologies [2] ..	19
Figure 2.14: Change of critical phase temperatures with stress [5]	27
Figure 2.15: Control system model	29
Figure 2.16: Cutting force components	30
Figure 3.1: Stabilus Lift-O-Mat gas spring [49]	42
Figure 3.2: Actuator control system	45
Figure 3.3: MOSFET switching circuit	46
Figure 3.4: National Instruments DAQ hardware	48

Figure 3.5: Actuator concept design	50
Figure 3.6: Actuator final design	51
Figure 3.7: FEA applied forces and constraints.....	52
Figure 3.8: FEA analysis of actuator shaft.....	53
Figure 3.9: Actuator system block diagram	54
Figure 3.10: Actuator system circuit diagram.....	55
Figure 4.1: Test stand setup.....	56
Figure 4.2: Actuator setup	58
Figure 4.3: Experimental setup	59
Figure 4.4: Labview open loop front panel	61
Figure 4.5: Force experiment setup.....	62
Figure 4.6: Labview closed loop front panel	63
Figure 4.7: Labview PID autotuning wizard	64
Figure 4.8: Labelled user front panel	66
Figure 5.1: Test stand temperature with time.....	69
Figure 5.2: 3V temperature with time	70
Figure 5.3: 3V displacement with time	71
Figure 5.4: 3V displacement with temperature.....	71
Figure 5.5: 5V temperature with time	72
Figure 5.6: 5V displacement with time	72
Figure 5.7: 5V displacement with temperature.....	73
Figure 5.8: 7V temperature with time	74
Figure 5.9: 7V displacement with time	74
Figure 5.10: 7V displacement with temperature.....	75

Figure 5.11: 9V temperature with time	76
Figure 5.12: 9V displacement with time	76
Figure 5.13: 9V displacement with temperature.....	77
Figure 5.14: 3V, 5V, 7V, 9V temperature with time comparison	77
Figure 5.15: 3V, 5V, 7V, 9V displacement with time comparison	78
Figure 5.16: 3V, 5V, 7V, 9V displacement with temperature comparison	78
Figure 5.17: 3V cooling temperature with time	80
Figure 5.18: 3V cooling displacement with time	81
Figure 5.19: 3V cooling displacement with temperature	81
Figure 5.20: 5V cooling temperature with time	82
Figure 5.21: 5V cooling displacement with time	82
Figure 5.22: 5V cooling displacement with temperature	83
Figure 5.23: 7V cooling temperature with time	84
Figure 5.24: 7V cooling displacement with time	84
Figure 5.25: 7V cooling displacement with temperature	85
Figure 5.26: 9V cooling temperature with time	86
Figure 5.27: 9V cooling displacement with time	86
Figure 5.28: 9V cooling displacement with temperature	87
Figure 5.29: 3V, 5V, 7V, 9V cooling temperature with time	88
Figure 5.30: 3V, 5V, 7V, 9V cooling displacement with time	88
Figure 5.31: 3V, 5V, 7V, 9V cooling displacement with temperature	89
Figure 5.32: Temperature with time for radial forces	90
Figure 5.33: Displacement with time for radial forces	91
Figure 5.34: Displacement with temperature for radial forces	91

Figure 5.35: 3V displacement response with time	93
Figure 5.36: 5V displacement response with time	94
Figure 5.37: 7V displacement response with time	95
Figure 5.38: 9V displacement response with time	96
Figure 5.39: 1mm 3V, 5V, 7V, 9V displacement with time	97
Figure 5.40: 2mm 3V, 5V, 7V, 9V displacement with time	97
Figure 5.41: 3mm 3V, 5V, 7V, 9V displacement with time	98
Figure 5.42: 4mm 3V, 5V, 7V, 9V displacement with time	98
Figure 5.43: 5mm 3V, 5V, 7V, 9V displacement with time	99
Figure 5.44: Varying displacement response with time for recommended settings	102
Figure A.1: Open loop block diagram	114
Figure A.2: Closed loop block diagram	115
Figure C.1: FEA applied forces	128
Figure C.2: FEA applied constraints	129
Figure C.3: FEA Von Mises stress results	131
Figure C.4: FEA displacement results.....	131
Figure C.5: FEA strain results	132

List of Tables

	Page
Table 2.1: Properties of different shape memory alloys [9].....	10
Table 2.2: Comparison of actuation systems [20]	18
Table 2.3: Relative effects of cooling methods [25]	23
Table 2.4: Specific cutting forces [43]	32
Table 2.5: Recommended conditions for single-point carbide tools in aluminium machining [46]	33
Table 3.1: Flexinol physical properties [25]	36
Table 3.2: Flexinol technical characteristics [25]	37
Table 3.3: Flexinol current requirements for a given force	38
Table 5.1: Steady-state errors (mm) in displacement setpoints for different voltages	100
Table 5.2: Steady-state errors (mm) with recommended settings	102

Abstract

A shape memory alloy (SMA) is an intermetallic compound able to recover, in a continuous and reversible way, a predetermined shape during a thermal cycle while generating mechanical work. In this thesis, its use in developing an actuator for a machining process is investigated. The actuator is to drive the tool cross feed into an aluminium workpiece in a finishing lathe operation. The actuator structure was designed with an output shaft to transfer the movement and force of the SMA wire outside the device. The actuator was fabricated and the experimental setup was assembled which also included a power supply control circuit, displacement sensor, temperature sensor and current sensor for feedback, and data collection and monitoring within software. PID control was implemented within the software that regulated the power supplied to the SMA, thereby providing the position control. This study covers the mechatronics system design and development of the actuator, the experiments carried out to determine performance and the results.

Open loop tests were conducted to determine the maximum stroke, the effect of cooling and response to radial forces. These tests revealed the expected non-linearity of the SMA. The actuator achieved the rated maximum stroke of 3-4%. The forced cooling test showed a general improvement of approximately 65% with fans. The radial force tests showed the value of the maximum stroke remained unaffected by force. The results from the closed loop tests responses with a tuned PID controller produced a stable system for various displacement setpoints. The actuator had a feed rate of 0.25 mm/s and an accuracy of 0.0153mm, which was within the acceptable accuracy for turning operations. The system was deemed accurate for a conventional lathe machine cross feed.

Keywords: shape memory alloys; smart actuators; machining end feed actuators.

Chapter 1. Introduction

1.1 Background

An actuator is a device that converts energy to provide a force and motion to perform a required action in a system. A majority of automated mechanical systems use hydraulic, pneumatic and electric actuators. Hydraulic actuators utilise the changes in fluid pressure to produce mechanical action. The main advantages of hydraulic actuators are the high forces that can be achieved, low compressibility of hydraulic fluids and rapid response. The main disadvantage is the containment of the fluid within the system. Hydraulic fluid is prone to leaks and contamination. Hydraulic fluid is also hazardous as it is flammable when pressurised. Other disadvantages include fluid viscosity changes with temperature and cavitation.

Pneumatic actuators are descendants of the hydraulic type but use compressed gas (mostly air) as the transmission medium. The advantages include lower maintenance cost and increased safety due to the non-flammable and cleaner properties of air. The disadvantages include lower force capabilities due to increased friction caused by lack of lubrication.

Electric actuators convert electrical energy to mechanical energy. This is performed by electric motors. They have the advantages of requiring less space and eliminating the need for reservoir tanks, pumps or pressurised lines for transmission medium since they are powered by electricity. The major disadvantage is that the power produced is very small in relation to their size and weight.

Over time, new discoveries have led to developments such as using active materials for actuation. Active materials produce mechanical action in response to non-mechanical inputs or fields such as thermal, electrical or magnetic. These materials include piezoelectric materials, electrostrictive and magnetostrictive materials, electro-rheological and magneto-rheological fluids, and shape memory alloys.

1.2 Shape Memory Alloys

A shape memory alloy (SMA) is an intermetallic compound able to recover, in a continuous and reversible way, a predetermined shape during a thermal cycle. SMAs have been widely used over recent history from static applications such as fasteners, couplings and electrical connectors, to the more recent dynamic applications as actuators. The early dynamic applications were based on ambient temperature-controlled devices such as valves and thermostats. Over time, the inclusion of electrical control systems opened the way to more complex applications in various engineering fields, where the shape could be manipulated for a desired response [1]. SMAs provide prominent advantages over other actuation methods. This has led to its continued and inquisitive research over the years. These benefits mainly include minimal cost, noise and space, and versatility. They are a fraction of the cost compared to motors and solenoids [2]. The cost to build, install and maintain SMAs is lower, as well as the power consumption [2]. While some oscillating power sources produce humming and vibrations that result in disturbances, SMAs are both acoustically and electrically quiet. When installed and operated correctly under the correct conditions, SMAs can operate for millions of cycles with minimal signs of wear, deterioration or changes in performance. SMAs are highly resistant to corrosion, hence their use in extreme conditions ranging from outer space to inside the human body. SMAs save a large amount of space and

weight in comparison to motors and solenoids doing the same task. The form of SMAs allows for flexible designs as they can be straightened, bent or wrapped to suit the product and required movement. These advantages have led to the wide use of SMAs in actuating and/or sensing applications. Even with all these benefits there are some significant drawbacks, such as efficiency concerns, control complexity and slow response (when cooling), which tend to give the conventional hydraulics and electric motors the edge [1].

1.3 Problem Statement

In automated machining, electric motors are typically used as the actuators for driving tool holders. Motors are generally noisy, costly, and voluminous. They also create additional problematic variables such as vibrations. In semi-automated/manual machining, an operator is required to drive the cutting tool into workpiece using a mechanical holder. This has the disadvantage of variable inaccuracies which are both operator and machine dependent. The use of SMA for manufacturing applications is a relatively new area that has rarely been researched.

When subjected to certain thermal cycles, SMAs are able to generate mechanical work by recovering a predetermined shape. This process is continuous and reversible. Thus, an SMA actuator can be developed to drive a tool holder in a machining operation. Considering the advantages and disadvantages of SMAs, their use as an actuator in a machining process can be investigated.

1.4 Objective

The aim of the research was to design and fabricate a shape memory alloy actuator that drives the cross-feed of a machine tool in a turning operation.

1.5 Scope

To achieve the objective, the machining conditions must be identified. This serves a foundation for the actuator requirements. The SMA must be selected to meet these requirements. The actuator structure must be designed and fabricated. A control system with feedback must be developed to control and monitor the operation of the actuator.

The scope of this study can be summarised as follows:

- Designing and fabricating a shape memory alloy actuator prototype.
- Control system hardware and software design.
- Analysis on shape memory alloy behaviour and performance when used as an actuator.

The study was limited to the turning of aluminium for finish cuts. This study covers a mechatronics system design and development with a manufacturing application, as well as materials.

1.6 Methodology

A typical SMA actuator is generally made up of several parts: the mechanical system, the SMA element, a bias element able to restore the deformed shape of SMA element, an electric control unit and a set of fixtures used to couple the actuator with the mechanical system. These components were individually designed and/or selected. The mechanical structure must be designed and constructed, an efficient SMA element selected to provide the required force and motion, and an accurate position control system developed. Based on the design, an SMA actuator system will be constructed and experimentally tested.

Based on the results from the experiments, the feasibility of using an SMA actuator in machining processes will be evaluated.

1.7 Structure

This report firstly covers a review of the relevant literature in Chapter 2. This includes the operation and considerations in SMA actuator design, as well as metal cutting. This is followed by the design and development of the actuator in Chapter 3 where components are designed and selected based on the initial requirements. The actuator is illustrated and each component is described in detail. Chapter 4 covers the experimental setup, the tests carried out and the results recorded. The results are discussed and the performance evaluated in Chapter 5. Finally, the research is concluded in Chapter 6.

Chapter 2. Literature Review

2.1 Shape Memory Alloy Functions

A shape memory alloy has the ability to deform to a predetermined shape and return to its initial shape under temperature changes to perform a useful function. Shape memory alloys can deliver five basic functions or operating modes [3]:

1. *Free recovery* – the SMA delivers displacement with no work. This has applications mainly in control devices and relay mechanisms.
2. *Constrained recovery* – the SMA is restricted from displacement delivering large stresses. Applications include fittings, couplings and connectors for machinery.
3. *Actuator* – the SMA produces work that is a force coupled with displacement. This is mainly used in engineering applications, such as transmission fluid control in vehicles [4] or for vanes controlling the flow of air through jet engines [5].
4. *Superelasticity* – the SMA serves as an enhanced spring with high plastic deformation. This is employed in eyeglass frames where after being subjected to large deformation, returns to its original shape upon release.
5. *High damping* – the SMA possesses high damping properties in the martensite phase. Application examples include its use as inserts in golf clubs allowing increased spin, greater control and a solid feel.

This multi-functionality has led to various fields incorporating SMAs; from the aerospace, transportation and medical industries to everyday domestic applications such as coffee makers and rice cookers [6].

2.2 Thermal Cycle

The SMA thermal cycle involves a crystallographic transition between the low temperature phase, martensite, and the high temperature phase, austenite. SMAs show a thermal hysteresis during transformations between the two phases. This hysteresis means the transformations from martensite to austenite and vice versa never coincide, giving the four distinct temperatures; where M_s and M_f represent the martensite start and finish temperatures while A_s and A_f are the austenite start and finish temperatures, respectively.

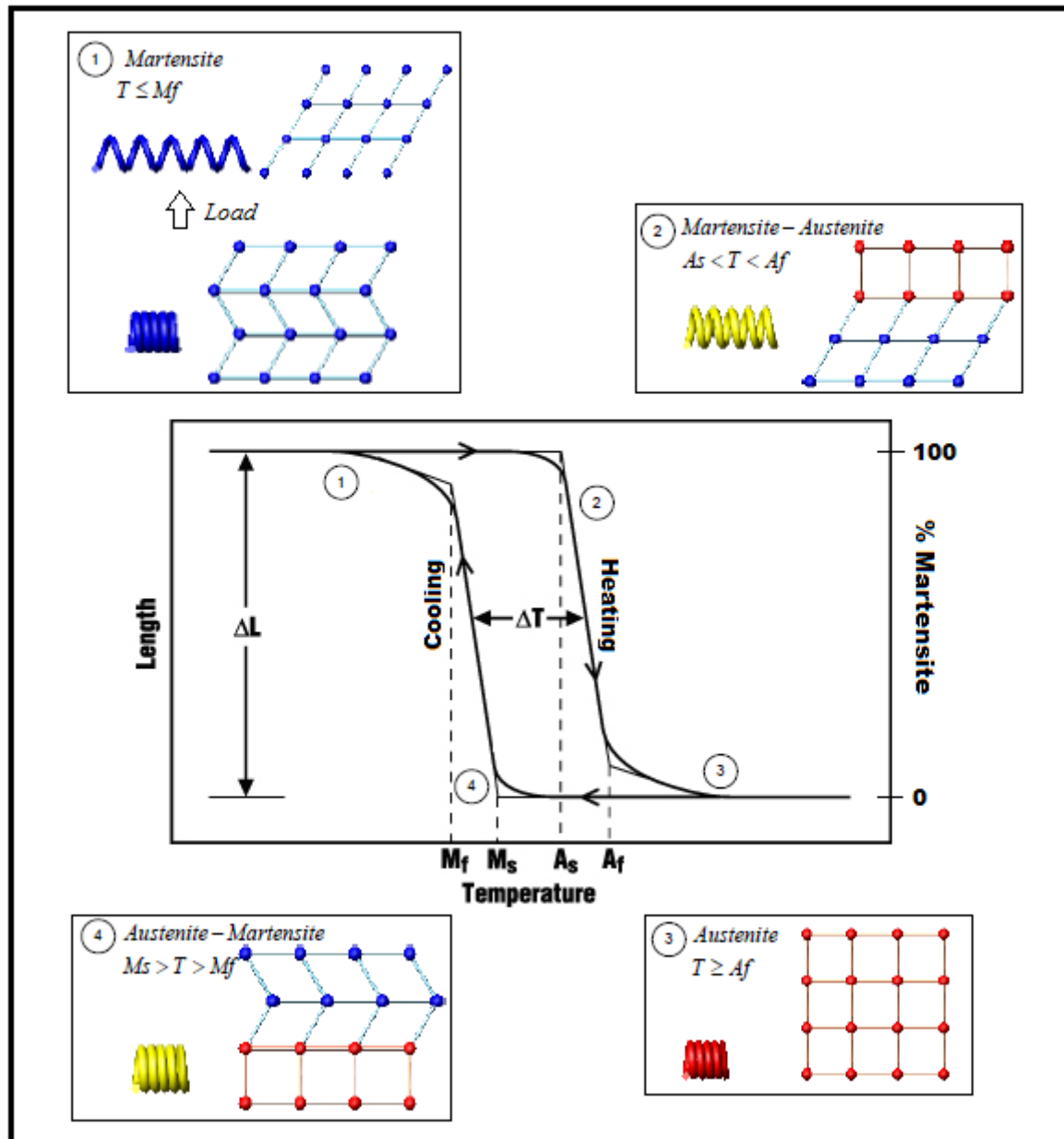


Figure 2.1: SMA thermo-mechanical hysteresis between martensite and austenite [7]

As seen in Figure 2.1, a shape memory element is initially in its martensite phase, which is macroscopically a relaxed state. At this stage, the temperature is equal to or lower than M_f . As it is heated, the austenite phase will begin to form at A_s temperature. The percentage of austenite increases with increase in temperature. This causes the element to physically compress until the full austenite phase is reached at A_f temperature. The temperature of the element is now lowered and the martensite phase begins to form at M_s temperature.

The element gradually reverts to initial relaxed shape as the temperature is decreased to the M_f temperature.

2.3 Material Composition

Copper-based alloys (CuAlNi and CuZnAl) and Nickel-Titanium (NiTi) alloys (also known as nitinol) are the two main groups of SMAs commercially available [5]. Material selection depends on the application of the SMA. The two groups of alloys mainly differ in transformation temperatures and price. Copper-based alloys are cheaper and are commonly found in applications such as fire detectors and clamps. NiTi alloys are more favourable in developing actuators. Even though NiTi has the significant disadvantages of lower transformation temperatures and considerable hysteresis, it has more superior advantages. These advantages include: larger resistivity (10 times higher) so smaller currents are required for electrical resistive heating, higher reproducibility of functional properties, higher mechanical strength thus higher working stress, higher working strain thus a higher work density, and corrosion resistance [8]. A far greater number of commercial applications use NiTi alloy, as it has been researched extensively and its properties and characteristics are well understood [6]. Other elements can be added to NiTi alloys to achieve certain desired characteristics. For example, the addition of copper (Cu) to NiTi reduces hysteresis of the SMA response, but at the expense of decreased transformation strain [6]. Humbeeck [3] and Lagoudas [6] describe other alloy combinations in detail with their advantages and disadvantages. Table 2.1 below compares the properties of nitinol and copper-based shape memory alloys.

Table 2.1: Properties of different shape memory alloys [9]

ITEM	Ni-Ti	Cu-Cu-Zn-Al	Cu-Al-Ni
Melting point (°C)	1250	1020	1050
Density (Kg/m ³)	6450	7900	7150
Electrical Resistivity ($\Omega \cdot m \cdot 10E-6$)	0.5-1.1	0.07-0.12	0.1-0.14
Thermal Conductivity, RT (W/m*K)	10-18	120	75
Thermal Expansion Coeff. (10E-6/K)	6.6-10	17	17
Specific Heat (J/Kg*K)	490	390	440
Transformation Enthalpy (J/Kg)	28,000	7,000	9,000
E-modulus (GPa)	95	70-100	80-100
UTS, mart. MPa)	800-1000	800-900	1000
Elongation at Fracture, mart. (%)	30-50	15	8-10
Fatigue Strength N=10E+6 (MPa)	350	270	350
Grain size (m*10E-6)	20-100	50-150	30-100
Transformation Temp. Range (°C.)	-100 to +110	-200 to +110	-150 to +200
Hysteresis (K)	30	15	20
Max one-way memory (%)	7	4	6
Normal two-way memory (%)	3.2	.8	1
Normal working Stress (MPa)	100-130	40	70
Normal number of thermal cycles	+100 000	+10 000	+5 000
Max. Overheating Temp. (°C)	400	150	300
Damping capacity (SDC %)	20	85	20
Corrosion Resistance	Excellent	Fair	Good
Biological Compatibility	Excellent	Bad	Bad

2.4 Shape Memory Alloy Actuators

SMA's are able to generate mechanical work during the phase transformation. Development of SMA actuators involves precise consideration of two parameters, the force and the displacement, produced during a heating/cooling cycle. The thermal and mechanical hysteresis are one of the factors affecting (and limiting) the precision control of SMA actuators [2]. An SMA actuator only provides force/displacement in one direction when heated. Thus, a bias (return) element must be used to restore the deformed shape after cooling. This characteristic of SMA's is known as the one-way shape memory effect. Most bias mechanisms are implemented with a conventional spring, load force under gravity or another SMA (antagonistic) as shown in Figure 2.2.

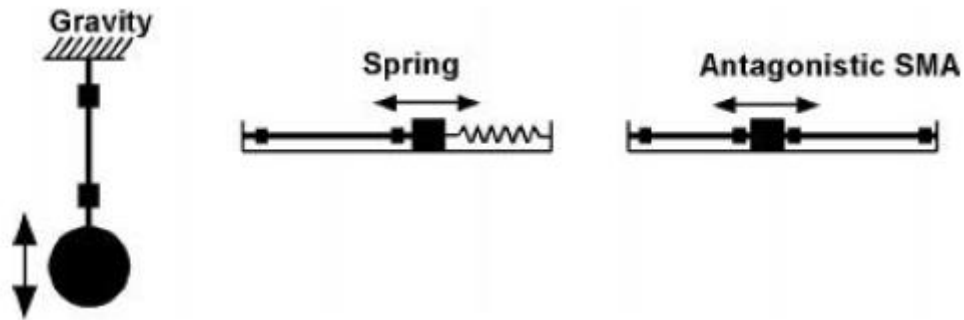


Figure 2.2: Bias force mechanisms [1]

To provide a device with high reproducibility, SMA elements generally require “training” under load over numerous thermal cycles. This involves the element requiring a gradually decreasing bias force over consequent actuator cycles, until the need for the bias is completely eliminated. This is the two-way memory effect, where the SMA element “learns” the behaviour during processing and provides force in both heating and cooling phases during operation. The usability of the two-way memory effect is greatly limited by smaller strains, low cooling phase forces and temperature instability (even slight overheating can remove the two-way effect in an element) [9]. Hence, the one-way memory effect is preferred.

Various researchers and companies have designed and developed unique shape memory alloy actuators, both linear and rotational. Ishii [10] designed a two-way action actuator, shown in Figure 2.3, where an SMA spring and stainless steel spring were working against each other pushing the shaft in either direction.



Figure 2.3: Two-way SMA actuator [10]

Strittmater and Gumpel [11] designed an SMA linear actuator for the activation of a hydraulic valve, shown in Figure 2.4. The SMA wires contract when heated shifting a moveable flange that possessed a shaft, transferring movement outside the closing screw. An outside spring (not shown in the Figure) pulls the shaft and flange back inside the closing screw when current is cut off. The actuator delivered a maximum stroke of 0.8 mm and a force of 98 N.

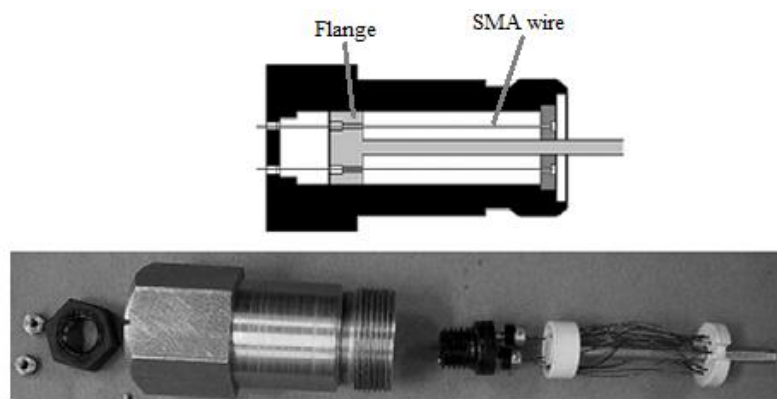


Figure 2.4: Hydraulic valve SMA actuator [11]

Starsys Research and Applied Physics Laboratory (APL) at John Hopkins University [12] designed a mini-actuator which had a travel pin that was moved by an SMA wire coupled with a bias spring, shown in Figure 2.5. The actuator was one of six mechanisms developed as a component of a miniature spacecraft.

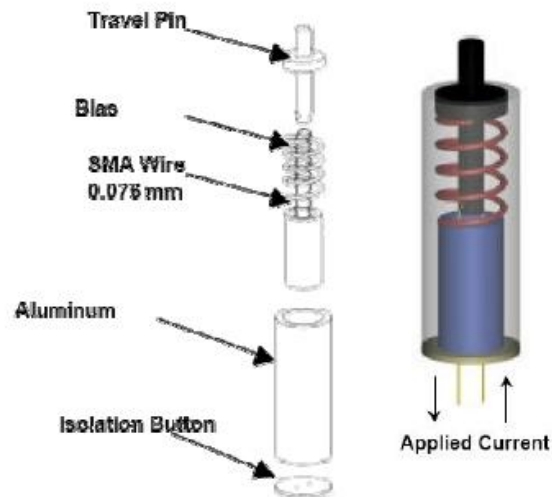


Figure 2.5: Starsys Research and APL mini-actuator [12]

Colli et al. [13] designed an actuator made up of two SMA spring sets that worked antagonistically to produce the movement of an output shaft. Figure 2.6 shows a CAD model and photo of the actuator. The actuator was developed for controlling the air flow into internal combustion engines, resulting in better fuel economy and engine performance.

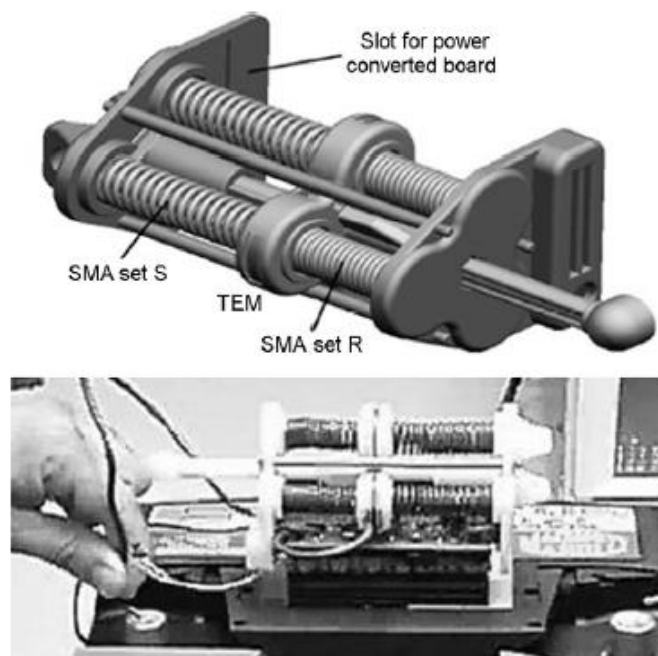


Figure 2.6: Antagonistic SMA linear actuator [13]

Elwaleed et al. [14] designed an SMA beam actuator where SMA wire was fixed on a flexible beam by connecting elements. The actuator consisted of two beams connected to two plates (one fixed, the other moveable) and a shaft fixed on the moveable plate that transferred movement outside the device. Heating the wires caused deflection of the beams, providing displacement of a moveable plate, as shown in Figure 2.7. This configuration provided a stroke of approximately 20 mm. Upon cooling, the beams provided the bias force to restore the wire.

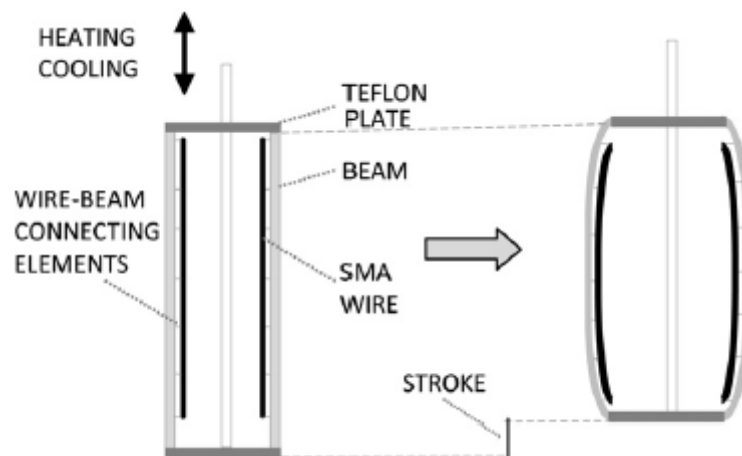


Figure 2.7: SMA beam actuator [14]

Williams et al. [15] developed a shape memory alloy actuator to control the position of an automotive external side mirror. The design, shown in Figure 2.8, comprised of a spring-loaded spherical joint and four SMA wires to rotate the mirror about two axes. The authors met their objective of improving on the conventional DC motor powered mirror actuator by successfully controlling the mirror positioning. In addition, they achieved acceptable disturbance rejection performance.

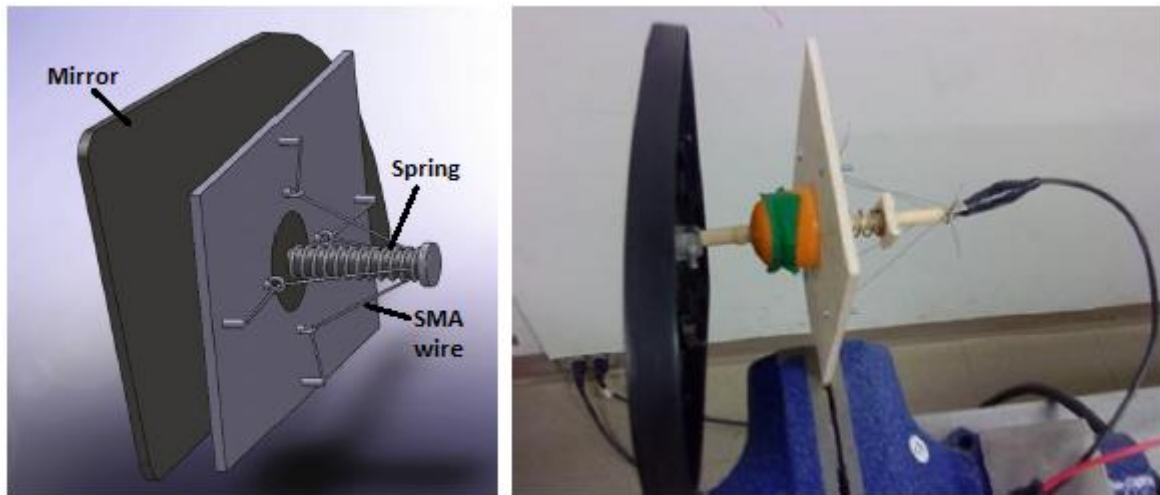


Figure 2.8: SMA mirror actuator prototype [15]

Pöhlau and Meier [16] suggested a high torque drive powered by six pairs of SMA actuators positioned radially inside a flexible gear wheel (called Flexring) with external teeth (Figure 2.9). The flexible wheel was meshed with an external gear wheel with internal teeth. Activating the pairs of SMA wires sequentially produces rotation of the external wheel, as the radial force of the wires is transformed into tangential force at the teeth generating a torque.

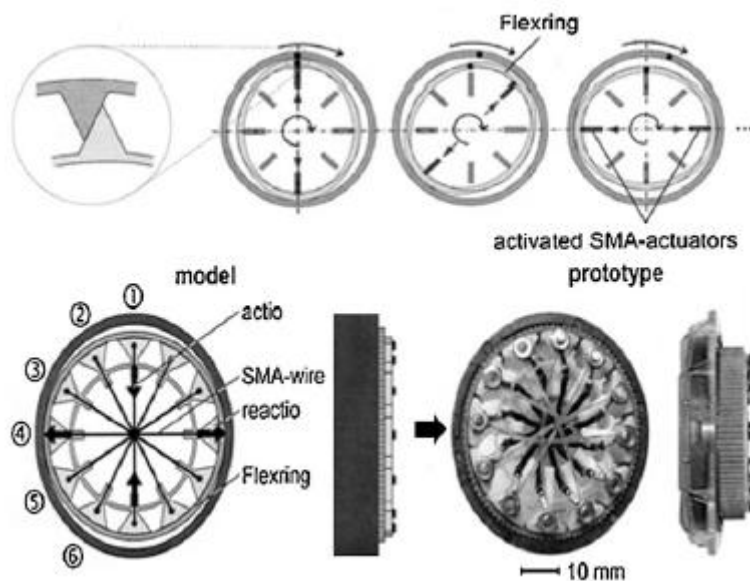


Figure 2.9: SMA drive system [16]

Jansen et al. [17] proposed an angular positioning mini-actuator (Figure 2.10) made up of two drive modules, brake module and snap module, all activated by SMA wires, a gear module connected to an output shaft, a casing module and a sensor/control module. The SMA wires produce a displacement of 30 mm and force of 4 N that is transferred to the gear module through a pulley to produce rotation of the output shaft. The device can produce a maximum angular range of 180° and a torque of 40 N·mm.

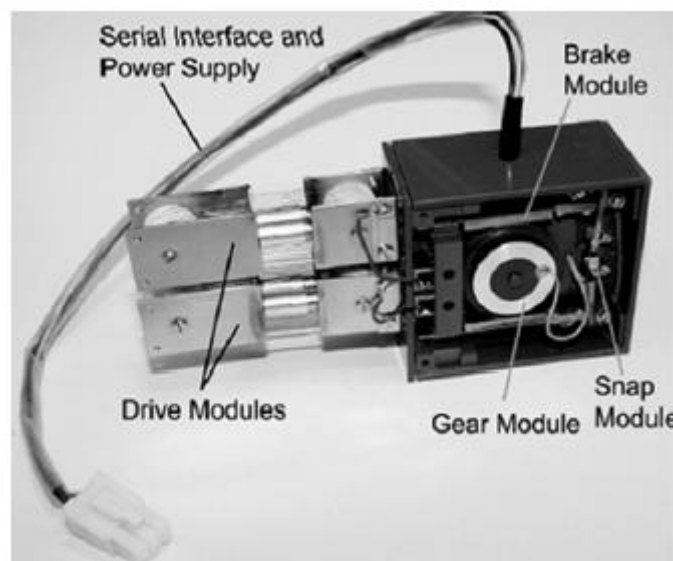


Figure 2.10: Positioning actuator prototype [17]

There are several companies that produce SMA actuators ready for use. Miga Motor Company manufactures a large variety of modular SMA actuators with stroke lengths up to 12.7 mm and forces up to 20 N. The MigaOne, shown in Figure 2.11, is one of the linear actuators they produce. The credit-card-sized actuator has a 9 mm stroke, and comes in three output force options (9 N, 12 N or 20 N) depending on the SMA wire diameter (0.025 mm, 0.03 mm or 0.038 mm, respectively). These actuators could have been used in the design but they would limit flexibility in the design and the cost of acquiring multiple actuators was not feasible in comparison to SMA actuator wires.



Figure 2.11: MigaOne linear SMA actuator [18]

The following companies produce shape memory alloy materials and/or actuators:

- Advanced Materials and Technologies (AMT), Belgium
- Dynalloy, Inc., USA
- Memry Co., USA
- Microfil Industries SA, Switzerland
- Mide Technology Co., USA
- Nitinol Devices & Components, USA
- Shape Memory Applications, Inc., USA
- Special Metals Co., USA/UK
- TiNi Alloy Co., USA
- Toki Corporation, Japan
- Ultimate NiTi Technologies, USA

The only work performed in using SMA for a machining application was by Shin et al. [19]. They developed a novel tool clamp for micro-spindle units. An SMA ring was used for clamping which provided miniaturisation and simplicity. The SMA ring (Figure 2.12) could be

switched between clamped and unclamped states by regulating the temperature and eliminated the need for a collet.

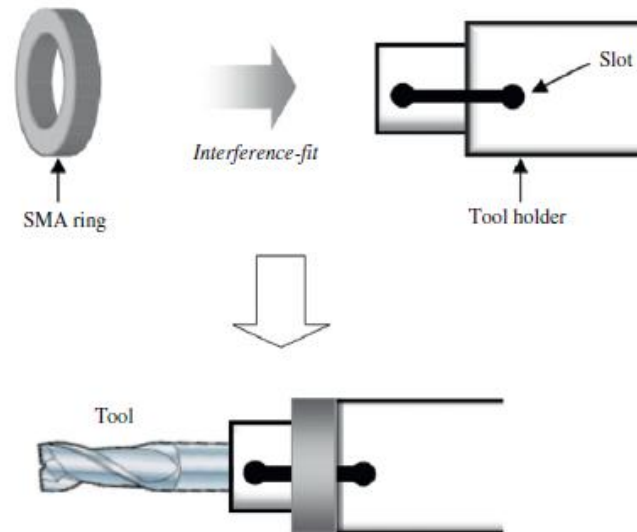


Figure 2.12: SMA tool clamp [19]

Most authors and companies refer to SMA actuators as a better alternative to conventional actuation systems. Hollerbach et al. [20] compared the performance of different active materials and traditional actuation systems. The results are summarised in Table 2.2.

Table 2.2: Comparison of actuation systems [20]

	Stress (MPa)	Strain (%)	Efficiency (%)	Bandwidth (Hz)	Work (J/cm ³)	Power (W/cm ³)
Piezoceramic	35	0.2	50	5000	0.035	175
Single crystal piezoelectric	300	1.7	90	5800	2.55	15000
SMA	200	10	3	3	10	30
Hydraulic	20	80	80	4	5	20
Pneumatic	0.7	90	90	20	0.175	3.5

From Table 2.2, it can be concluded that SMAs have the best stress and strain combination and are therefore most suited in providing work. Thus, SMAs are highly suitable in actuation

that requires significant displacement and force. Various other sources support this conclusion. Nespoli et al. [2] illustrate the high potential for miniaturisation using SMAs, as depicted in Figure 2.13. The high power-to-weight ratio of the SMA compared to other actuation technologies means much less of the material is required to produce the same work output.

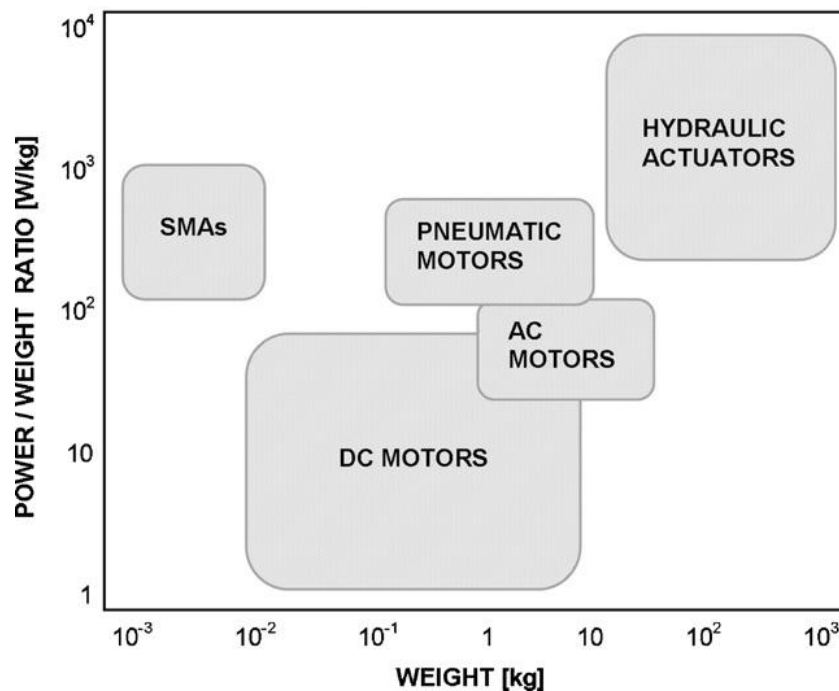


Figure 2.13: Power/weight ratio vs. weight of different actuators. Schematic representation of power density as a function of weight for the most common actuator technologies [2]

Further advantages to the use SMA actuators include, the simplicity of mechanism, cleanliness, silent actuation, seclusion, sensing ability and low driving voltage. However, SMA also have some weak points, such as, a low energy efficiency (<10%), a strong relationship between the strain operation range and fatigue life, fairly slow response speed and a nonlinear behaviour [2].

2.5 Design Considerations for Shape Memory Alloy Actuator Wires

Design involving shape memory material requires clearly defining the interrelated areas; mainly the operating mode, transformation temperatures, heating method, in addition to mechanical considerations (such as tolerances and components assembly), force requirements and cyclic requirements.

A number of calculations must be undertaken for material selection that will meet the desired design requirements. The most conventional forms of shape memory material are wire, ribbon or strip, and spring. Wire is the most common. It provides the maximum amount of force per cross sectional area, matched only by the ribbon form [7]. The wire actuator design methodology documented by Waram [21] assumes linear stress-strain behaviour. The force and diameter are related by the stress as

$$\sigma = \frac{F}{A_{cs}} = \frac{4F}{\pi d^2} \quad (2.1)$$

Where σ is the maximum shear stress, F is the required operating force, and A_{cs} is the cross sectional area (which can be described in terms of diameter d). The maximum shear stress value must be selected conservatively as it affects the number of cycles the actuator can perform [7]. Manufacturers usually provide an approximation of the maximum shear stress according to the desired life of the actuator. The free length of the wire is obtained by

$$L = \frac{S}{\Delta \varepsilon} = \frac{S}{\varepsilon_l - \varepsilon_h} \quad (2.2)$$

Where S represents the stroke, and $\Delta \varepsilon$ is the difference between the high temperature strain ε_h and the low temperature strain ε_l . Similar to the maximum shear stress, the low temperature strain is also a selected value and affects the number of cycles before failure. In nitinol, this can range from 8% for a few cycles to 5% for thousands of cycles [7]. The high temperature strain is given by

$$\varepsilon_h = \frac{\sigma_h}{E_h} \quad (2.3)$$

Where E_h is the value of the Young's modulus for the material at high temperature and σ_h is the high temperature stress. The length increment of the wire at high temperature is given by

$$L_i = \varepsilon_h L \quad (2.4)$$

The low temperature stress is calculated as

$$\sigma_l = \varepsilon_l E_l \quad (2.5)$$

Where E_l is the Young's modulus for the material at low temperature.

The bias force required to revert the wire is calculated as

$$F_r = \sigma_l A_{cs} \quad (2.6)$$

The high resistivity of the shape memory alloy allows heating by feeding a direct current through it (Joule heating). The resistance can be calculated as

$$R = \frac{\rho L}{A} \quad (2.7)$$

Where ρ is the SMA resistivity, L is the free length, and A is the cross sectional area. Ohm's law gives the voltage for activation as

$$V = IR \quad (2.8)$$

Where I is the current. Most manufacturers provide the recommended activation current, but this value can also be determined by testing as it varies under different ambient conditions and alloy composition. The power required is calculated as

$$P = VI = I^2 R \quad (2.9)$$

2.6 Heating and Cooling

SMA actuators require a heating/cooling system as their operation is based on temperature changes. The heating can be achieved through three main methods: electric heating (Joule heating), heating element or ambient heating. Joule heating requires the current to be fed directly through the element. The simplicity of Joule heating makes it the most commonly used method, although, it requires the element to be electrically isolated and a large current supply due to the SMA resistivity. A separate heating element overcomes this disadvantage as small currents can be used with a suitable voltage to provide enough power to heat the material. Though this may seem favourable, it is not very efficient and the mass of the actuator will increase as additional components and space must now be considered. Ambient heating means the SMA element operates according to the surrounding temperature. This method is most effective for applications where the SMA is used as a sensor, without any electric connectors [9].

Cooling of the SMA element can also be done using various methods but the effectiveness is application dependent. Ambient cooling can be used where the environment temperature is below the transformation temperature range and speed requirements are not critical. However, for applications where cooling speed is a critical, an active cooling element must be used to lower the temperature quickly. This can be implemented using heat sinks, forced convection (fan), or a moving liquid (oil or water). It must be noted that systems where cooling elements are continuously present require higher heating currents [9]. Furuya and Shimada [22] used water immersion as a cooling method, which resulted in the SMA wire cooling 10 times faster than an ambient SMA wire. Asada and Mascaro [23] used flowing water around the wire, which could be run only when the wire needed to be cooled. The

main disadvantage of such systems is the need for pumps or compressors with sealing systems, and the increase (up to a factor of 20) in total power consumption [24]. Table 2.3 gives an indication of the relative effects of various cooling methods on cooling time.

Table 2.3: Relative effects of cooling methods [25]

Cooling Method	Improvement in Speed
Increasing Stress	1.2:1
Using Higher Temperature Wire	2:1
Using Solid Heat Sink materials	2:1
Forced Air	4:1
Heat Conductive Grease	10:1
Oil Immersion	25:1
Water with Glycol	100:1

The thermoelectric effect (Seebeck-Peltier) has also been researched as a means of heating/cooling and improving the dynamic performance of SMA actuators. Romano and Tannuri [24] made use of a thermoelectric tablet within a heat sink with the cold face in permanent contact with the SMA wire. This eliminated the need for complex accessories like pumps or compressors but still increased power consumption as the wire required additional heat to overcome the continuous cooling. Peltier elements provide an effective means of achieving active heating and cooling. The heating or cooling occurs depending on the polarity of the voltage fed into the Peltier element. The main advantage of this system is the heating and cooling is provided through the same source and is not applied on the material simultaneously, but the contact surface area with the SMA tends to be insufficient resulting in poor efficiency.

Another method that combines heating and cooling involves controlling the medium in which the SMA material lies, and adjusting it between martensite and austenite temperatures. The main disadvantage of this method is the high operating temperature

range. This in turn involves the complexity of building a precisely controlled heat exchanger [7].

Heat transfer between an object and ambient is given by

$$P = h \cdot A \cdot \Delta T \quad (2.10)$$

Where P is the transmitted power (W), h is the heat transmission coefficient ($\text{W}/\text{m}^2 \cdot \text{K}$), A is the surface area (m^2), and ΔT the temperature difference between the object and ambient (K).

The cooling time can be approximated as

$$t = - \frac{m \cdot c}{h \cdot A \cdot \ln\left(\frac{M_f}{M_s}\right)} \quad (2.11)$$

Where t is the cooling time (s), m is the mass of the active element (kg), and c is the equivalent specific heat ($\text{J}/\text{kg} \cdot \text{K}$). This equation can also be used to determine the heat transmission coefficient h .

As mentioned earlier, hysteresis and nonlinearity of SMAs poses difficulties in applications which require the displacement of actuator generating linear motion. Therefore, in such applications, most SMA actuators are on/off controlled with only two determined positions of movement. This is achieved by maintaining the austenite phase through constant heating and maintaining the martensite phase through constant cooling. To achieve controlled linear motion with variable displacements, a control system based on a precise model must be implemented.

2.7 Modelling and Control

The main challenge in shape memory alloy actuator control is precisely regulating the heating element in order to position the actuator to the desired location. The modelling and

consequent control of SMAs remains challenging primarily due to the nonlinear hysteretic thermo-mechanical behaviour. The hysteresis behaviour can lead to a loss in position precision with up to a 50% error [26].

Various methods of control have been applied to SMA actuators. Sittner et al. [27], Chirani et al. [28], and Bouvet et al. [29], proposed phase transformation kinetic and three-dimensional models for the thermo-mechanical behaviour of SMAs. These complex models, though precise, require finite element code computation which is not suitable for real time control [30]. Majima et al. [31], and Ahn and Kha [32], used a feedforward neural network which obtained its command using a Preisach model for the hysteretic effect. Dutta et al. [33], used a similar feedforward scheme but utilised the Duhem differential hysteresis model. These hysteretic models make the controller synthesis a complicated and time consuming process requiring substantial computational time. Simpler and classical models have also been applied to SMA actuators and improved by various researchers. DaSilva [34] and Calin et. al [35], used variations of linear proportional integral derivative (PID) control approaches. Ahn and Nguyen [36] developed a control algorithm that tuned the parameters of a PID controller thereby producing an adaptive fuzzy PID controller. The use of empirical information for fuzzy control provides a convenient method for constructing nonlinear controllers [36]. PID controllers are often tuned with linear models which are preferred in industry [30]. Gharaybeh and Burdea [37] used pulse width modulation (PWM) to vary the average current flowing into the shape memory element, thus controlling its thermoelectric state.

When using an active cooling system, in addition to the SMA element behaviour model and control, the cooling system itself should also be controlled to improve dynamic performance of the actuator and minimise power consumption.

Control model schemes involve a desired position signal input, a controller, a thermoelectric model to convert power to temperature, a thermomechanical model to convert temperature to position and a feedback signal to determine the deviation from actual and desired positions.

The thermoelectric model involves applying the relation between input power and temperature, given by the formula [5]

$$m \cdot c \cdot \frac{dT(t)}{dt} = P + h \cdot A \cdot (T_0 - T(t)) \quad (2.12)$$

Where m is the mass of the active element (kg), c is the equivalent specific heat (J/kg·K), T is the temperature of the active element, P is the input power (W), h is the heat transmission coefficient (W/m²·K), A is the surface area (m²), and T_0 is the environment temperature.

The thermomechanical model involves using a mathematical expression that describes the shape memory transformation behaviour. Liang and Rogers [38] made use of a cosine function to describe the graphical representation of the transformation behaviour as a mathematical expression. This model was accomplished in two steps. Firstly, equations are derived relating the martensite fraction ξ in the SMA element to temperature and stress. For transformation from martensite to austenite with an initial martensite fraction ξ_0 the formula is

$$\xi = \frac{\xi_0}{2} [\cos(\alpha_A(T - A_s) + b_A\sigma) + 1], \quad M \rightarrow A \quad (2.13)$$

Where

$$\alpha_A = \frac{\pi}{A_f - A_s}, \quad A_s \leq T \leq A_f \quad (2.14)$$

$$b_A = \frac{-\alpha_A}{\tan \beta} \quad (2.15)$$

For the reverse transformation

$$\xi = \frac{1-\xi_0}{2} \cos[\alpha_M(T - M_f) + b_M \sigma] + \frac{1+\xi_0}{2}, \quad A \rightarrow M \quad (2.16)$$

Where

$$\alpha_M = \frac{\pi}{M_s - M_f}, \quad M_f \leq T \leq M_s \quad (2.17)$$

$$b_M = \frac{\alpha_M}{\tan \gamma} \quad (2.18)$$

For a fully martensitic and fully austenitic condition, $\xi = 1$ and $\xi = 0$, respectively. When the element is stressed ($\sigma \neq 0$) higher temperatures will be required to bring about phase change. The increase is linear, with critical temperatures increasing with the applied stress [5]. These changes are described by slopes β (the angle between the A_s at no stress and the A_s' under stress) and γ (the angle between the M_f at no stress and the M_f' under stress), used to determine the values of b_A and b_M . The angles are measured from the horizontal at the zero stress temperature on a stress versus temperature graph as shown in Figure 2.14.

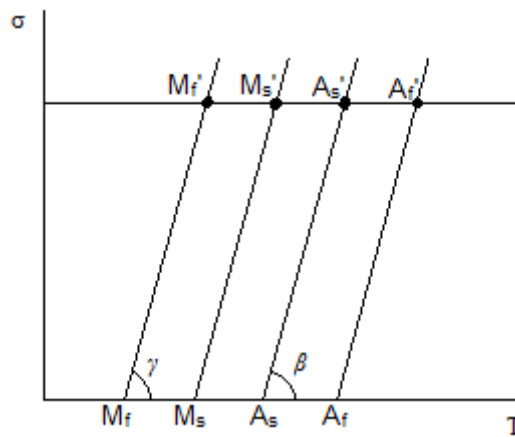


Figure 2.14: Change of critical phase temperatures with stress [5]

Secondly, the martensite phase fraction determined is applied to the constitutive model.

Liang [39] expressed the constitutive model of the shape memory effect with the equation

$$\sigma - \sigma_0 = D(\varepsilon - \varepsilon_0) + \theta(T - T_0) + \Omega(\xi - \xi_0) \quad (2.19)$$

The equation combines stress σ , strain ε , temperature T and phase fraction ξ , where σ_0 , ε_0 , T_0 , ξ_0 are initial states, and D is the Young's modulus, θ is the thermoelastic coefficient, Ω is the transformation coefficient.

As the material is loaded in the fully martensitic phase, the material response remains elastic until a point where plastic deformation occurs. When the material is unloaded, the stress reaches zero, but the strain remains at the maximum limit it attained. The maximum recoverable martensitic strain, or the recovery strain limit ε_L , is the maximum strain attained after plastic deformation, calculated as

$$\varepsilon_L = -\frac{\Omega}{D} \quad (2.20)$$

The recovery strain limit is generally constant between the martensitic phase and austenitic phase, and is therefore considered temperature-independent constant that is specified by the SMA manufacturer. Equation 2.20 can then be used to determine the transformation coefficient.

The Young's modulus varies significantly between the two material phases and can be calculated as

$$D = D_A + \xi(D_M - D_A) \quad (2.21)$$

Where D_A is the Young's modulus in the austenite phase and D_M is the Young's modulus in the martensite phase. Similarly, a relationship for the thermoelastic coefficient can be written.

These models can be implemented in software to simulate the behaviour of an SMA element in response to a given input and optimise controller parameters. The control model block diagram is as shown in Figure 2.15.

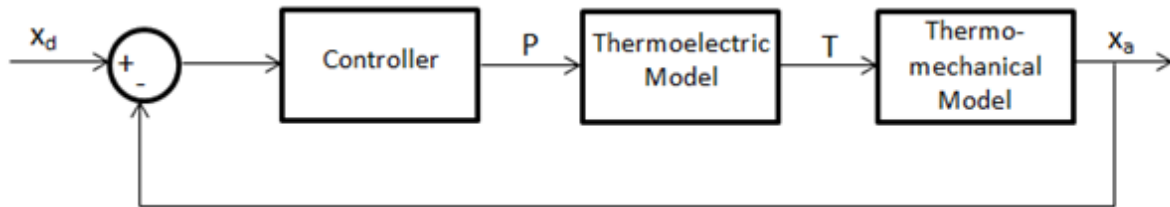


Figure 2.15: Control system model

Though significant work has been done in developing models that imitate the behaviour of SMAs, they are still not highly accurate and will generally produce results that vary from the actual performance. Shape memory manufacturing and production is such that no two batches will ever be exactly the same. SMA Inc., California and a few other companies are utilising quality control standards, like ISO-9002, to maintain some uniformity in production [7]. Despite this, each material still behaves slightly differently. The recommended method is through testing of the actual material in use. Shape memory manufacturers provide datasheets which are a useful guide in testing the material rather than designing using theoretical formulas.

2.8 Metal Cutting

Since the shape memory alloy actuator is designed to drive the tool holder for a machining (turning) operation, it is important to understand the process of metal cutting and the forces involved. The tool is usually wedge-shaped and the removed material is sheared in the form of a chip. When cutting occurs, three main forces act on the tool [40]:

1. *Tangential force* – acts in a direction tangent to the revolving workpiece. This is the workpiece resistance to rotation. It accounts for 99% of the total power required by the operation.
2. *Longitudinal force* – acts parallel to the workpiece longitudinal axis. This force opposes the tool's longitudinal feed. It is 50% of tangential force and accounts for 1% of the total power required by the operation, as feed velocity is low compared to the workpiece rotational velocity.
3. *Radial force* – acts in a radial line from the centre of the workpiece. It is the smallest of the forces, being 25% of the tangential force.

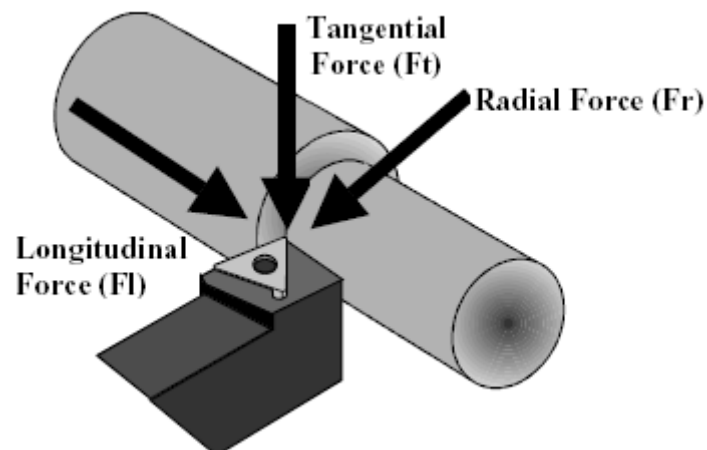


Figure 2.16: Cutting force components

Figure 2.16 shows the three force components, their resultant is the total force acting on the cutting tool. The actuator designed in this study must be sufficiently stiff to overcome the radial force component and drive the tool into the workpiece. If this force is not overcome, the tool will be pushed away from the workpiece surface, leading to dimensional inaccuracies and possible failure of the actuator structure.

Cutting speed, tool feed and depth of cut are the major factors affecting the turning operation [41]. The cutting speed is the rotational/surface speed of the workpiece, the feed is the distance the cutting tool moves along the longitudinal path per revolution, and the depth of cut is how deep the workpiece is engaged by the tool face. These cutting conditions are the root parameters in calculating turning performance parameters such as material removal rate and power. The material removal rate is calculated as

$$Q = f \times v_c \times a \quad (2.22)$$

Where f is the feed per revolution, v_c is the cutting speed and a is the depth of cut. The influence of the material being machined is reflected in the specific cutting force k_c , introduced by O. Kienzle in 1957, calculated from an empirical formula [42]. The specific cutting force is primarily a function of the material being machined, the feed, cutting geometry and tool wear (increase of 30-40% if worn) [43]. The cutting force is calculated as

$$F_c = k_c \times a_p \times f \quad (2.23)$$

From the cutting force, the power (in kW) can be calculated as

$$P = \frac{F_c \times v_c}{60000} \quad (2.24)$$

Table 2.4 shows the specific cutting forces of various materials.

Table 2.4: Specific cutting forces [43]

Class of material		k_c^* new tool	k_c^* worn tool
Aluminium alloys:	- forged - annealed - cast Si < 13	500	700
Aluminium alloys:	- forged - aged - cast Si > 13	750	1,050
- FGL250 type GL cast-irons		1,250	1,750
- FGS500 type GS cast-irons		1,500	2,100
R < 600 steels			
R < 800 steels		1,750	2,450
Titanium Alloys			
R < 1000 steels			
Austenitic stainless steels		2,000	2,800
R < 1200 steels			
X200Cr12 annealed tool steels		2,250	3,150
R < 1400 steels			
Refractory stainless steels		2,500	3,500
Mn X120Mn12 steels		2,750	3,850
Nickel-based alloys		3,000	4,200
Cobalt-based alloys			
60HRC steels		3,250	4,550

Marandet, et al. [43] state the specific cutting force of aluminium alloys with Si < 13% and Si > 13% as 500-700 N/mm² for a new tool and 700-1050 N/mm² for a worn tool, respectively.

Sandvik's catalogue [44] also states that the specific cutting force of aluminium alloys is in the range of 700-1000 N/mm² for aluminium alloyed with Si < 10% to Si > 10% respectively.

Kalpakjian and Schmid [45] provide the following ranges for turning operations on aluminium alloys:

- Cutting speeds 200-1000 m/min
- Depths of cut 0.5-12 mm
- Feeds 0.15-1 mm/rev

The higher range of the cutting speeds is for coated carbide and cermet tools. High-speed steel tools are operated at cutting speeds lower than that indicated above.

Krar et al. [46] provided cutting speeds and feeds for rough and finish turning of aluminium using high-speed steel toolbits:

- Cutting speed 61 m/min (rough cuts), 93 m/min (finish cuts)
- Feeds 0.4-0.75 mm/rev (rough cuts), 0.13-0.25 mm/rev (finish cuts)

For single point carbide tools, the authors recommend the feed and cutting speed ranges shown in Table 2.5 below for a corresponding depth of cut range.

Table 2.5: Recommended conditions for single-point carbide tools in aluminium machining [46]

Depth of Cut (mm)	Feed (mm/rev)	Cutting Speed (m/min)
0.15-0.4	0.05-0.15	215-305
0.5-2.3	0.15-0.4	135-215
2.55-5.1	0.4-0.75	90-135
7.6-17.8	0.75-2.3	30-60

Machining accuracy refers to the ability to position the tool point within the working envelope. The acceptable positioning accuracy for turning operations is generally within 0.013mm, for most lathe machines [47].

Chapter 3. Design and Development

3.1 Design Requirements

The actuator design requirements were based on a machining scenario. This was narrowed down to the turning process of aluminium with a single point tool. The design was chosen to cater for finish cuts. The shape memory alloy element selection was limited to commercially available alloys, thus certain shape and mechanical design properties were dependent on what the manufacturer supplied. Customised alloys with desired shape and mechanical parameters can be manufactured but this is a time consuming and expensive exercise, and as a result not cost effective.

The actuator must be designed and constructed with the following considerations:

- Cutting force of resulting from finishing in aluminium turning must be overcome.
- Linear displacement.
- Stroke must achieve the required depth of cut for finish cuts in the range of 1-2mm.
- SMA actuator wire must be commercially available.
- Uniform current must be supplied to wires.
- Wire configuration must maximize the heat transfer surface area.
- Wires must be attached such that they can be easily replaced, and also allowance for additional wires to be used, making the actuator versatile should force requirements increase.
- Components must be easy to assemble and disassemble for easy accessibility and maintenance.

- Control system must be developed to precisely regulate the wire temperature and consequent displacement.

3.2 Forces in Aluminium Turning

The actuator structure must be capable of withstanding the overall cutting force. The cutting force has three components, but the actuator wire need only overcome the radial force to drive the tool into the workpiece. The typical total cutting force in turning an aluminium workpiece was calculated and the radial force was approximated as 25% of the result. For this to be calculated, cutting conditions must be selected. Although, most of the conditions are machine and tool dependent, some preliminary values were selected as a starting point for force calculation. From the researched data values collected, the following finish cutting conditions were selected:

- Depth of cut 1mm
- Feed 0.25mm/rev
- Specific cutting force of aluminium alloys 1050N/mm²

The cutting force was found to be

$$F_c = k_c \times a_p \times f = 1050 \times 1 \times 0.25 = 265.5N$$

From the calculations, the cutting force was approximated to 300N.

The tangential force is stated as being 99% of the cutting force, the longitudinal force 50% and the radial force 25%.

$$F_t = 300 \times \frac{99}{100} = 297N$$

$$F_l = 300 \times \frac{50}{100} = 150N$$

$$F_r = 300 \times \frac{25}{100} = 75N$$

3.3 Wire Selection

The common SMA forms available are wire, ribbon and spring, with wire and ribbon providing the greatest force per cross sectional area. Due to this force capability as well as availability, the final design makes use of the wire form. Flexinol shape memory alloy actuator wires, manufactured by Dynalloy, were selected. Flexinol wires are composed of nickel-titanium. Table 3.1 shows the physical properties of Flexinol wires.

Table 3.1: Flexinol physical properties [25]

1. Density	0.235 lb/in ³ (6.45 g/cm ³)
2. Specific Heat	0.20 BTU/lb * °F (0.2 cal/g * °C)
3. Melting Point	2370 °F (1300 °C)
4. Latent Heat of Transformation	10.4 BTU/lb (5.78 cal/g)
5. Thermal Conductivity	10.4 BTU/hr * ft * °F (0.18 W/cm * °C)
6. Thermal Expansion Coefficient Martensite Austenite	3.67x10 ⁻⁶ /°F (6.6x10 ⁻⁶ /°C) 6.11x10 ⁻⁶ /°F (11.0x 10 ⁻⁶ /°C)
7. Electrical Resistivity (approx.) Martensite: Austenite:	32 micro-ohms * in (80 micro-ohms * cm) 39 micro-ohms * in (100 micro-ohms * cm)

Though Flexinol is chemically similar to Nitinol, it is significantly more stable and can operate over thousands more cycles with no noticeable change in performance. Flexinol has been tested over its entire length to consistently perform to specifications.

Dynalloy provides a range of Flexinol wire sizes with diameters from 0.025mm to 0.508mm.

The Flexinol wires are available in two categories, HT (high temperature) and LT (low

temperature). The main difference being that HT wires have an austenite finish temperature of 90°C, while LT wires have an austenite finish temperature of 70°C.

Achieving the desired shape memory behaviour requires the appropriate diameter wire to be carefully selected. Table 3.2 shows the characteristics of the various Flexinol wire sizes.

Table 3.2: Flexinol technical characteristics [25]

Diameter Size (mm)	Resistance (ohms/m)	Pull Force* (grams)	Approximate** Current at Room Temperature (mA)	Contraction** Time (seconds)	Off Time 70° C "LT" Wire*** (seconds)	Off Time 90° C "HT" Wire*** (seconds)
0.025	1424.8	8.9	45	1	0.18	0.15
0.038	889.5	20.0	55	1	0.24	0.20
0.050	500.0	35.6	85	1	0.4	0.3
0.076	232.2	80.2	150	1	0.8	0.7
0.102	126.0	142.5	200	1	1.1	0.9
0.127	74.8	222.7	320	1	1.6	1.4
0.152	55.1	320.6	410	1	2.0	1.7
0.203	29.1	570.0	660	1	3.2	2.7
0.254	18.5	890.6	1050	1	5.4	4.5
0.305	12.2	1282.5	1500	1	8.1	6.8
0.381	8.3	2003.9	2250	1	10.5	8.8
0.508	4.3	3562.6	4000	1	16.8	14.0

The most efficient wire was selected based on the current requirements. Table 3.3 shows the various wire sizes with the activation current and pull force extracted from the Flexinol datasheet. The pull force (3562.6 grams) for the largest wire size available was selected to calculate the total current for the number of wires required in parallel to achieve that force.

Table 3.3: Flexinol current requirements for a given force

Wire Diameter (mm)	Force (grams)	No. of Wires	Current (mA)	Total Current (mA)
0.025	8.9	400.3	45	18013.1
0.038	20.0	178.1	55	9797.2
0.050	35.6	100.1	85	8506.2
0.076	80.2	44.4	150	6663.2
0.102	142.5	25.0	200	5000.1
0.127	222.7	16.0	320	5119.1
0.152	320.6	11.1	410	4556.0
0.203	570.0	6.3	660	4125.1
0.254	890.6	4.0	1050	4200.2
0.305	1282.5	2.8	1500	4166.8
0.381	2003.9	1.8	2250	4000.1
0.508	3562.6	1.0	4000	4000.0

As seen on Table 3.3, the 0.025mm diameter wire requires the most current and the 0.508 mm wire requires the least current. Thus, approximately two 0.38 mm wires can produce the same force as four hundred 0.025mm wires for approximately 78% less current. These results hold for any required force. Smaller diameter wires have a higher surface to volume ratio giving them better heat transfer characteristics. Though smaller diameter wires provide higher performance, the large number of wires required in parallel increase the complexity of the actuator and the power requirements are too excessive. The 0.381mm diameter wire was therefore selected to maintain a high efficiency and minimize the wire bundle size.

3.4 Wire Bundle

A preliminary requirement was to achieve a thrust force to overcome the radial cutting force. A single Flexinol wire cannot produce the required force, thus a wire bundle must be

used to improve the force capabilities. By assembling the wires mechanically in parallel a greater force can be achieved. The total force of the actuator is expressed as

$$F_{total} = F_{bias} + F_{net} \quad (3.1)$$

Where F_{bias} is the bias force used to restore the actuator to its martensite state and F_{net} the force exerted by the actuator. Though the bias force can be calculated using Equation 2.6, the wire manufacturers recommend an approximate bias force of two-fifths the total load.

$$F_{bias} = \frac{2}{5} F_{total} \quad (3.2)$$

The target force to be achieved (F_{net}), as was previously calculated, 75N. After substituting Equation 3.2 into Equation 3.1 this yields

$$F_{total} = \frac{2}{5} F_{total} + 75$$

Solving for the total force gives

$$F_{total} = 125N$$

The selected 0.38mm wire can provide a pulling force of 2003.9g (20N). To achieve this force, the number of wires required is calculated as

$$N = \frac{F_{total}}{F_{wire}} = \frac{125}{20} \cong 6 \text{ wires}$$

When wires are bundled, they must be separated to maximize the heat transfer surface area so the cooling medium can freely flow around the surfaces [48]. The wires were arranged in a spread lattice held in tension with crimps.

A bundle of 6 Flexinol 0.381mm actuator wires were fixed in a circular pattern onto the blocks. The wires were insulated with a plastic sleeve and crimped on each end to hold them

in tension. The Flexinol wires each have a pull force of 2000 grams giving a total pull force of 12000 grams (120N). This was lower than the 125N calculated but was acceptable as the cutting force calculated in Section 3.2 was approximated to 300N from 265.5N and could cater for this.

3.5 Stroke

The stroke determines the movement of the actuator shaft, which in turn is the depth of cut. The manufacturer approximates a 3% to 4% stroke with a normal bias spring setup [25]. The appropriate wire length must be selected to achieve the desired stroke. The stroke was selected based on the selected depth of cut of 1mm. Thus, the wire length should have a minimum length of 33.3mm.

3.6 Cycle Rate

The cycle rate is the amount of time needed for the shape memory element to contract and relax. The contraction is solely due to heating and the relaxation is solely due to cooling. The cycle rate is thus entirely dependent on the rate of heating and cooling of the Flexinol wire. Direct electric heating was the chosen method as it is the most advantageous and convenient method to implement. The entire bundle can be evenly heated by feeding a direct current through the SMA wire bundle. Flexinol has a high resistance but is still conductive enough to carry current easily [25]. For the 0.381mm Flexinol, 2.25A of current is required for the wire to contract within 1 second. Alternating current, direct current or pulse width modulated current may be used. The Flexinol low temperature wire must be heated to 70°C while the Flexinol high temperature wire must be heated to 90°C to achieve maximum displacement, both requiring the same value of current.

The selected Flexinol wire (0.381mm) is rated to take 10.5 seconds and 8.8 seconds for the low temperature wire and high temperature wire to relax, respectively. The high temperature wire was selected due to the shorter cooling time. The higher temperature differential between the ambient temperature and the HT wire means the wire will experience a faster rate of heat loss and drop to the transformation temperature faster. The cooling times specified by the manufacturer are under ambient conditions. This can be further reduced by implementing cooling elements.

3.7 Bias Force

The bias force restores the original shape of the SMA wire when in the martensite state. This can be done using a load force, spring or another SMA wire set up in a differential manner. A conventional spring is commonly utilised for this purpose. A spring would cause an extremely rapid (snap) return of the actuator during cooling. Thus, a gas spring is implemented which would provide both the bias force and smooth retraction.

The required bias force was calculated from Equation 3.2 as

$$F_{bias} = \frac{2}{5} F_{total} = \frac{2}{5} \times 120 = 48N$$

Stabilus Lift-O-Mat spring was used to provide the bias force. The gas spring (Figure 3.5) consists of a pressure tube filled with nitrogen which creates a force as it is compressed by the piston. In addition, the Lift-O-Mat spring provides hydraulic compression and extension damping which creates a smooth linear movement. An oil chamber produces the damping, where the damping range is determined by the oil amount and the damping degree is determined by the oil viscosity.

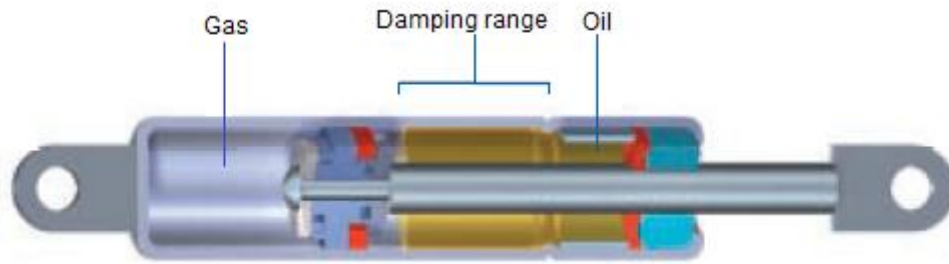


Figure 3.1: Stabilus Lift-O-Mat gas spring [49]

Stabilus Lift-O-Mat springs have the following advantages [49]:

- Simple structure
- Excellent performance/price ratio
- Standard product line
- Damping in compression and extension
- Fast and easy mounting
- Maintenance-free

The spring selected had the following characteristics:

- Force 50N
- Extended length 200mm
- Stroke 60mm

The wire bundle force of 120N and the bias force of 50N meant the actuator produced a net force of 70N. The design was such that the SMA wire length would be approximately the same length as the bias spring. Thus the wire length was 200mm and the stroke was 6mm. The 200mm wire length would produce a noticeable stroke and provide some clearance.

3.8 Power Supply

As Joule heating was selected to actuate the wires, a sufficient power source must be selected to supply the required current. The power required is calculated from the resistance and current.

Though the actuator wires are mechanically arranged in parallel, this is not the best way to implement the circuit design as it causes impractical power requirements. If the wires are connected electrically in parallel the effective linear resistance R_{EFF} is given by [48]

$$\frac{1}{R_{EFF}} = \sum_{n=1}^N \frac{1}{R_n} \quad (3.3)$$

Where R_n is the linear resistance of a single wire and N is the number of wires in the bundle.

As all the wires have the same linear resistance, the effective resistance becomes

$$R_{EFF} = \frac{R_n}{N} \quad (3.4)$$

The linear resistance of the 0.381mm wire is 8.3Ω/m. For the length of 200mm, the resistance is 1.66Ω. The bundle consisting of six wires will have an effective resistance of 0.28Ω. The current required for a single wire to contract within one second is rated as 2.25A. Thus, the current required for the electrically parallel bundle would be six times this rated current, 13.5A. This would produce a voltage drop of 3.78V across the bundle.

This resulting combination of high current and low voltage can be minimised by creating a circuit where the wires are electrically connected in a combination of series and parallel paths while maintaining mechanically parallel arrangement. For a combination of series and parallel paths, the voltage drop V_B and current I_B required across the bundle are calculated as [48]

$$V_B = I_{SMA} \cdot \frac{N}{p} \cdot L \cdot R \quad (3.5)$$

$$I_B = p \cdot I_{SMA} \quad (3.6)$$

Where I_{SMA} is the single wire activation current, N is the number of wires in the bundle, p is the number of parallel paths, L is the bundle length, and R is the single wire linear resistance.

Based on this method and applying Equation 3.5 and Equation 3.6, two electrically parallel paths were chosen for the bundle giving a voltage drop of 11.2V and a current of 4.5A across the bundle.

$$V_B = 2.25 \cdot \frac{6}{2} \cdot 0.2 \cdot 8.3 = 11.2V$$

$$I_B = 2 \cdot 2.25 = 4.5A$$

The power required is calculated from Equation 2.9 as

$$P = V_B I_B = 11.2 \times 4.5 = 50W$$

The power supply used was the Mean Well S-250-12, rated at 12V DC, 18A. The peak power output of 216W was much greater power than required to actuate the bundle.

3.9 Control Method

The wire must be quickly heated to contract to a defined length and held in that position for a period of time. This requires control of the driving current. Closed loop position control was implemented where PID control was applied to a PWM signal duty cycle. PID controllers are preferred in industry as they are robust and simple to implement and tune [30]. This method was a combination of that used by DaSilva [34] (PID) and Gharaybeh and Burdea [37] (PWM). A PID controller with tuning features and PWM signals are simple to implement

compared to the other methods mentioned in Section 2.7 which require finite element code computation which is not suitable for real time control [30].

The PWM signal was the input of a MOSFET switching circuit which controlled the power supply to the SMA wires, controlling the heating and the subsequent wire contraction and displacement of the shaft. Based on the feedback, the PWM duty cycle is varied accordingly to achieve and maintain the desired position. Feedback was provided through displacement, current and temperature sensors. The relation between input power and output position was used to estimate the power needed to keep the actuator in the desired position.

The block diagram of the actuator control system is shown in Figure 3.2.

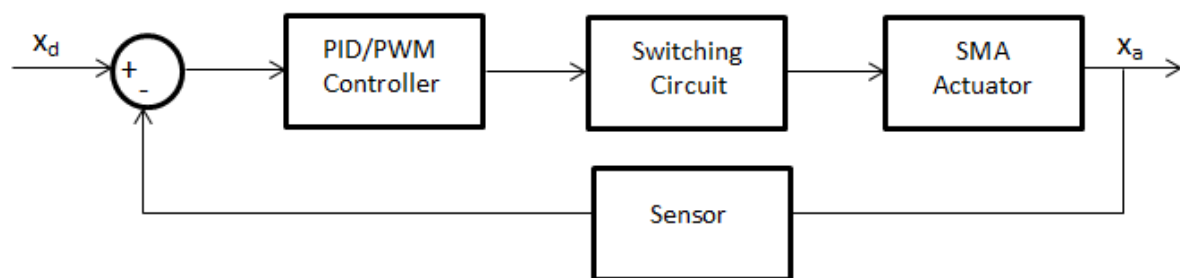


Figure 3.2: Actuator control system

3.10 Switching Circuit

The switching circuit was responsible for varying the power being supplied to the wires. A MOSFET (IRFZ44N) was used as the switching device, which was controlled by a logic-level signal. The circuit schematic is shown in Figure 3.3.

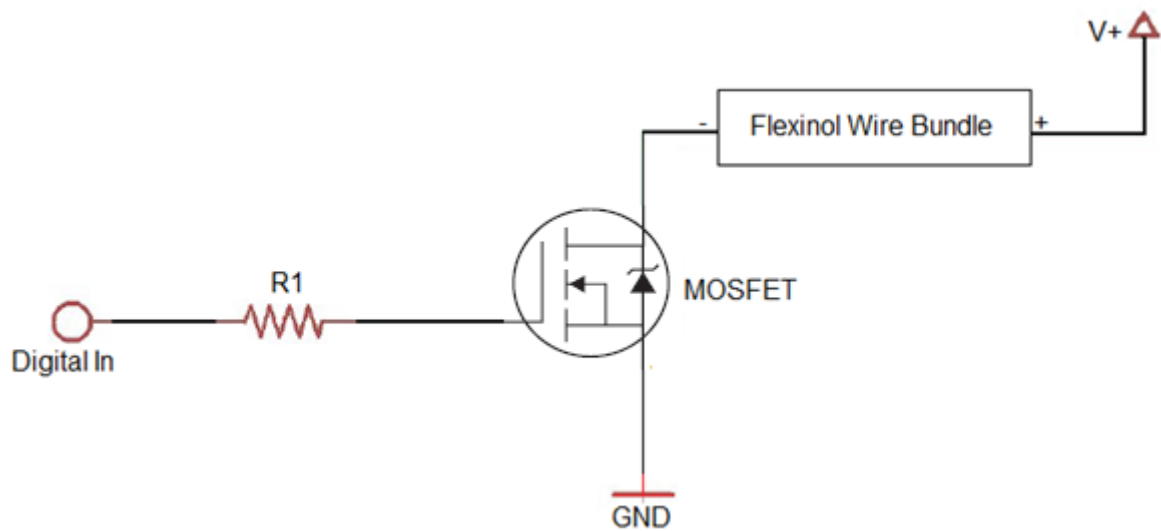


Figure 3.3: MOSFET switching circuit

A high digital signal allows the current to flow through the SMA element and the MOSFET to ground. A low digital signal effectively cuts the current supply. This setup allows switching of the high current supply using a low current, logic-level signal. The logic-level input was supplied in the form of a PWM signal to control actuation.

3.11 Sensors

Three parameters needed to be monitored: current, temperature and displacement. A current sensor monitors the current being supplied to the SMA wire bundle. A Honeywell Micro Switch CS series linear current sensor was selected. The sensor incorporates a linear output Hall effect transducer that outputs a percentage of its supply voltage in proportion to the sensed current. When operating at zero current, the output voltage of the current sensor is half of its supply voltage. Depending on the direction of current flow, the output

voltage will either decrease or increase from this offset voltage to a limit of 25% or 75% of the supply voltage, respectively. The current sensor selected was the CSLA1CD, capable of sensing up to 57A, either AC or DC current, with a supply voltage of 8V to 16V and a sensitivity of $49.6\text{mV}\cdot\text{N}/\text{A}$ (where N is the number of times the sensed wire is looped through the sensor toroid). The sensor was supplied with 12V. This gave a span of 3V on either side of the 6V offset. The sensed wire was looped eight times giving a sensitivity of approximately $0.4\text{V}/\text{A}$. The eight loops meant the sensor's maximum output voltage of 9V would represent a maximum sensed current of 7.5A.

A thermocouple in contact with the wires was used to monitor temperature. An RS J-type welded tip PTFE insulated thermocouple was selected. The thermocouple had a sensing tip of 0.2mm and a temperature range of -50°C to 260°C . The tip was sufficiently small to be attached to the 0.38mm Flexinol wire for monitoring temperature.

Displacement was measured using a linear potentiometer. The Opkon LPT linear motion transducer was selected. The transducer had a measuring stroke of 50mm. The transducer used a voltage divider principle to output a proportion of its supply voltage in relation to stroke. The stroke of the potentiometer rod varied its resistance. The resolution was essentially infinite as it depended on the voltage supplied. The supply voltage of 12V divided by the potentiometer's stroke of 50mm gave a resolution of $0.24\text{V}/\text{mm}$.

3.12 Data Acquisition

The signals from the sensors must be fed into a software package for data processing and analysis. The data acquisition (DAQ) module was the bridge that linked the sensors to software. The National Instruments Compact DAQ (NI cDAQ) was selected. The NI cDAQ

(Figure 3.8) consisted of a chassis with slots for hot-swappable I/O modules with integrated signal conditioning. Four modules were selected:

- NI 9211 thermocouple input module – 4 channel, 14 S/s, 24-bit resolution, $\pm 80\text{mV}$, antialiasing filters, open-thermocouple detection, noise immunity, inputs for high accuracy temperature measurements from the thermocouple.
- NI 9215 analog input module – 4 channel, 100 kS/s, 16-bit resolution, $\pm 10\text{V}$, inputs for receiving the signals from the sensors.
- NI 9263 analog output module – 4 channel, 100 kS/s, 16-bit resolution, $\pm 10\text{V}$, 0-20mA, outputs for providing power to additional system peripherals.
- NI 9472 digital output module – 8 channel, 6-24V logic, 100 μs , outputs for generating PWM signals and switching tasks.



Figure 3.4: National Instruments DAQ hardware

The NI cDAQ was connected to a PC via USB, where the input signals were recorded and analysed and output signals were generated.

3.13 Software

The data collection and control was implemented using the National Instruments Labview software. Labview is a powerful graphical programming software tailored for data gathering and analysis. The PID control and PWM signal was generated within Labview and output through the DAQ module to the MOSFET switching circuit. The operation of the fans during cooling was also provided via the DAQ module. A user interface was created that allows the user to input the desired displacement for the controller to maintain and monitor the actuator's performance. The data was displayed on charts and recorded into a file.

3.14 Forced Cooling

The cooling time of the actuator wires was reduced using fans. Two DC brushless fans, 12V 0.12A, were positioned on the actuator base block beside the wire bundle. The NI digital output module requires an external DC power supply ranging from 6V to 30V. It was supplied with 12V and was thus capable of powering the fans directly. The control system only switched on the fans after actuation was complete, as having the fans constantly on would mean higher current requirements for heating.

3.15 Physical Structure

A concept was developed then improved and finalised. The design involves transferring the force and displacement produced by the SMA wires to a shaft. In the proposed design (Figure 3.5), the SMA wires are attached to a stationery block on one end and to a moveable block on the other end. The shaft is fixed on the moveable block and extended through the stationery block which also acted as guide. The entire configuration is fixed onto a firm base block.

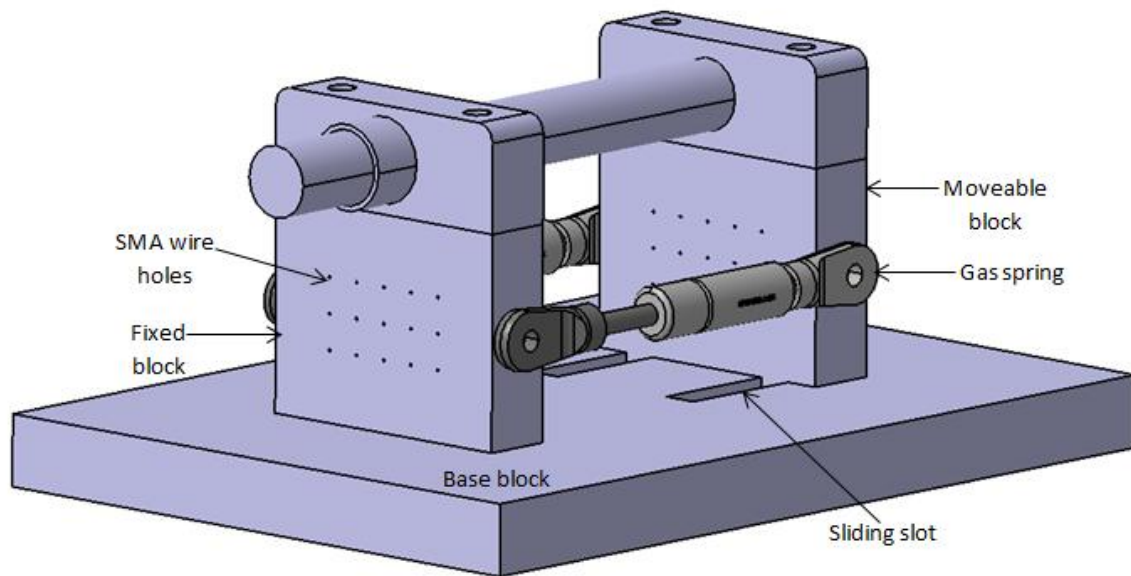


Figure 3.5: Actuator concept design

Two compression gas springs were screwed onto each block as shown to provide the bias force. The configuration also limits the freedom of movement to the required linear motion along one axis. The moveable block moved within slots.

This concept was improved by having the moveable block move along a fixed shaft instead of slots. This shaft is fixed onto the base block. A brass bush and lubrication was used to provide frictionless movement. Two springs were also deemed unnecessary and a single spring is sufficient to provide the bias force and limit the degrees of freedom to linear movement along the required axis. The final design is shown in Figure 3.6. The detailed engineering drawings for the parts can be found in Appendix B.

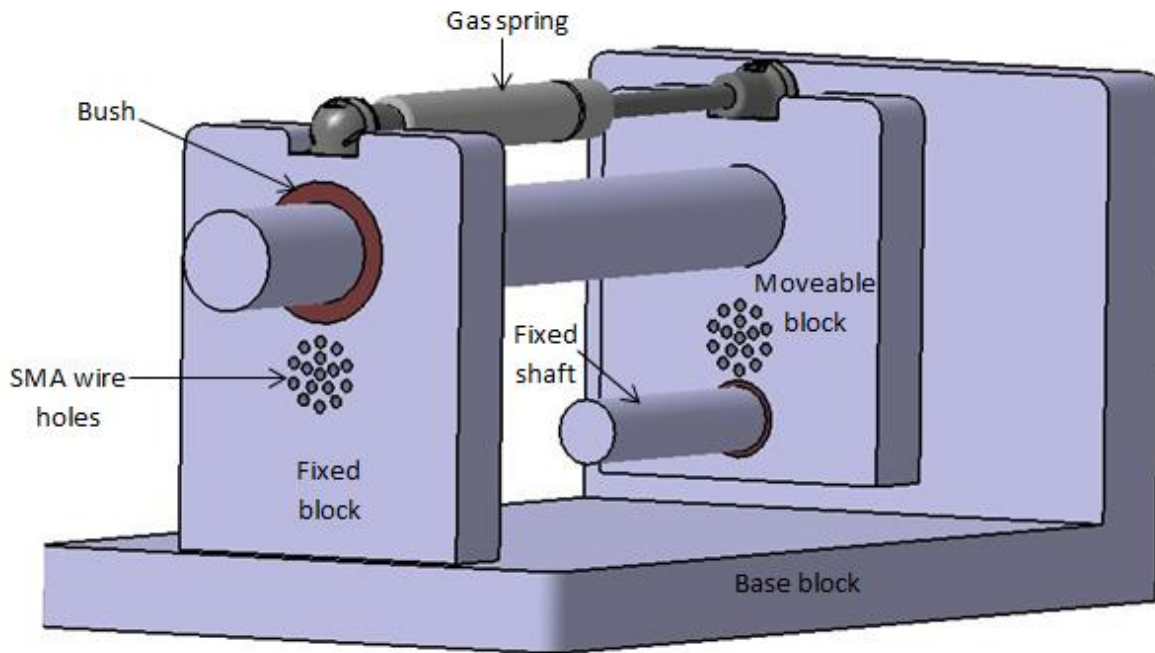


Figure 3.6: Actuator final design

The actuator structure was made from mild steel. This provided sufficient rigidity and strength. The entire structure occupied a space of 280x150x130 mm. A finite element analysis (FEA) was performed using Autodesk Inventor software. The FEA was implemented on the moveable block with the shaft, as this was the part that would experience the loads and subsequent stress. The actuator shaft had a diameter of 25mm and the yield strength of mild steel, 240MPa [50]. The calculated cutting force, the gas spring bias force and the SMA wire pull force were applied. Figure 3.7 shows the applied forces and constraints.

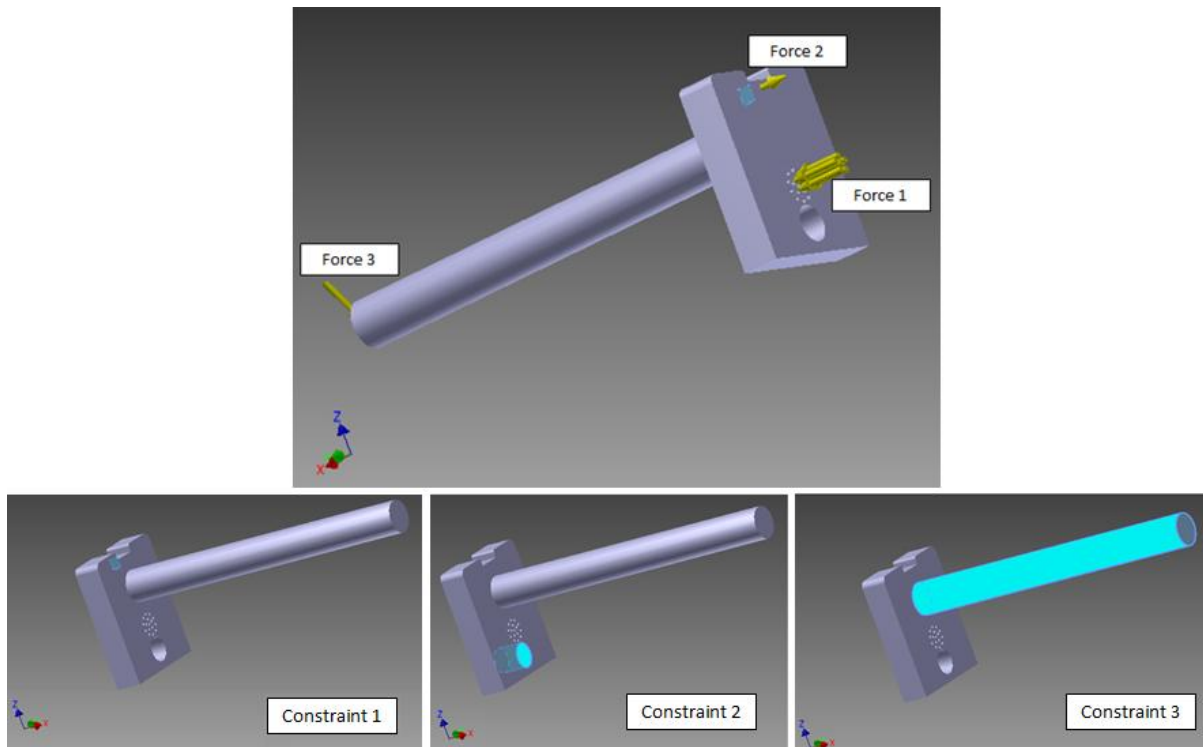


Figure 3.7: FEA applied forces and constraints

Force 1 is the 120N pulling force from the SMA wire bundle, Force 2 is the 50N bias force from the gas spring, and Force 3 is the 300N resultant cutting force. Constraint 1 is the hole where the gas spring was fixed, Constraint 2 is the hole on which the block moved along a shaft, and Constraint 3 is on the main shaft that moved through the guide. The constraints allowed movement in the direction of linear displacement.

The results, shown in the Figure 3.8, indicate a maximum stress of 5.712MPa on the block from the force of the wire bundle and a maximum displacement of 0.097 μ m at the front tip of the shaft from the cutting force. Refer to Appendix C for a detailed FEA report.

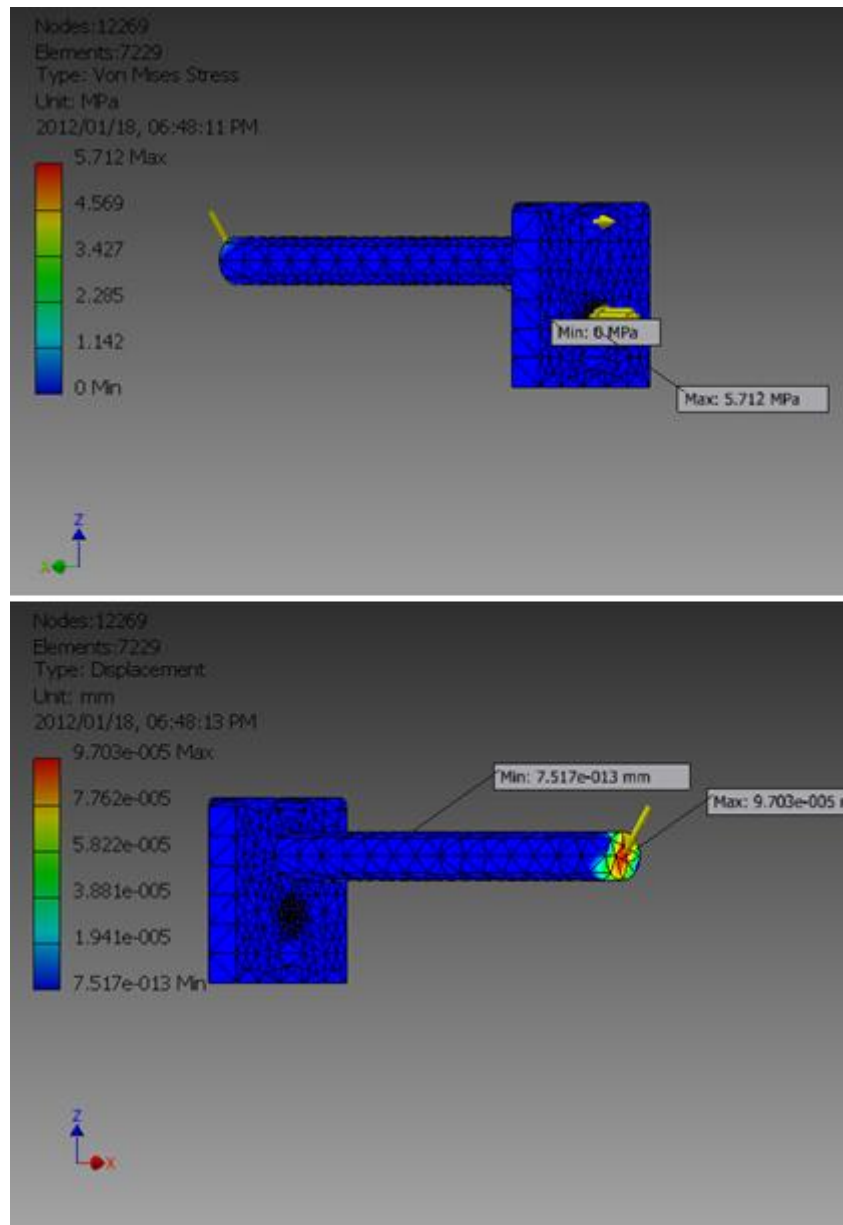


Figure 3.8: FEA analysis of actuator shaft

3.16 Actuator Control System

The entire system block diagram is depicted in Figure 3.9 showing all the major system components.

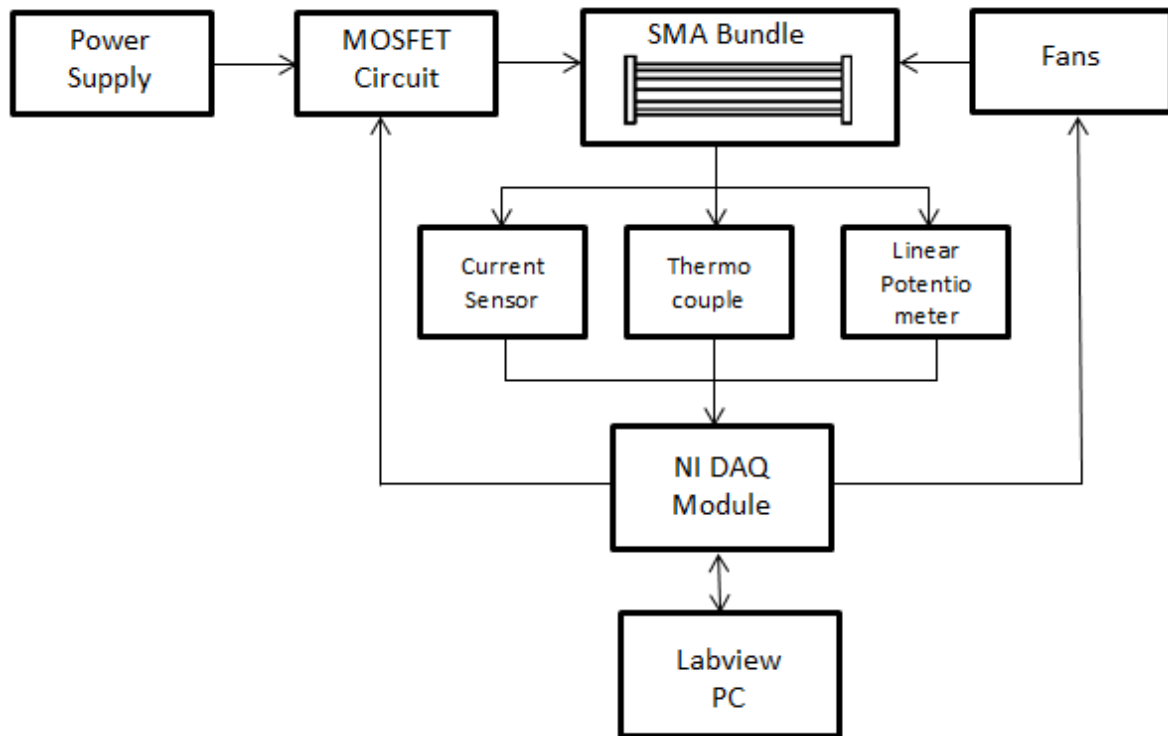


Figure 3.9: Actuator system block diagram

The circuit diagram is depicted in Figure 3.10, showing all the electrical connections of the system components.

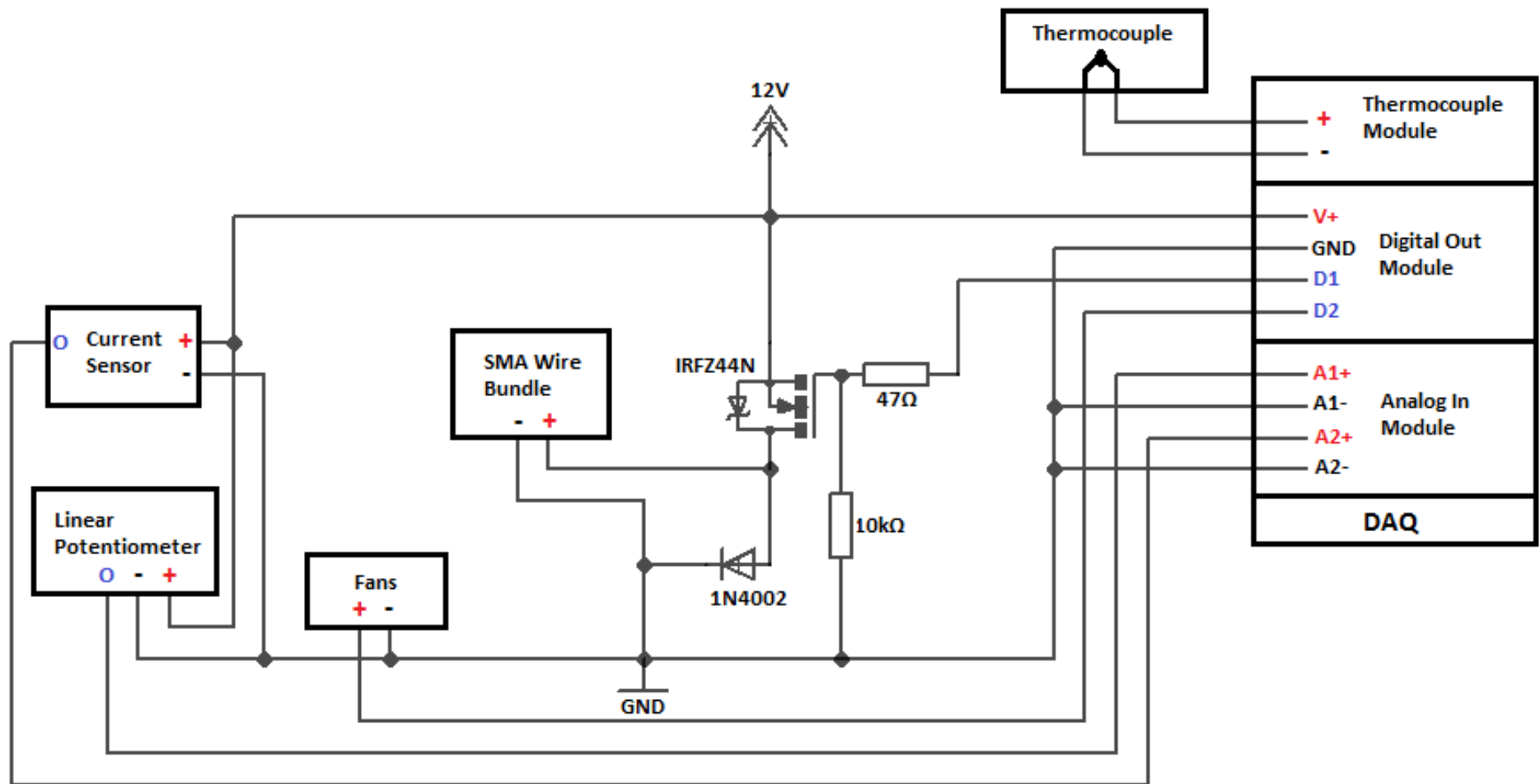


Figure 3.10: Actuator system circuit diagram

Chapter 4. Experiments and Testing

4.1 Test Stand

A test stand was initially setup to observe the wire behaviour before the actual actuator system was constructed. The test stand consisted of a single wire working against a tension spring as shown in Figure 4.1. The wire was 0.381mm in diameter and 200mm in length (the same to be used in the actuator). The test stand had a displacement scale with a pointer and, in addition, a thermocouple was attached to the wire to monitor temperature.

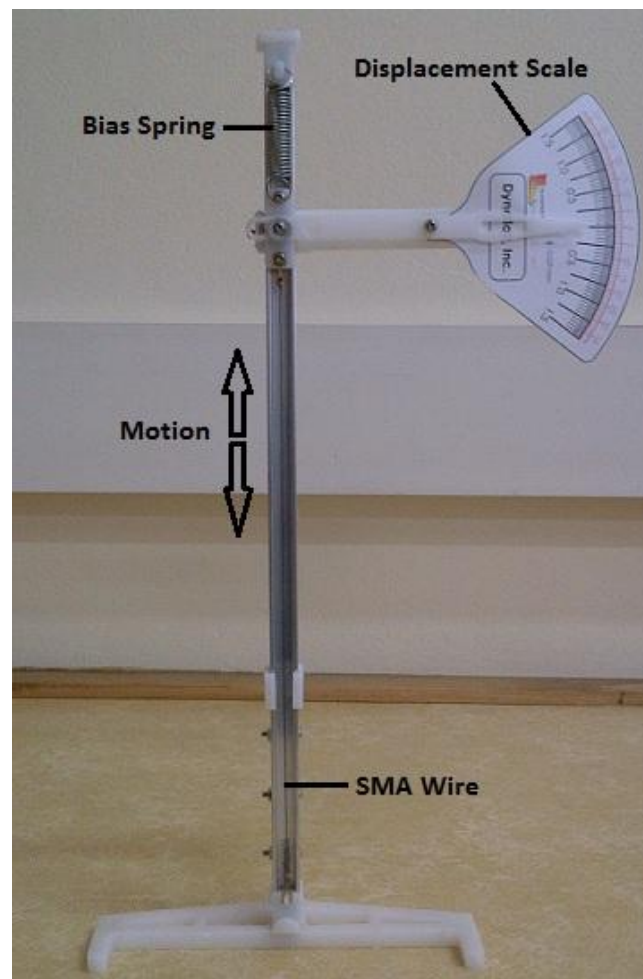


Figure 4.1: Test stand setup

The wire was heated and held at maximum displacement for some time then allowed to cool back to ambient temperature. Precaution was taken not to overheat the wire so a temperature of 100°C was selected as the power supply cut off point.

The wire, with a resistance of 1.66Ω , was supplied with 3V, 1.8A. The maximum displacement on the scale was noted and the temperature change with time was recorded and graphed.

4.2 Experimental Setup

The designed actuator setup was constructed as shown in Figure 4.2. The thermocouple was attached to a SMA wire with heat shrink. The linear potentiometer was fixed onto the base block with its extendable rod screwed to the moveable block to measure displacement. The current sensor was placed on a PCB with the MOSFET circuit. The entire experimental setup is shown in Figure 4.3. Open loop and closed loop performance tests were carried out to determine the SMA bundle characteristics.

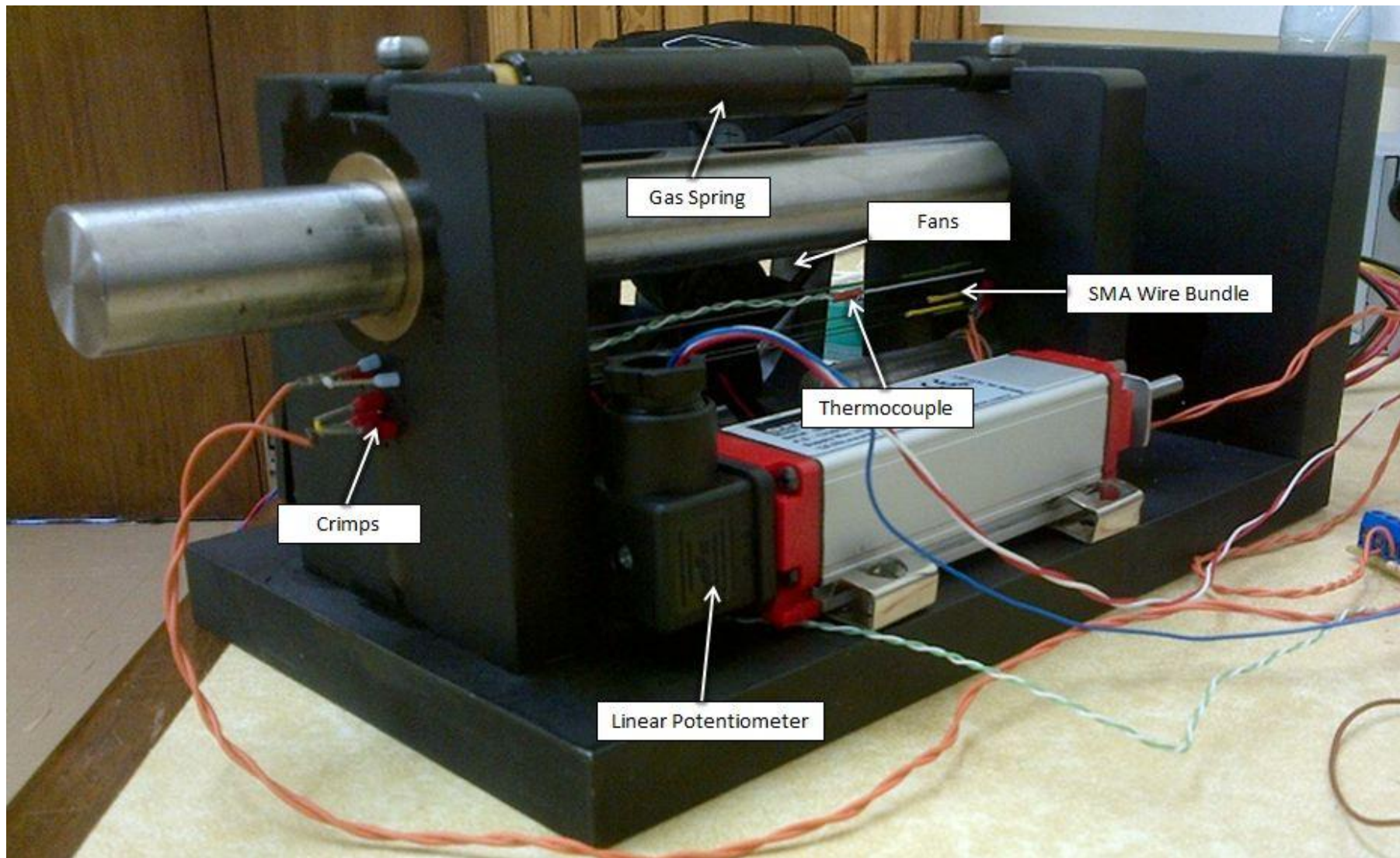


Figure 4.2: Actuator setup

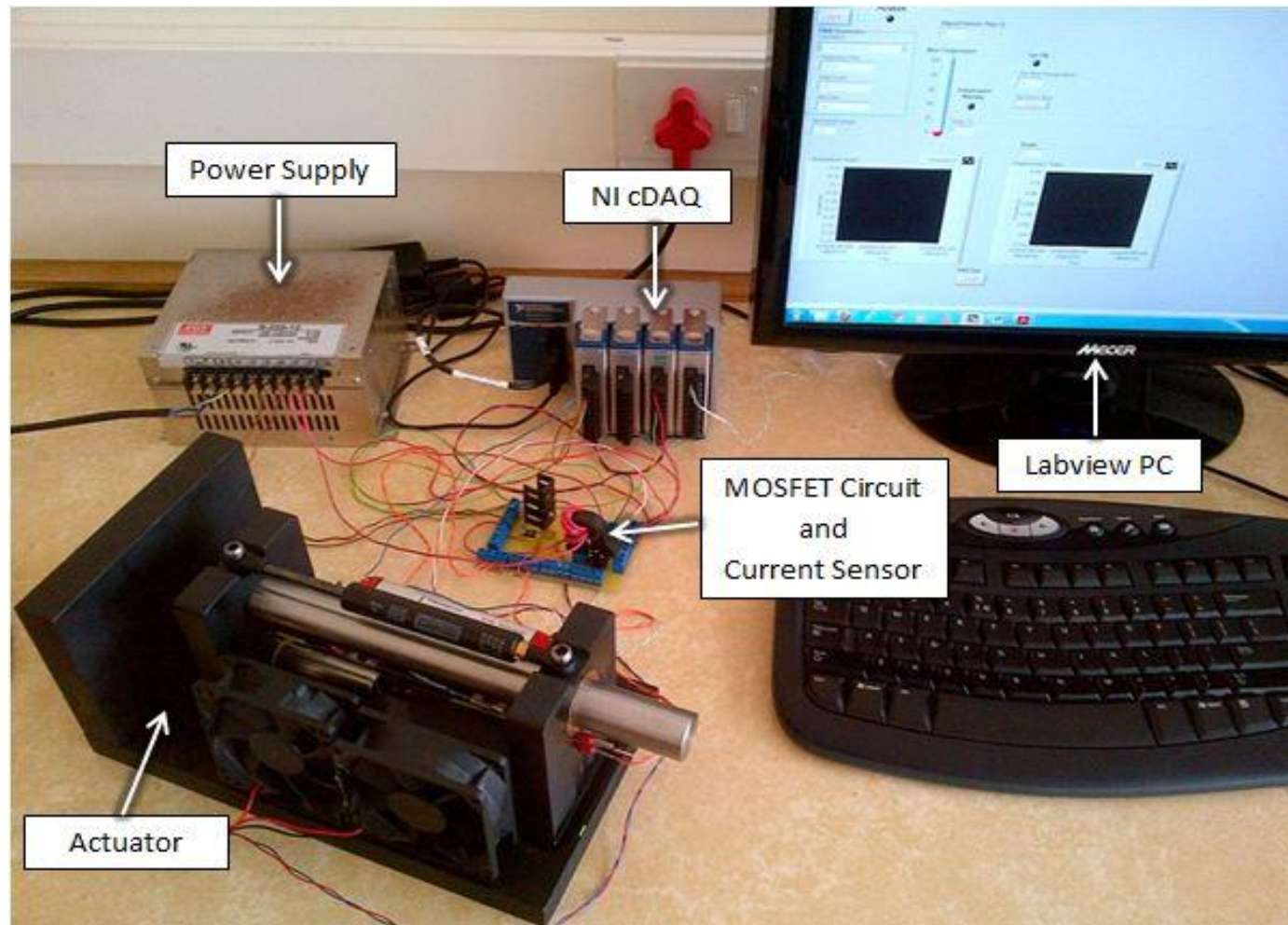


Figure 4.3: Experimental setup

After the setup was complete, the initial design parameters and requirements were finalised. The power supply provided a steady 12V. Thus, the current sensor and linear potentiometer calculations and readings were deemed accurate. A safe maximum activation current was selected as 2A for each wire, giving a total wire bundle current of 4A and a maximum voltage of 10V. The 6-wire bundle, 200mm long, with two electrically parallel wires each 600mm (3x200mm) long, had a combined resistance of 2.5Ω.

$$R = \frac{8.3\Omega/\text{m} \times 0.2\text{m} \times 3}{2} = 2.5\Omega$$

The Labview open loop user front panel is shown in Figure 4.4. The duty cycle (a percentage of 12V) was entered by the user to achieve a required voltage. The temperature at which the fans turn off during cooling could also be input. The user can turn off the power at any time with the Power OFF button and stop the data collection with the DAQ Stop button which also stops the program. Three different LEDs were present which indicated when the power was on, when the fans were on and a warning when the temperature exceeded 80°C.

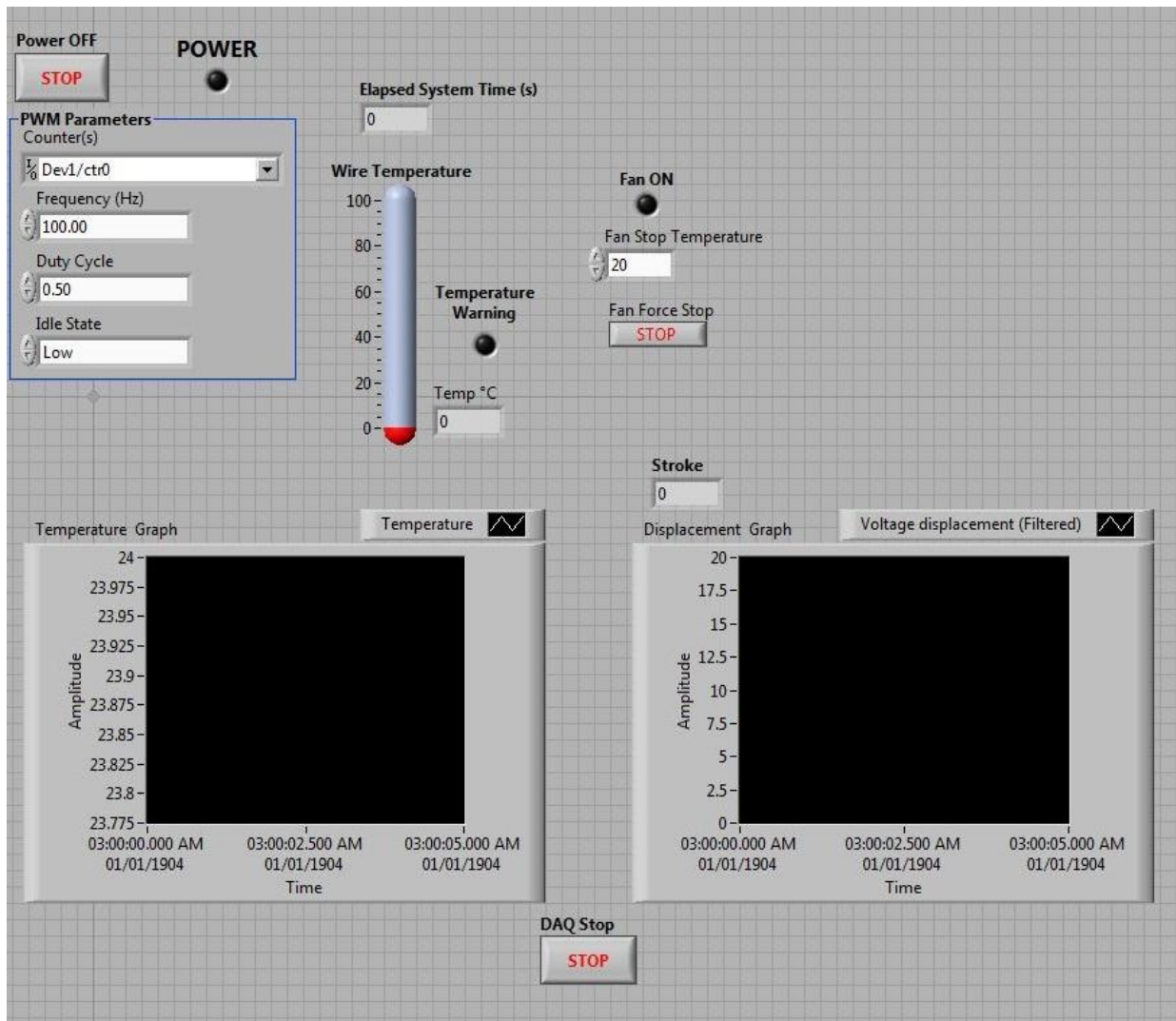


Figure 4.4: Labview open loop front panel

The open loop tests involved applying a selected voltage for a given time to observe the actuator's response. The temperature and displacement were monitored and recorded.

Three main tests were carried out:

1. The maximum stroke under various voltages: The actuator was supplied with 3V until no change in displacement was observed. At this point the power supply was cut off and the wire bundle was allowed to cool back to room temperature. This was repeated for 5V, 7V and 9V.

2. The change in cooling time and retraction time under forced air: The actuator was supplied with 3V, heated for 10 seconds and allowed to cool under ambient temperature until the wires reached room temperature. The same voltage was supplied but forced cooling was applied. This was repeated for 5V, 7V and 9V.
3. The actuator's response to radial forces on the shaft: The actuator was positioned vertically, as shown in Figure 4.5. The actuator was supplied with 3V until no change in displacement was observed. At this point the power supply was cut off and the actuator was allowed retract back to its initial position. This test was repeated but with a 500g weights placed on the shaft. The 20N weight of the moving block remained constant and was negligible when comparing the response with various weights.

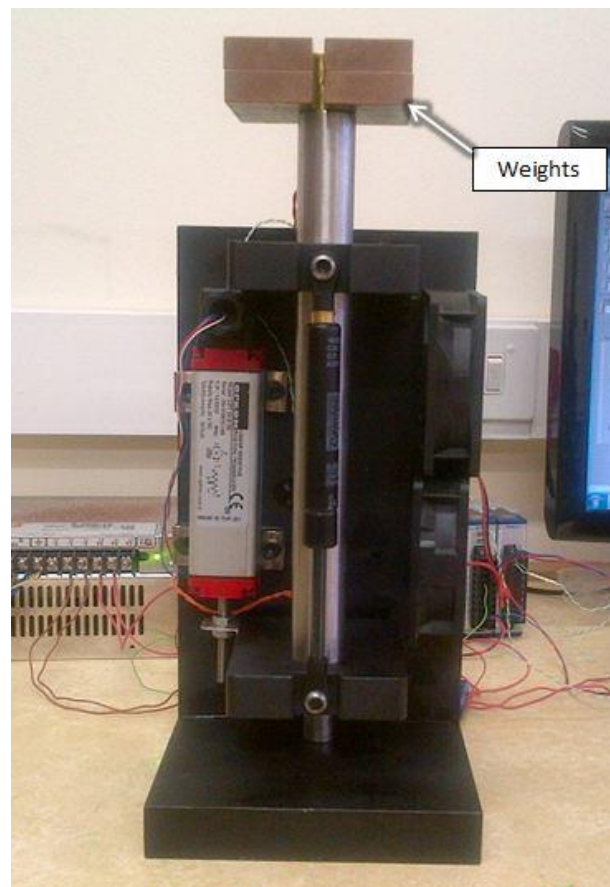


Figure 4.5: Force experiment setup

The closed loop user front panel, shown in Figure 4.6, was similar to the open loop panel with the addition of a Desired Displacement and PID constants inputs. The detailed block diagrams of the open loop and closed loop Labview programs are shown in Appendix A.

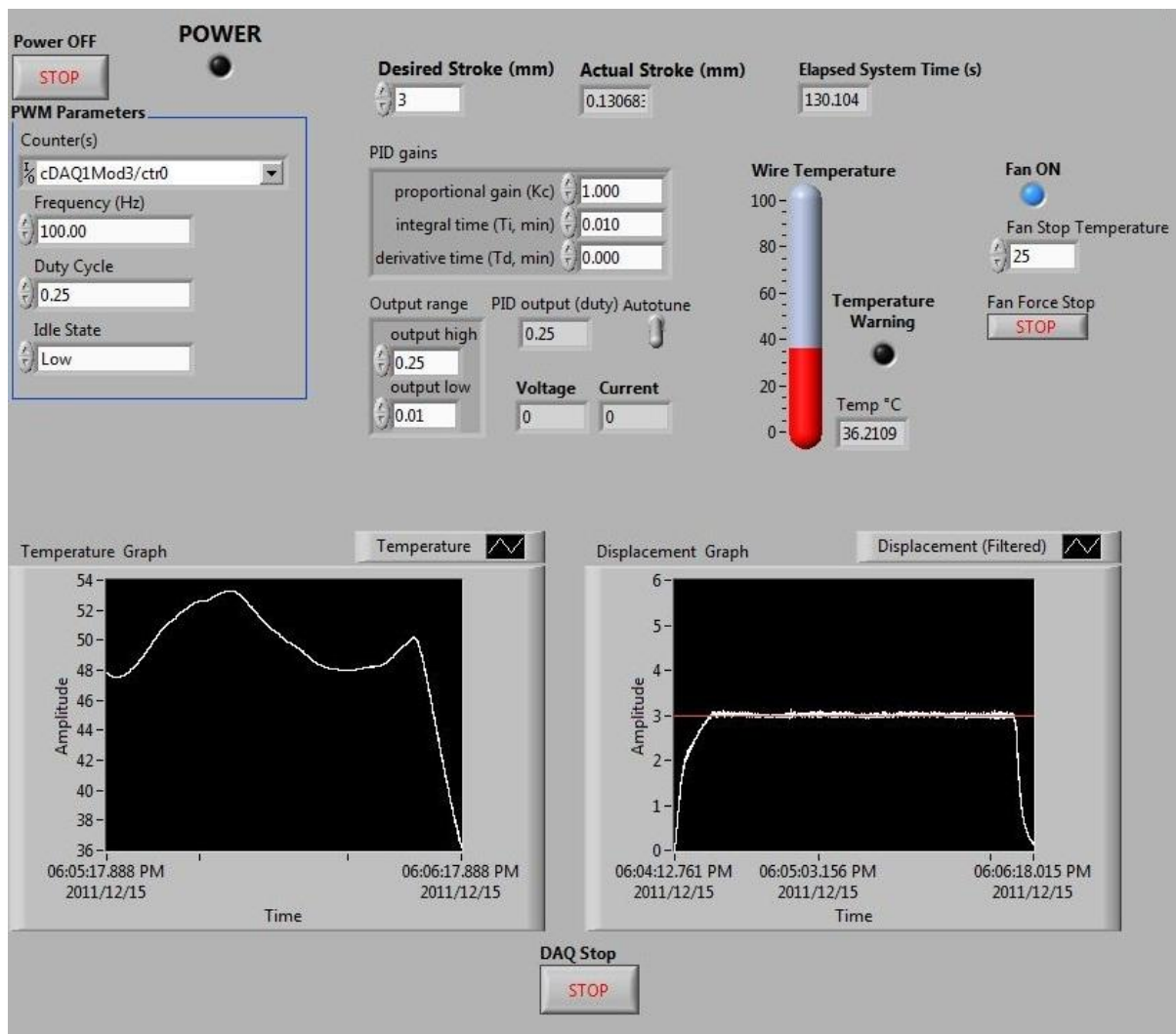


Figure 4.6: Labview closed loop front panel

The closed loop tests involve applying PID control to maintain a user selected displacement based on feedback from the displacement sensor. The actuator was supplied with a selected voltage and its performance in maintaining various displacements for approximately 10 seconds was recorded and graphed. The fans were used to assist cooling after actuation.

The optimum PID controller constants must be determined before performing the closed loop tests. The PID autotune feature within Labview was used for this task. The Autotuning Wizard steps the user through the autotuning process and outputs new values for the PID gains when complete. The autotuning tool uses Ziegler and Nichols' heuristic methods to determine the PID gains [51]. The Autotuning Wizard is shown in Figure 4.7.

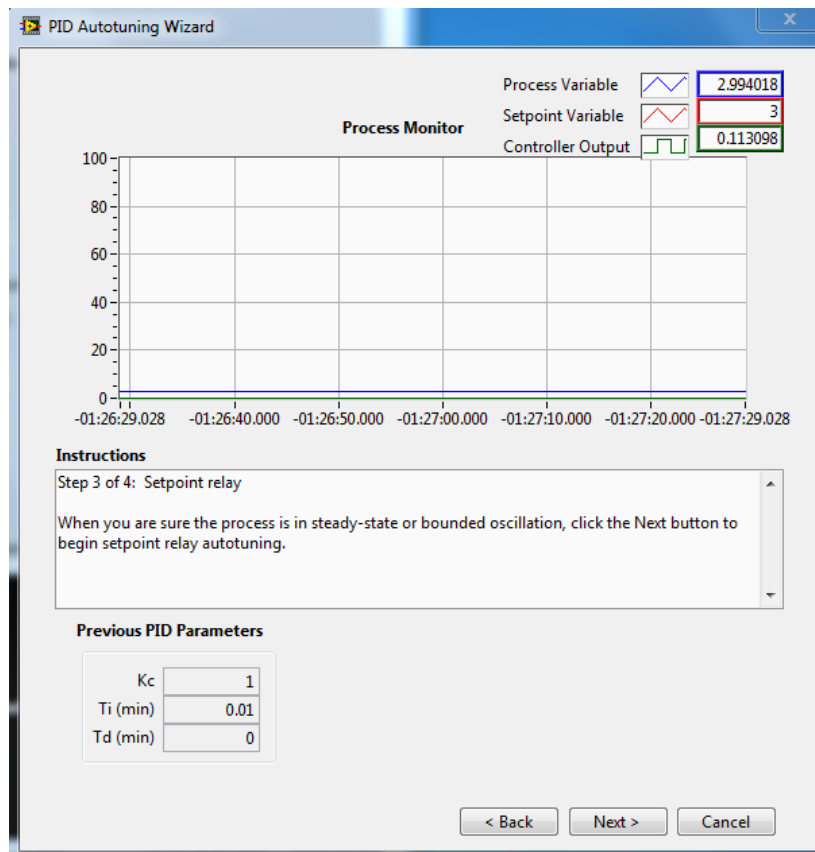


Figure 4.7: Labview PID autotuning wizard

The mean errors in maintaining the required displacements were calculated to provide a measure of accuracy. The following voltage-displacement combinations were tested:

1. 3V – 1mm, 2mm, 3mm, 4mm and 5mm
2. 5V – 1mm, 2mm, 3mm, 4mm and 5mm
3. 7V – 1mm, 2mm, 3mm, 4mm and 5mm
4. 9V – 1mm, 2mm, 3mm, 4mm and 5mm

Based on the findings, the recommended settings to operate the actuator was determined.

4.3 Safety and Operation

Before operating the actuator system, a few safety checks must be performed.

1. There must be continuity between both ends of the SMA wire bundle. The SMA wires must be well crimped to ensure the tension does not cause them to slip out of the crimp and lose contact with the wires supplying current.
2. It is highly crucial that the SMA wire bundle is isolated from the physical structure. Though the wire is insulated and the structure has a coat of paint, it is important to check for any shorts. In addition, the structure must be earthed.
3. The power supply must have a steady 12V. Any large deviation or fluctuations will lead to incorrect readings.
4. The shafts must be well lubricated to aid in smooth movement.
5. The current sensor and linear potentiometer should be producing an output voltage into the DAQ with the power supply on and the actuator on standby.

Once the safety checks are complete the actuator may be operated. Refer to Figure 4.8 for the labels highlighted in red.

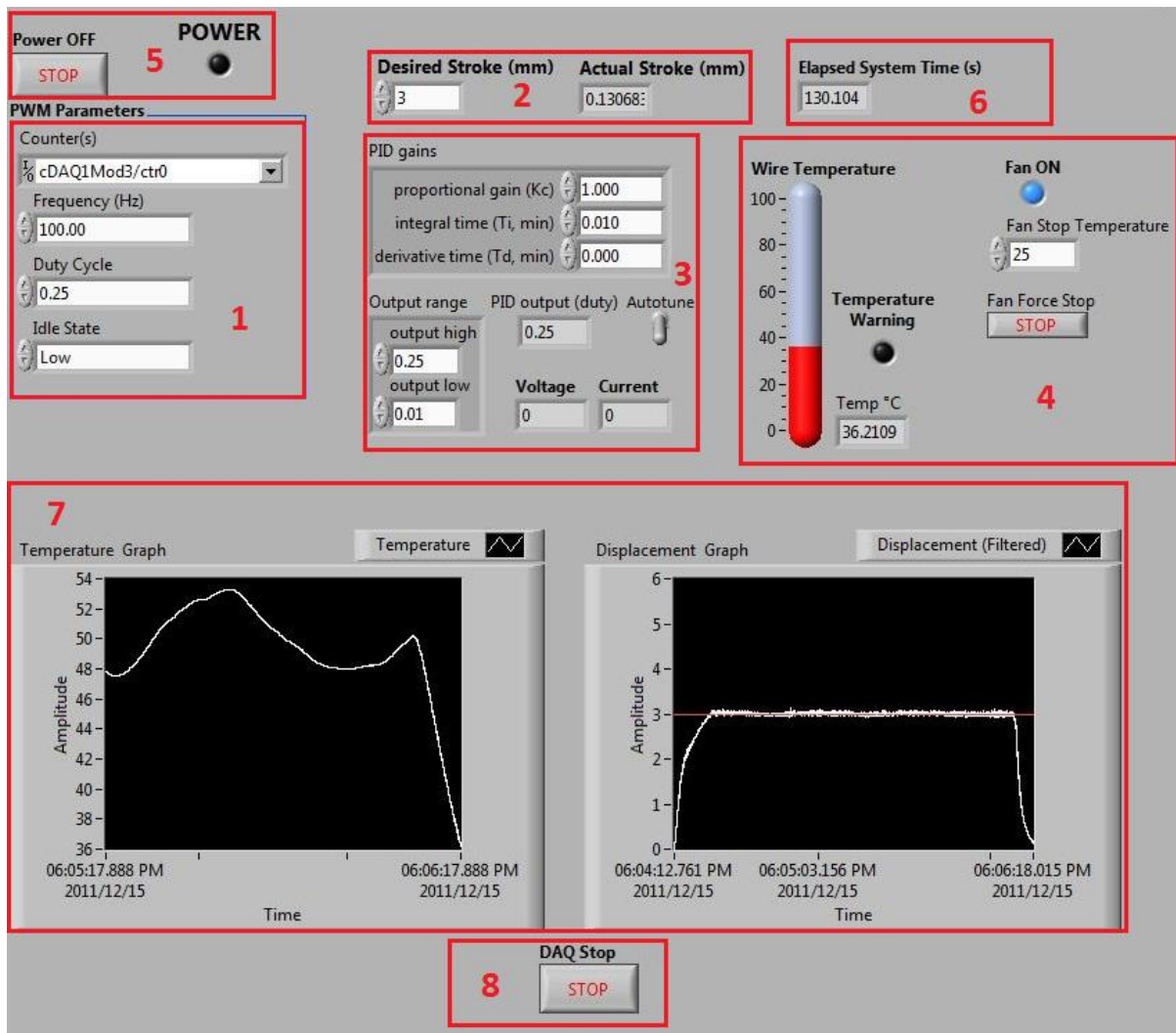


Figure 4.8: Labelled user front panel

1. The PWM parameters must be entered. Label 1 shows the default settings that should be entered for the Counter cDAQ1Mod3/ctr0, Frequency 100Hz and Idle State Low. The required voltage is entered as a percentage of 12V in the Duty Cycle tab.
2. The desired displacement setpoint is entered under the Desired Stroke tab, label 2. A value between 1mm to 5mm should be entered. The actual stroke of the actuator can be monitored under the Actual Stroke tab.
3. The PID constants are entered under the PID Gains tab, label 3. These are by default set as Proportional Gain 1, Integral Time 0.01, Derivative Time 0. The constants are

automatically tuned using the Autotune switch. This provides optimal constants for the system. The output range is the upper and lower limit of the duty cycle value that the PID controller outputs. This value varies the power to the SMA wire bundle to achieve and maintain the desired position entered. Hence, the Low is entered as 0.01 and the High should be the same value that was entered for Duty Cycle in Label 1. The controller's output, the voltage across the wire bundle and current being drawn by the wire bundle can be monitored under the PID Output, Voltage and Current tabs, respectively.

4. The temperature at which the fans will turn off during cooling is entered under the Fan Stop Temperature tab, label 4. This value is entered as 28°C by default. It is advisable to enter a value 3-4°C above room temperature. The temperature of the SMA wire is monitored on the graphical thermometer and the numerical display beside it. An LED is present which blinks yellow when the temperature exceeds 80°C to provide a warning to the user that overheating is imminent. A blue LED indicates when the fans are on and a button is also present should the fans need to be turned off manually.
5. The power supply can then be switched on and the program run. Once started, the Power LED (label 5) turns green to indicate the PWM is being generated and power is being supplied to the SMA wire bundle.
6. While the actuator is in operation, the elapsed time (label 6) is displayed and charts (label 7) illustrate the actuator's response.
7. Once the operation is complete, the Power Off button (label 5) is pressed to disable the PWM signal, cutting power to the wire bundle. The fans are automatically activated and data is still collected and displayed.

8. When the wires have cooled down to room temperature and the actuator has retracted to its original position, the DAQ Stop button (label 8) is pressed and the program stops running.

Chapter 5. Results and Discussions

5.1 Test Stand

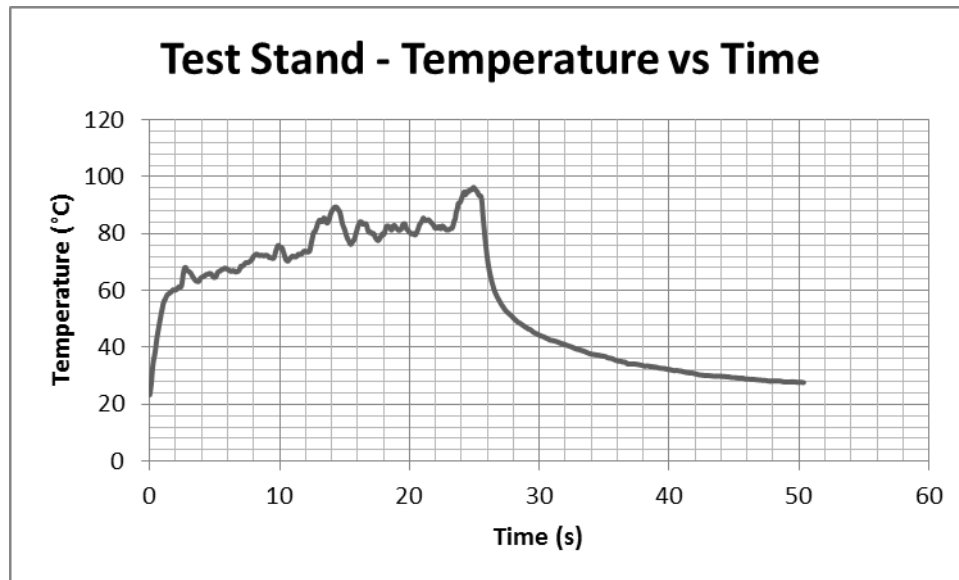


Figure 5.1: Test stand temperature with time

The maximum displacement is recorded as 6mm (3% stroke). The non-linearity is seen in Figure 5.1. with the hysteresis represented as the curves between 0-25s while heating and 25-40s while cooling. Upon heating, the wire shows an immediate response contracting and pulling the spring downwards. The maximum stroke is achieved in approximately 2 seconds. Similarly, as soon as the power was cut off, the wire immediately began to revert to its original position with the spring pulling it back upwards. The wire takes approximately 10 seconds to return to its initial position. The wire reached an austenite finish temperature at 60°C in 2 seconds, which corresponds with the time the wire took to reach maximum stroke. The short linear region present between 30°C and 60°C is the area of focus to achieve accurate PID control during heating.

5.2 Open Loop Experiments

5.2.1 Maximum Stroke Tests

The first open loop test carried out was to determine the maximum stroke length at various supply voltages. Power was supplied to the actuator until the stroke became fairly constant then allowed to cool without fans. This test was performed for 3V, 5V, 7V and 9V, which when considering the wire bundle resistance, produced a current of 1.2A, 2A, 2.8A and 3.6A, respectively. The displacements and the temperatures were monitored and the results were recorded and graphed.

The graphs below illustrate the temperature change with time (Figure 5.2), displacement change with time (Figure 5.3) and the displacement against temperature change (Figure 5.4) for 3V.

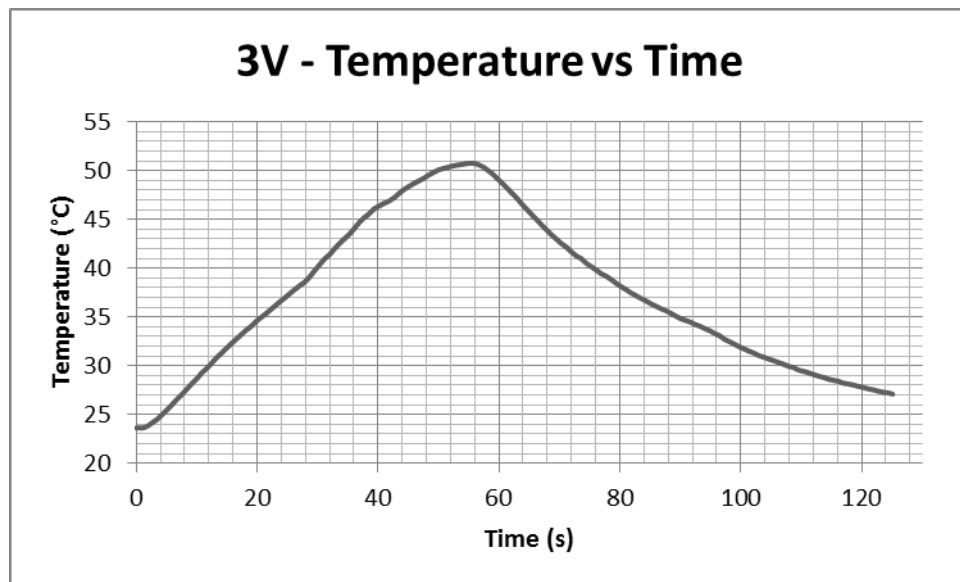


Figure 5.2: 3V temperature with time

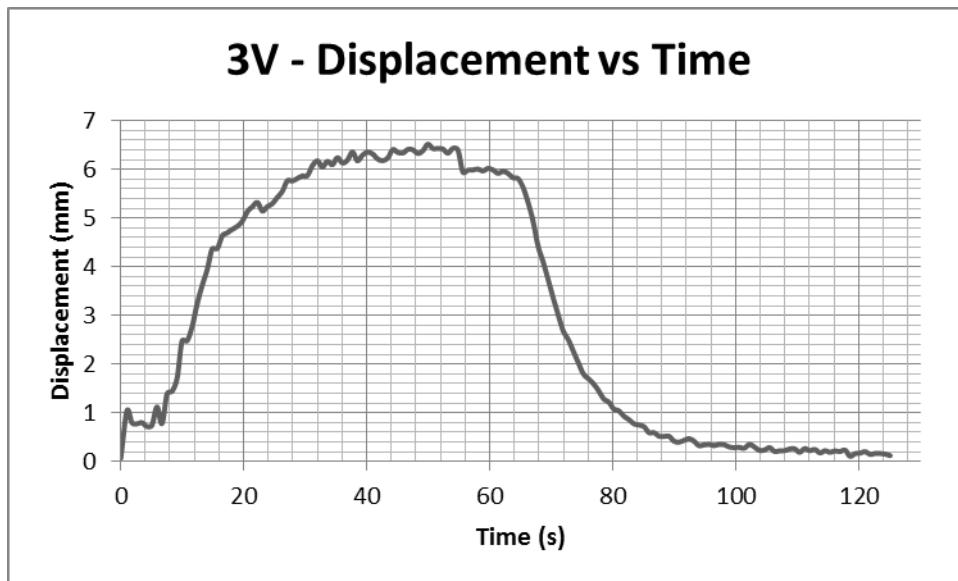


Figure 5.3: 3V displacement with time

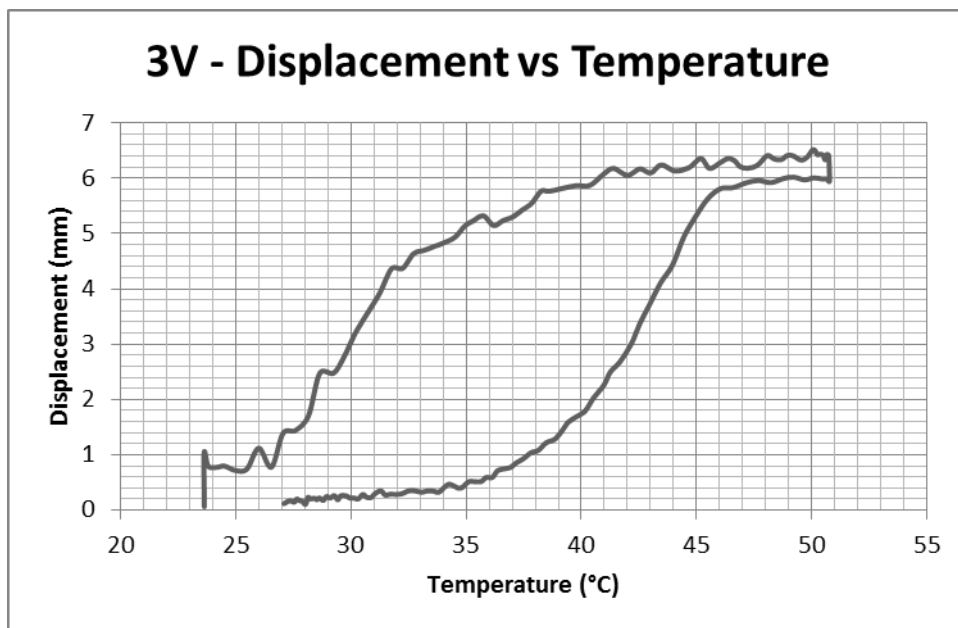


Figure 5.4: 3V displacement with temperature

When supplied with 3V, the wire bundle achieves a maximum temperature of 50°C and a maximum stroke of 6.5mm (3.3%) in 50 seconds. The displacement plotted against temperature shows the expected hysteretic response.

The graphs below illustrate the temperature change with time (Figure 5.5), displacement change with time (Figure 5.6) and the displacement against temperature change (Figure 5.7) for 5V.

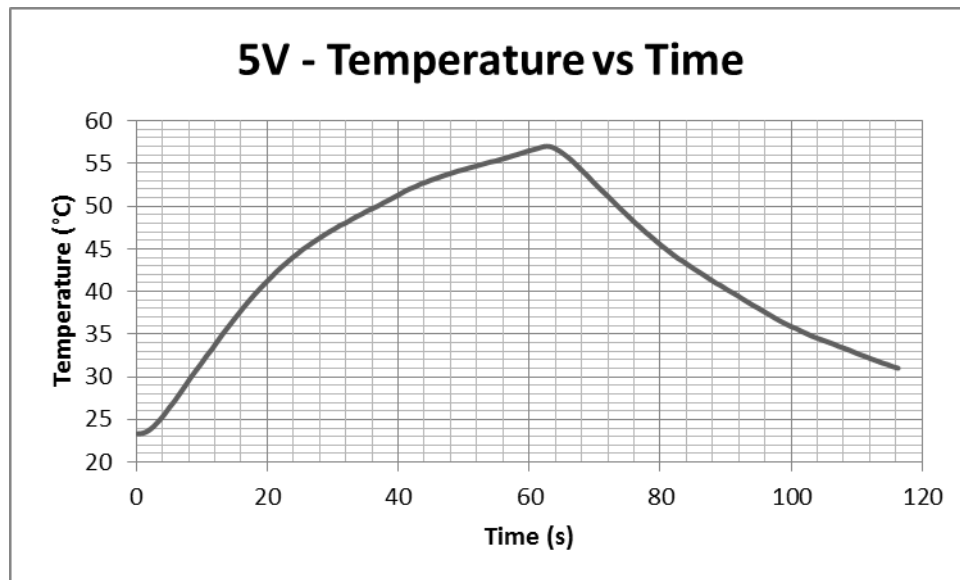


Figure 5.5: 5V temperature with time

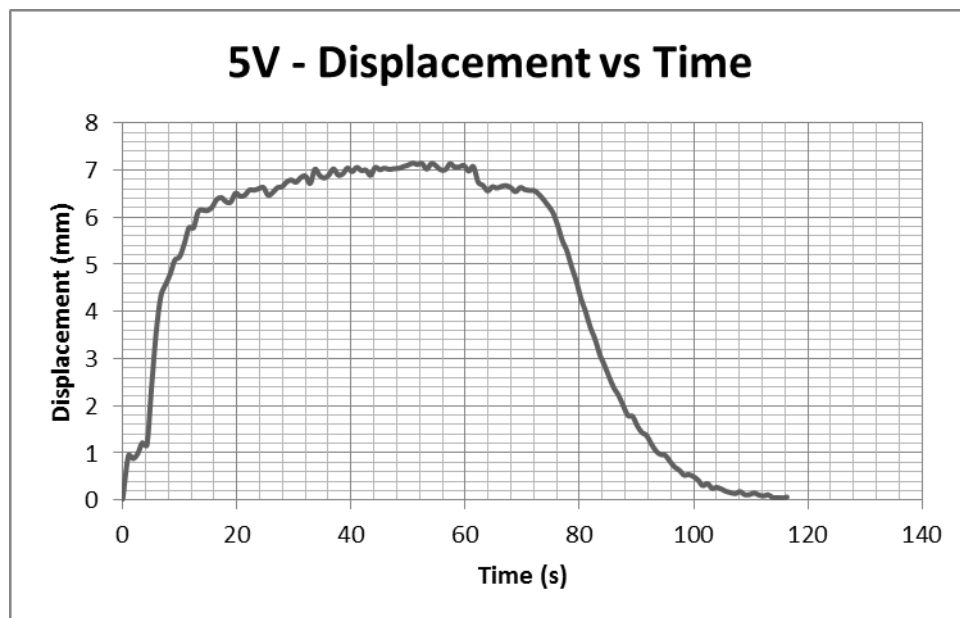


Figure 5.6: 5V displacement with time

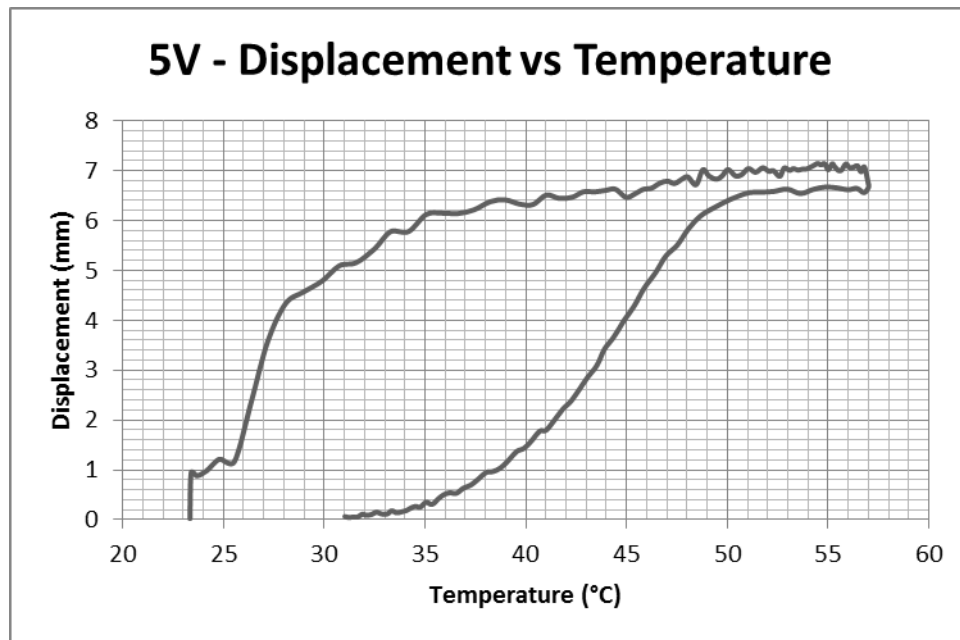


Figure 5.7: 5V displacement with temperature

The wire bundle achieves a maximum temperature of 57°C and a maximum stroke of 7.1mm (3.6%) in 50 seconds when supplied with 5V. The expected hysteresis is shown when the displacement is plotted against temperature.

The graphs below illustrate the temperature change with time (Figure 5.8), displacement change with time (Figure 5.9) and the displacement against temperature change (Figure 5.10) for 7V.

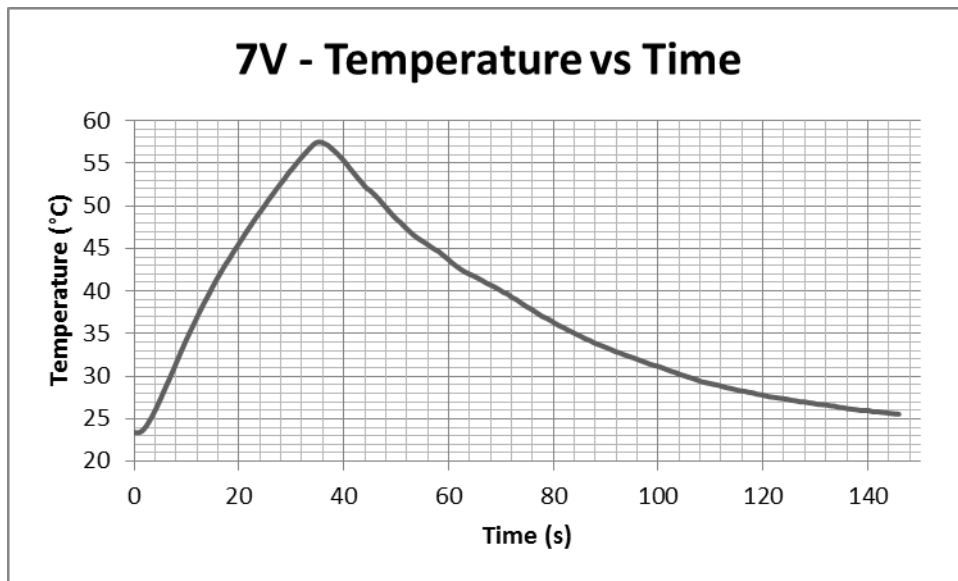


Figure 5.8: 7V temperature with time

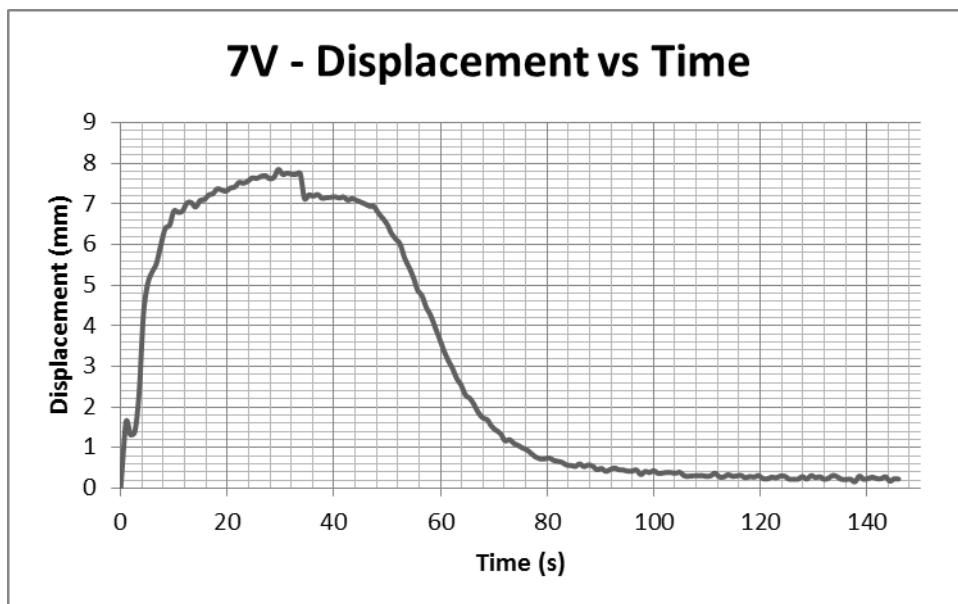


Figure 5.9: 7V displacement with time

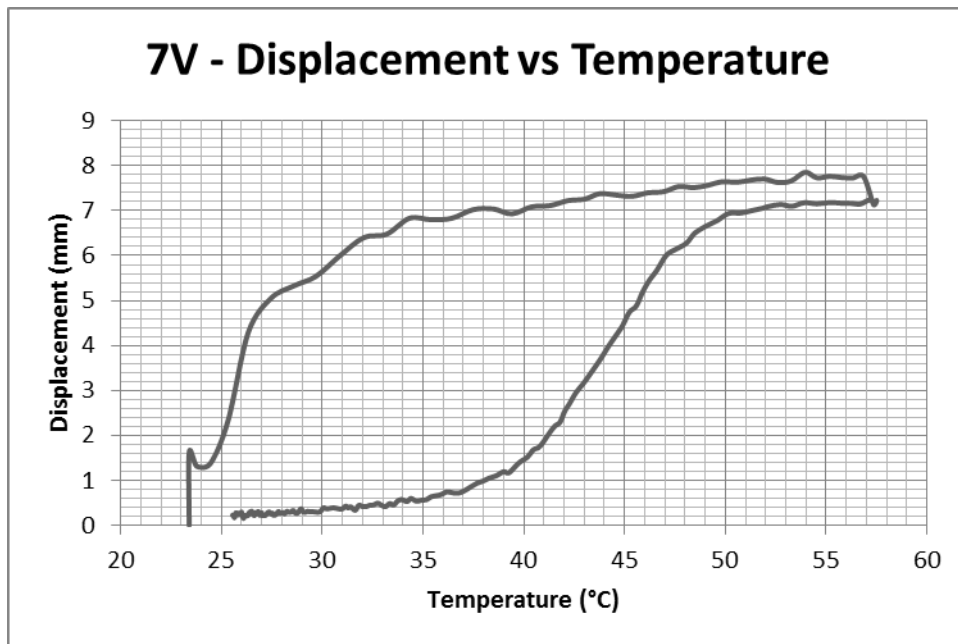


Figure 5.10: 7V displacement with temperature

When supplied with 7V, the wire bundle reaches a maximum temperature of 57°C and a maximum stroke of 7.8mm (3.9%) in 30 seconds. A similar hysteresis is seen when the displacement is plotted against temperature.

The graphs below illustrate the temperature change with time (Figure 5.11), displacement change with time (Figure 5.12) and the displacement against temperature change (Figure 5.13) for 9V.

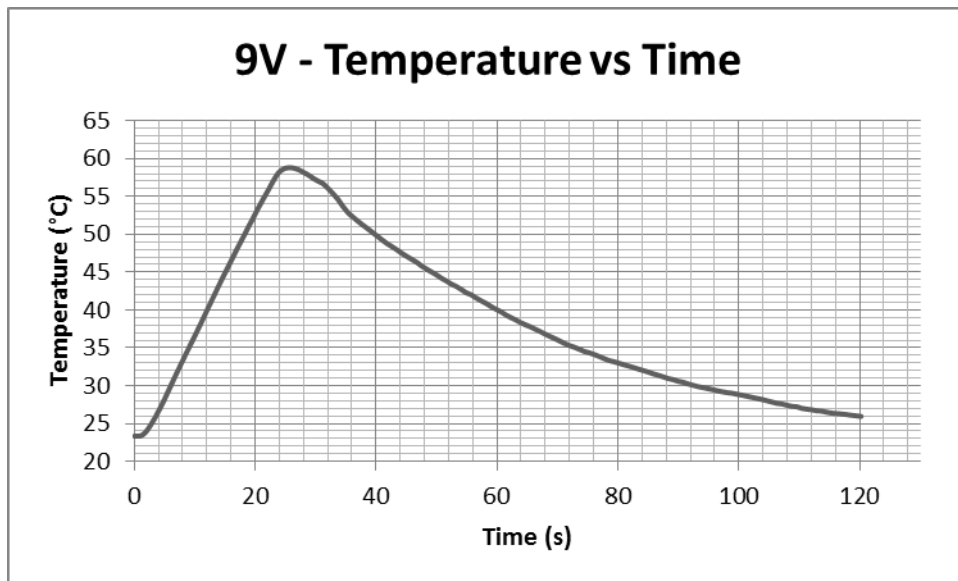


Figure 5.11: 9V temperature with time

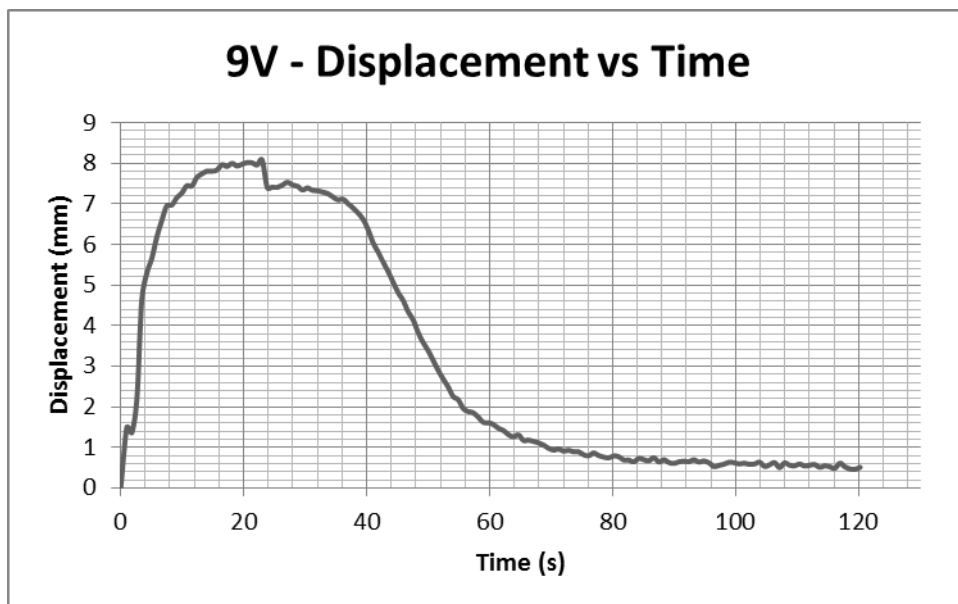


Figure 5.12: 9V displacement with time

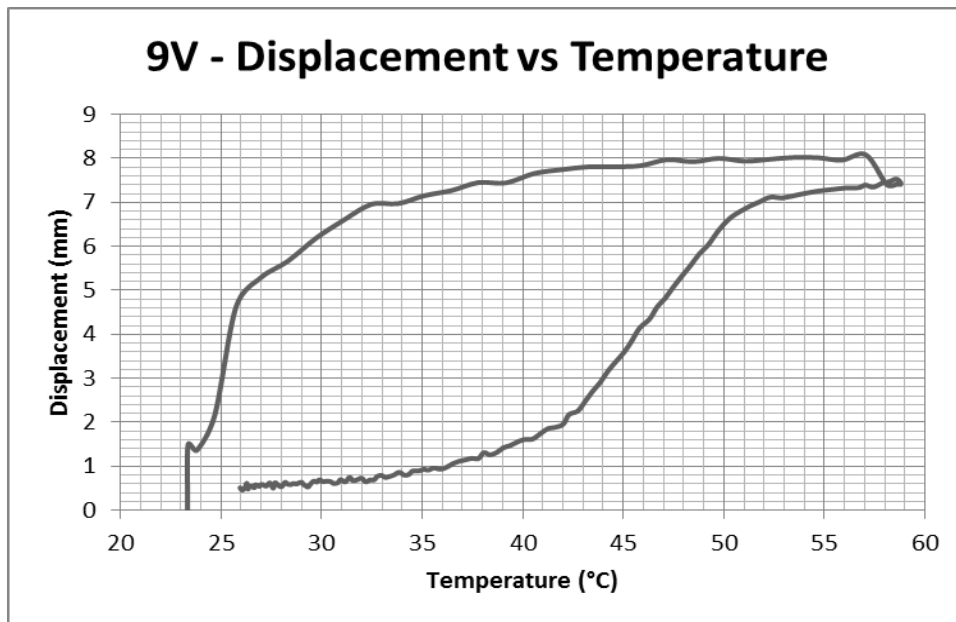


Figure 5.13: 9V displacement with temperature

The wire bundle achieves a maximum temperature of 59°C and a maximum stroke of 8mm (4%) in 18 seconds when supplied with 9V. The hysteretic response is seen with the displacement plotted against temperature.

The four voltages were plotted on the same graph for comparison (Figure 5.14, Figure 5.15 and Figure 5.16).

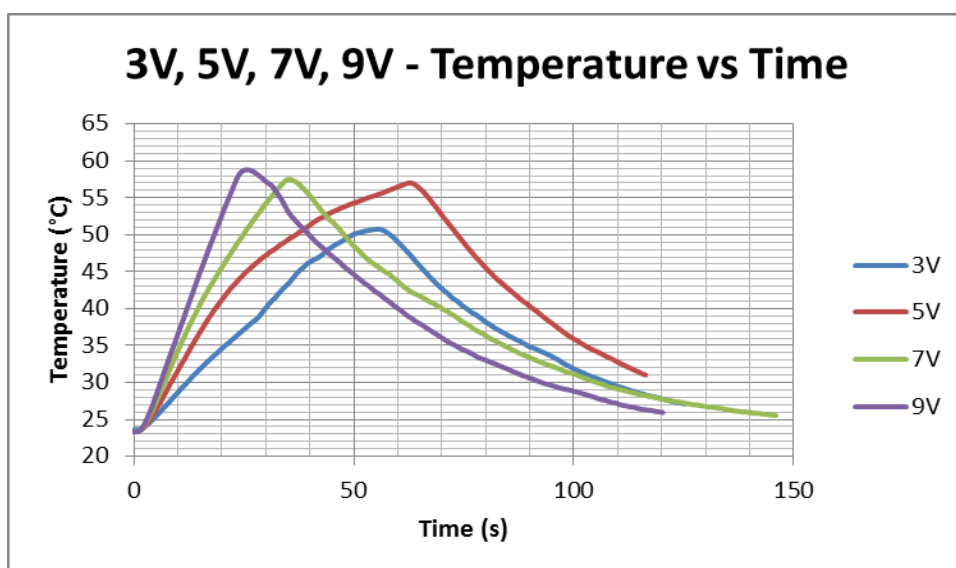


Figure 5.14: 3V, 5V, 7V, 9V temperature with time comparison

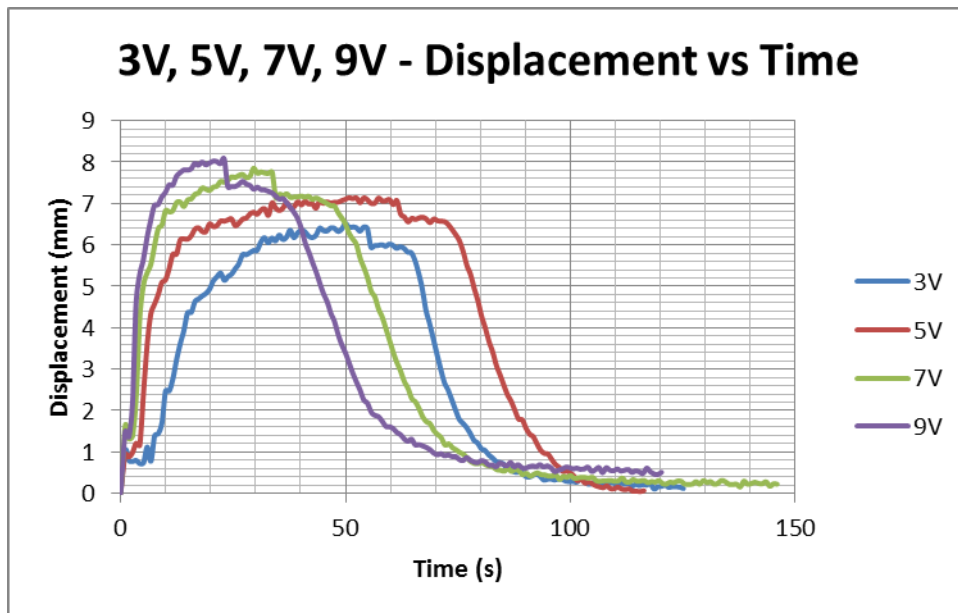


Figure 5.15: 3V, 5V, 7V, 9V displacement with time comparison

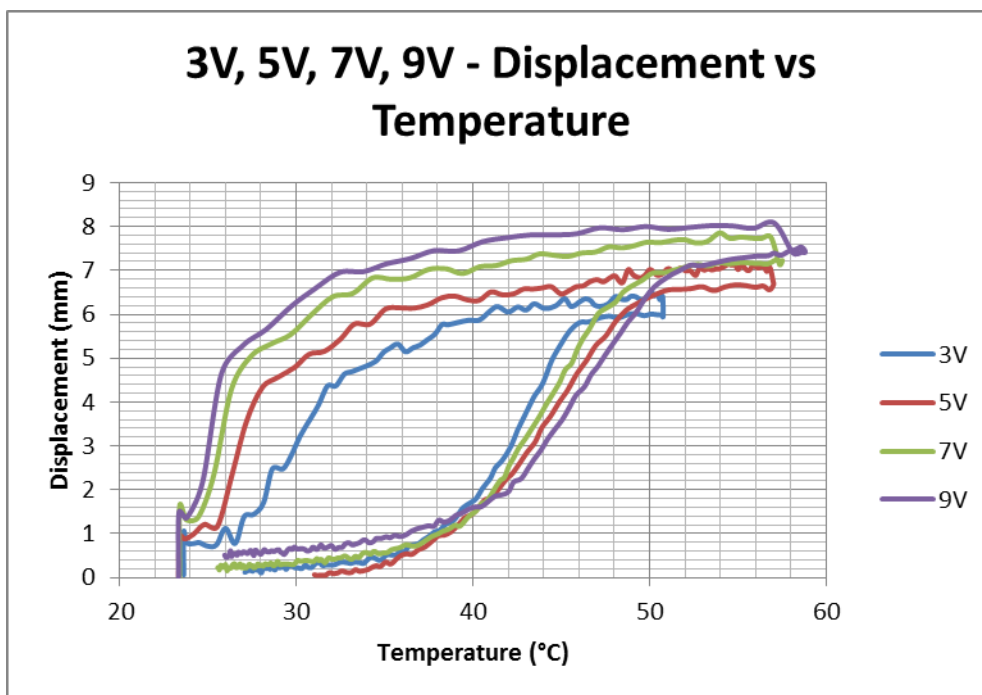


Figure 5.16: 3V, 5V, 7V, 9V displacement with temperature comparison

The results reveal the non-linear characteristic of the actuator. The graphs show the temperature rate of increase and temperature maximum being higher with increase in voltage. A similar trend is produced with the displacement. The higher voltages produced greater rate of increase in displacement and greater maximum displacement. The initial

delay before the actuator responds is also reduced with the increase in voltage. These trends are due to the higher currents produced with higher voltages which result in faster heating. The results by Reynaerts and Van Brussel [8] showed similar displacement characteristics with increase in supply voltage.

These trends create a wider hysteresis loop with increase in voltage meaning the critical phase temperatures are achieved faster, as the austenite start and finish temperatures appear lower and the martensite start and finish temperatures appear higher, with increased voltage.

An almost linear slope is observed as the displacement increases to the maximum during heating. Saturation behaviour seemed to occur with higher voltages. An increase in voltage shows a small change in maximum displacement with the higher voltages. A difference of 0.2mm occurs between 7V and 9V while a difference of 0.6mm occurs between 3V and 5V. This shows there is loss in efficiency at maximum displacement with higher voltages. This is also evident with the temperature curves. The 7V and 9V show a sharper rise in temperature with minimal increase in maximum displacement. The results by Mosley et al. [48] showed a similar saturation phenomenon with increase in supply voltage.

Generally, a maximum stroke of 6.5mm to 8mm was achieved with voltages from 3V to 9V, respectively, which was within the 3-4% stroke range rated by the manufacturer (Section 3.6).

5.2.2 Forced Cooling Tests

The next open loop test carried out was to observe the cooling rate and observe the effect of the forced air (fans) on cooling. This test involved heating the wires with 3V for 10

seconds and allowing the wires to cool under the ambient temperature, then heating again for 10 seconds but with the cooling assisted by the fans. This test was repeated for 5V, 7V and 9V. The temperatures and displacements were monitored, recorded and graphed. The cooling time was taken from the point where heating stopped to the point the temperature dropped below 28°C. The room temperature was 25°C. The time taken for the actuator to retract to its initial position from its maximum displacement was also recorded.

The graphs below show the temperature change with time (Figure 5.17), displacement change with time (Figure 5.18) and the displacement against temperature change (Figure 5.19) for 3V, under ambient cooling and forced air cooling.

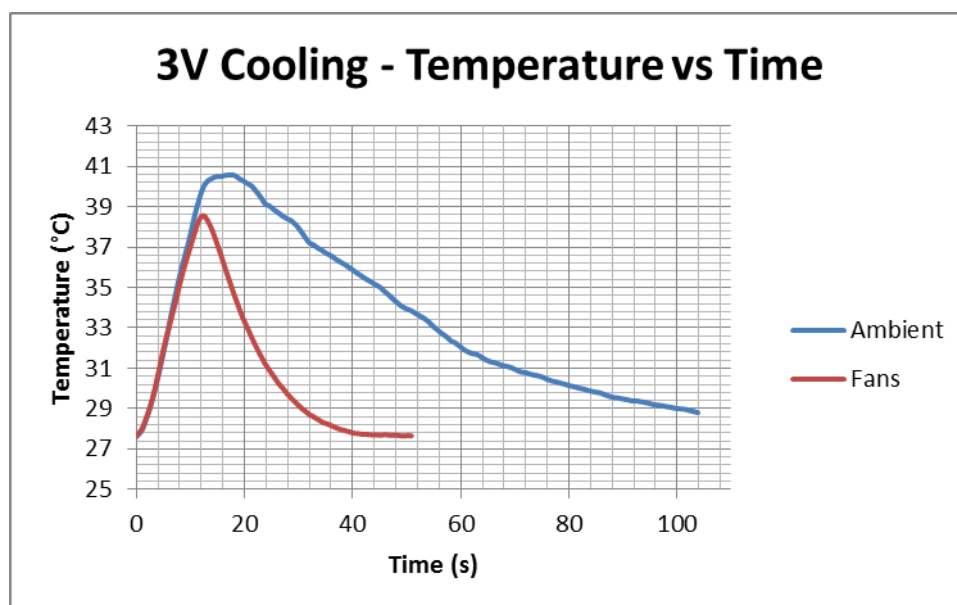


Figure 5.17: 3V cooling temperature with time

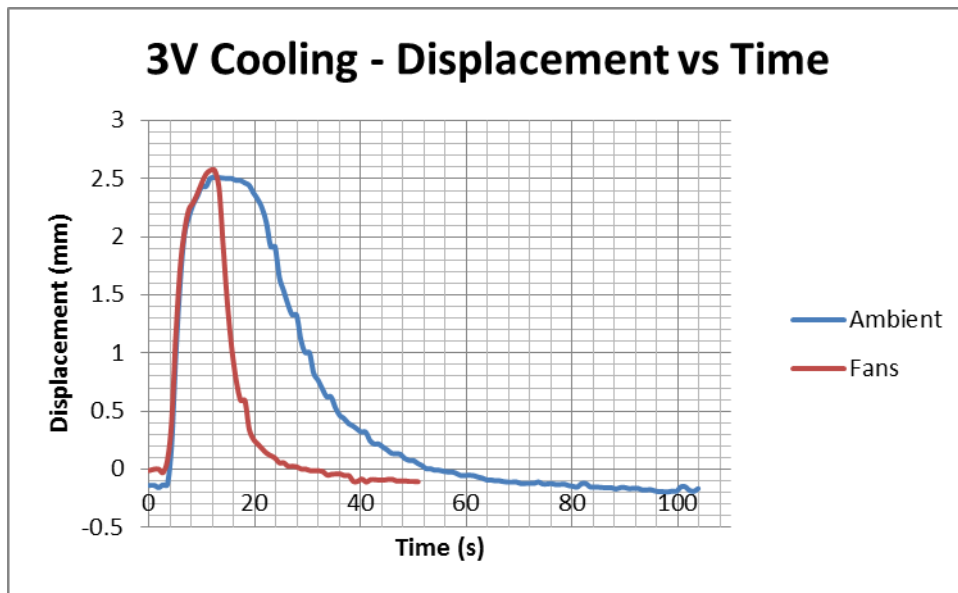


Figure 5.18: 3V cooling displacement with time

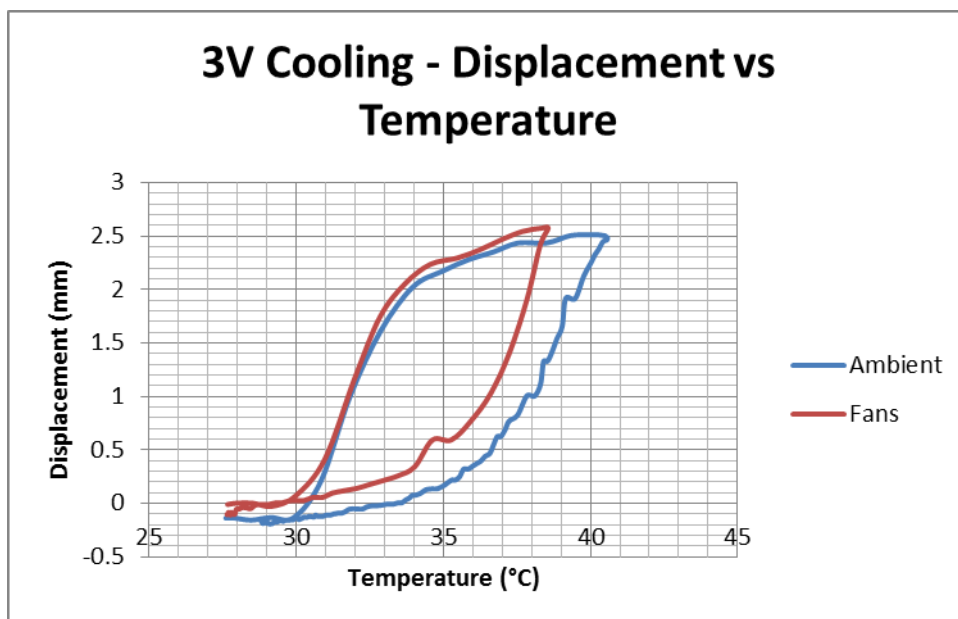


Figure 5.19: 3V cooling displacement with temperature

As expected, the use of fans improved the cooling speed. The temperature graph shows an improvement of 70s (70%), from 100s to 30s with fans. This directly corresponds with the displacement graph which shows the time to revert to initial position being shorter, improving by 24s (46%), from 52s to 28s. The temperature and displacement both show a rapid drop when cooled by fans compared to the smooth, steady decline when cooled under

the ambient temperature. The displacement plotted against temperature shows a wider hysteresis with the fans, as the displacement responds faster than the temperature.

The graphs below show the temperature change with time (Figure 5.20), displacement change with time (Figure 5.21) and the displacement against temperature change (Figure 5.22) for 5V, under ambient cooling and forced air cooling.

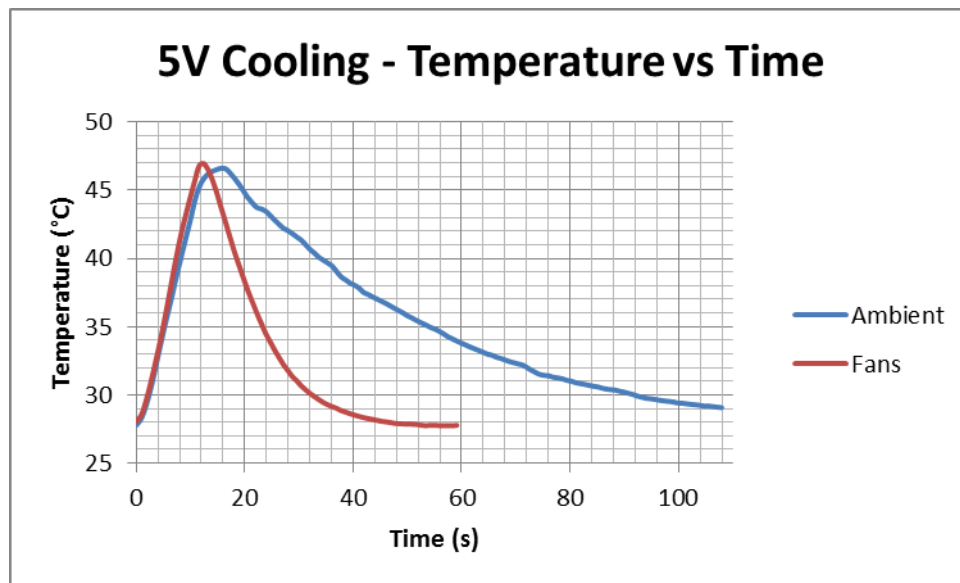


Figure 5.20: 5V cooling temperature with time

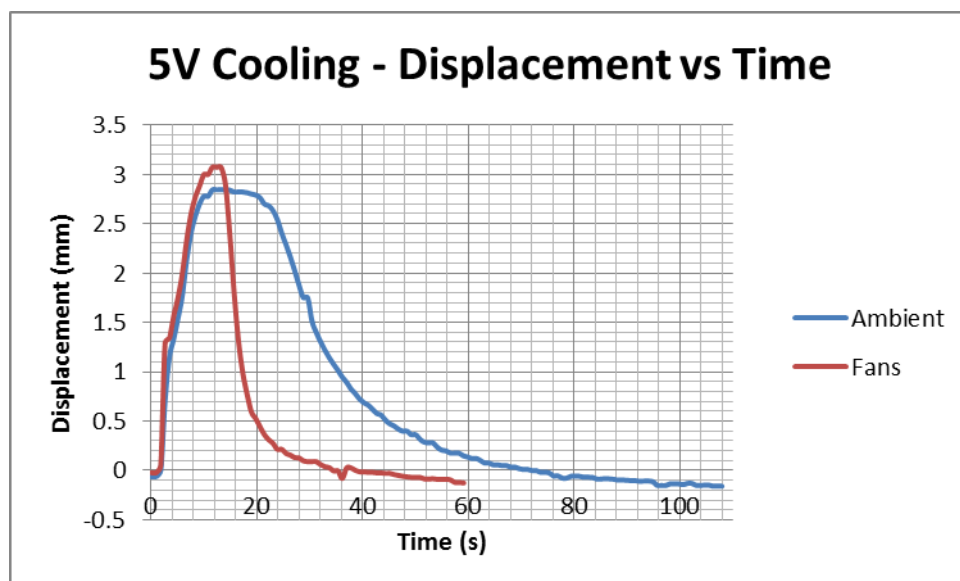


Figure 5.21: 5V cooling displacement with time

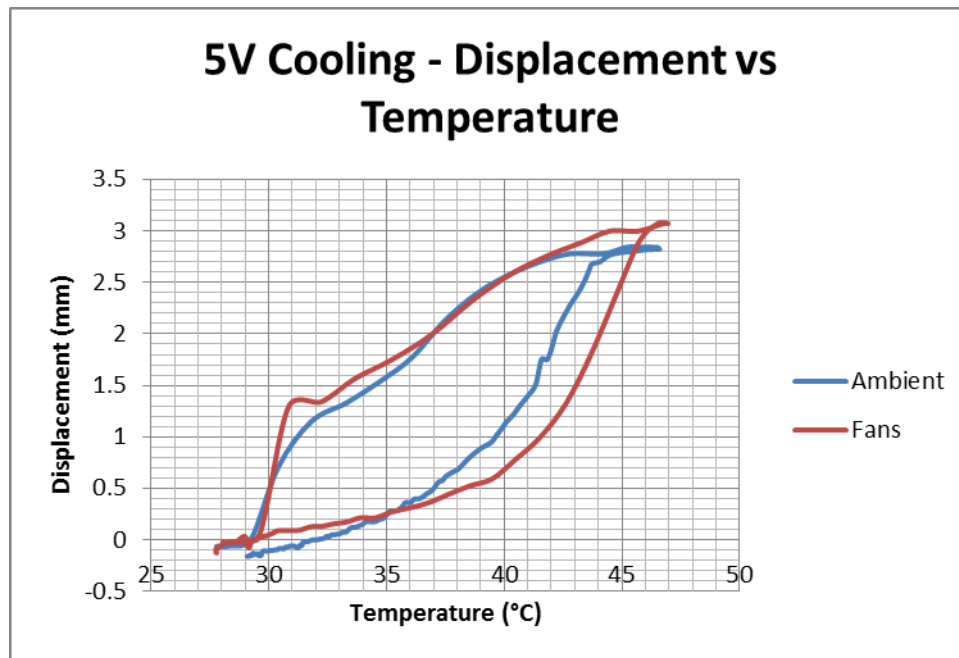


Figure 5.22: 5V cooling displacement with temperature

A similar trend to the 3V is seen when supplying the actuator with 5V. The temperature graph shows an improvement of 72s (67%), from 108s to 36s with fans. The displacement graph shows the time to revert to initial position, improving by 36s (53%), from 68s to 32s. The temperature and displacement both show a rapid drop when cooled by fans compared to the smooth, steady decline when cooled under the ambient temperature. The displacement plotted against temperature shows a wider hysteresis loop with the fans.

The graphs below show the temperature change with time (Figure 5.23), displacement change with time (Figure 5.24) and the displacement against temperature change (Figure 5.25) for 7V, under ambient cooling and forced air cooling.

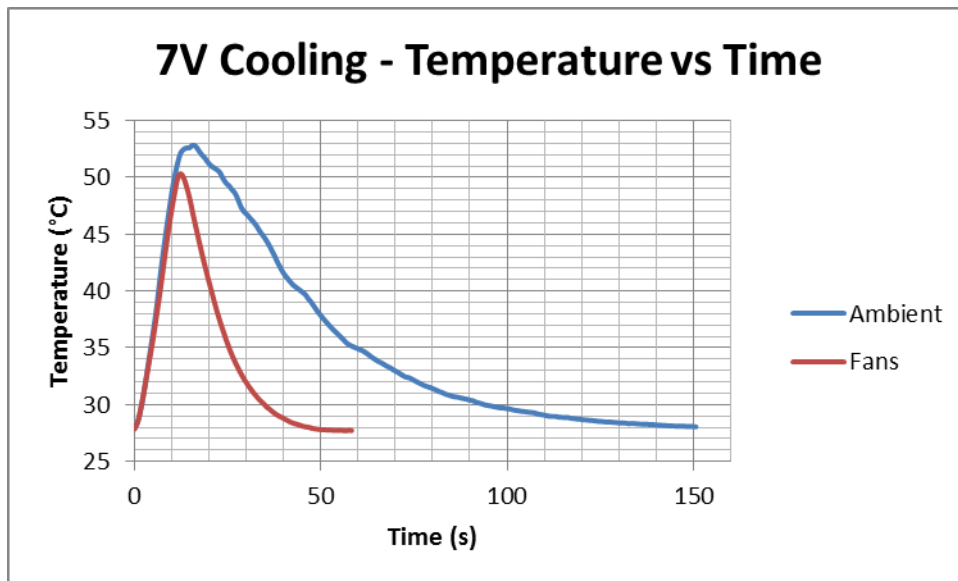


Figure 5.23: 7V cooling temperature with time

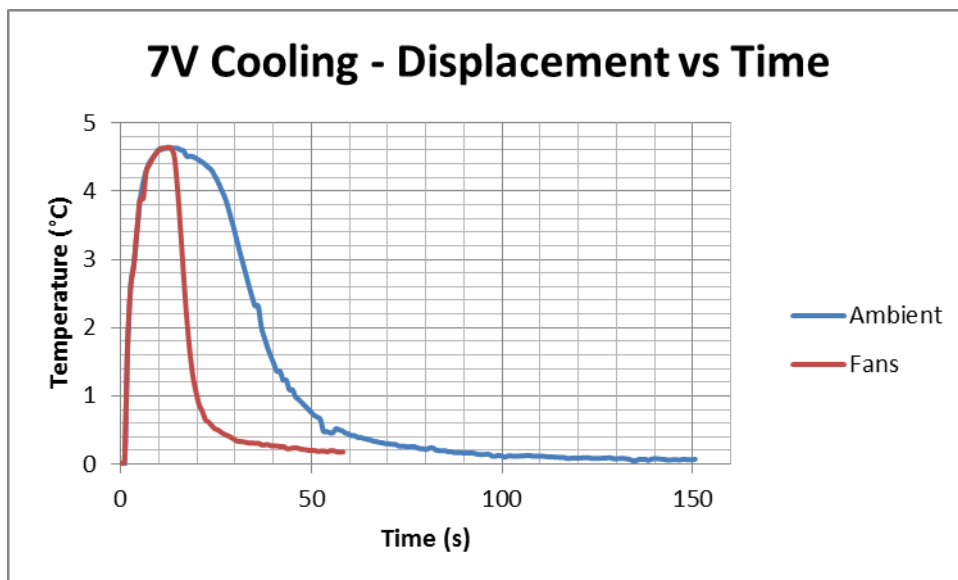


Figure 5.24: 7V cooling displacement with time

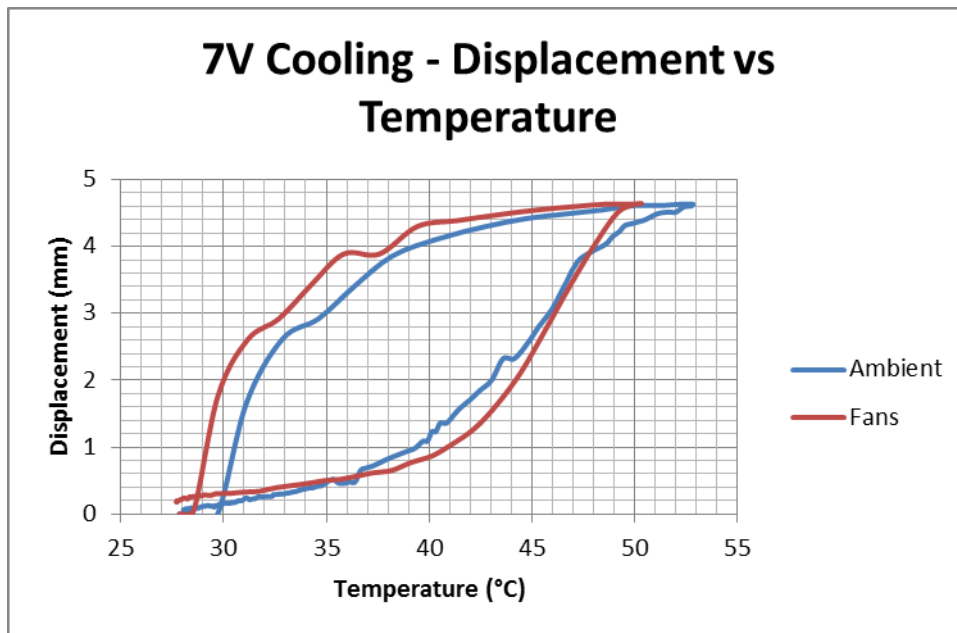


Figure 5.25: 7V cooling displacement with temperature

When supplying the actuator with 7V, the temperature graph shows an improvement of 72s (64%), from 112s to 40s with fans. The displacement graph shows the time to revert to initial position, improving by 40s (50%), from 80s to 40s. The temperature and displacement both show a rapid drop when cooled by fans compared to the smooth, steady decline when cooled under the ambient temperature. The displacement plotted against temperature shows a wider hysteresis loop with the fans.

The graphs below show the temperature change with time (Figure 5.26), displacement change with time (Figure 5.27) and the displacement against temperature change (Figure 5.28) for 9V, under ambient cooling and forced air cooling.

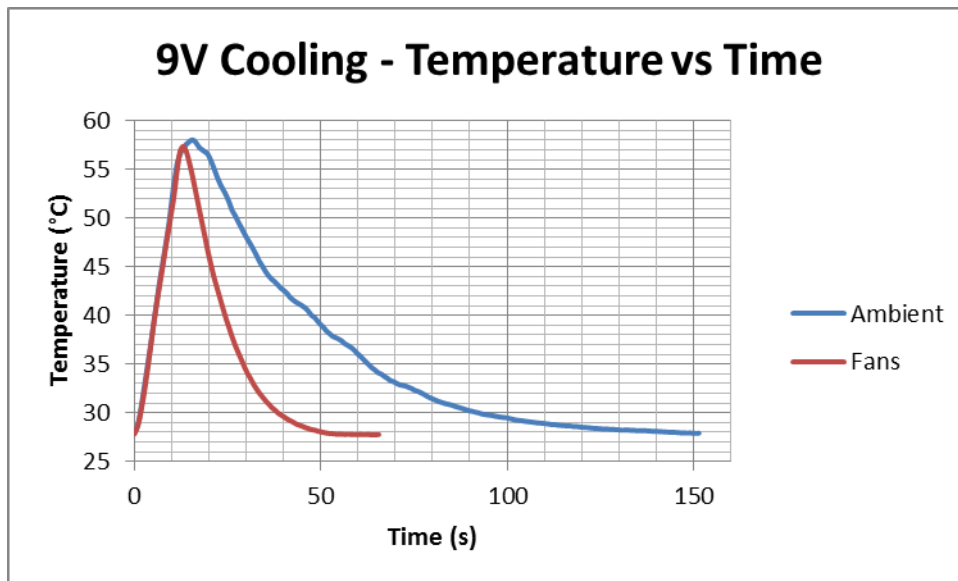


Figure 5.26: 9V cooling temperature with time

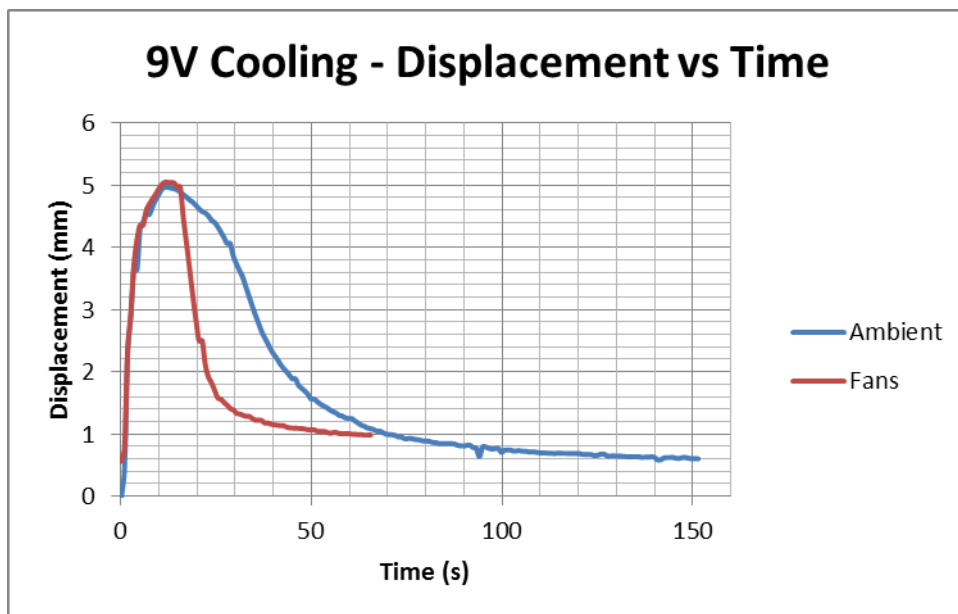


Figure 5.27: 9V cooling displacement with time

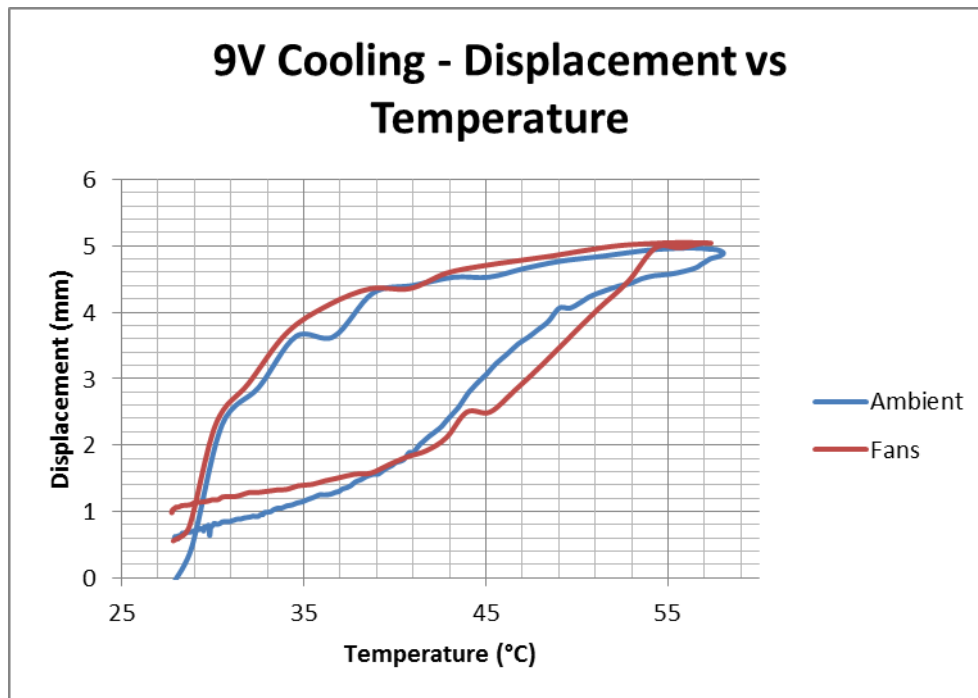


Figure 5.28: 9V cooling displacement with temperature

When supplying the actuator with 9V, the temperature graph shows an improvement of 70s (64%), from 110s to 40s with fans. The displacement graph shows the time to revert to initial position, improving by 60s (55%), from 110s to 50s. The temperature and displacement both show a rapid drop when cooled by fans compared to the smooth, steady decline when cooled under the ambient temperature. The displacement plotted against temperature shows an almost identical hysteresis loop as the temperature time improvement and the displacement time improvement were fairly equal.

The temperature, displacement and displacement against temperature graphs for the four different voltages under forced air cooling were combined for comparison as shown in Figure 5.29, Figure 5.30 and Figure 5.31.

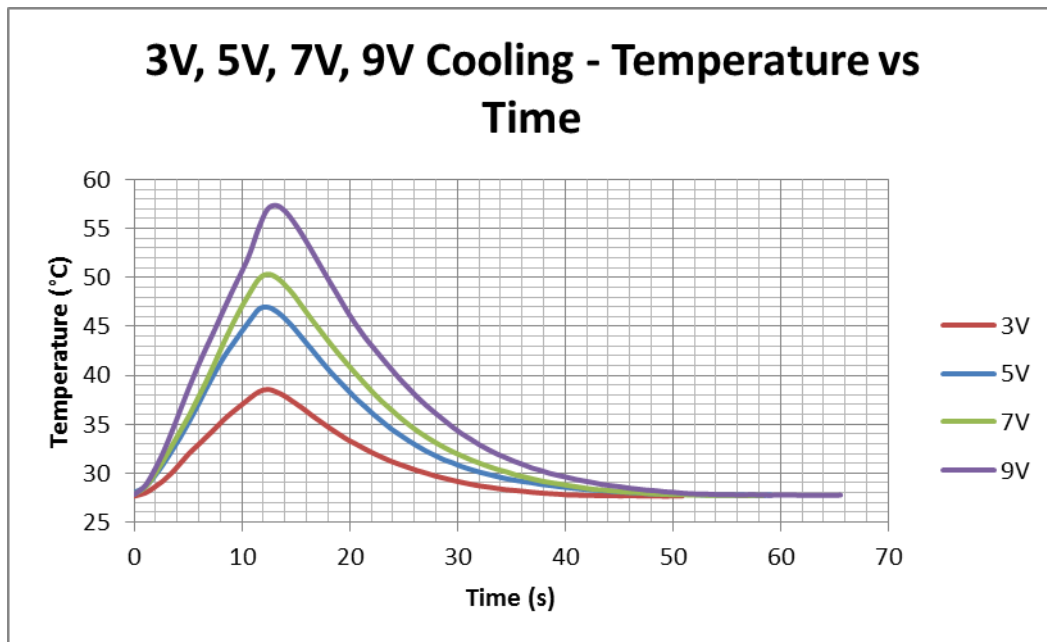


Figure 5.29: 3V, 5V, 7V, 9V cooling temperature with time

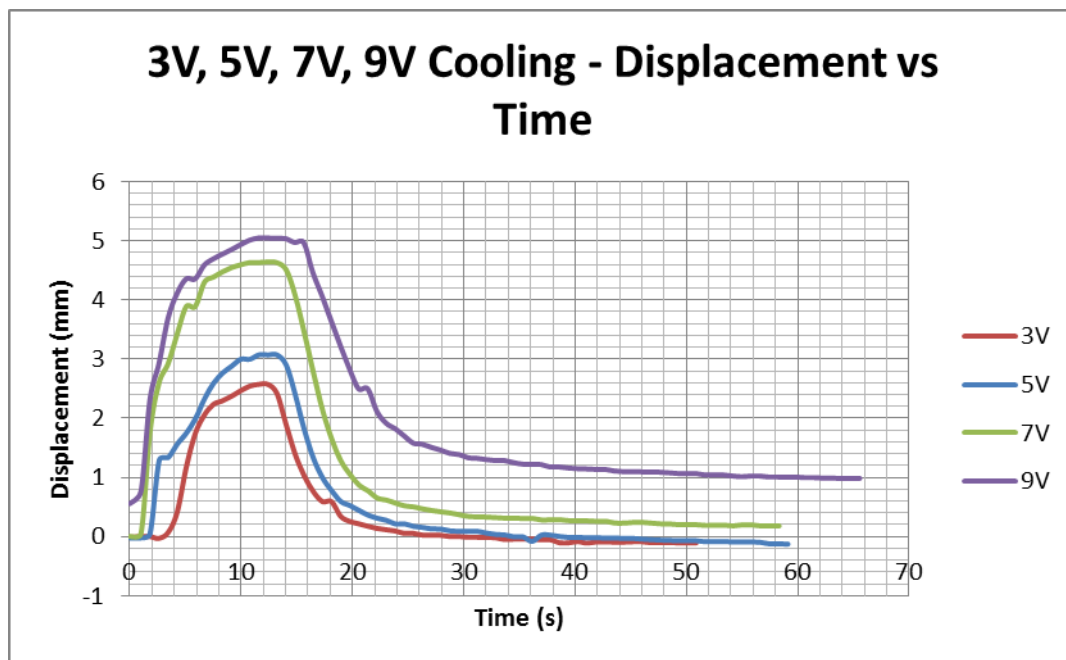


Figure 5.30: 3V, 5V, 7V, 9V cooling displacement with time

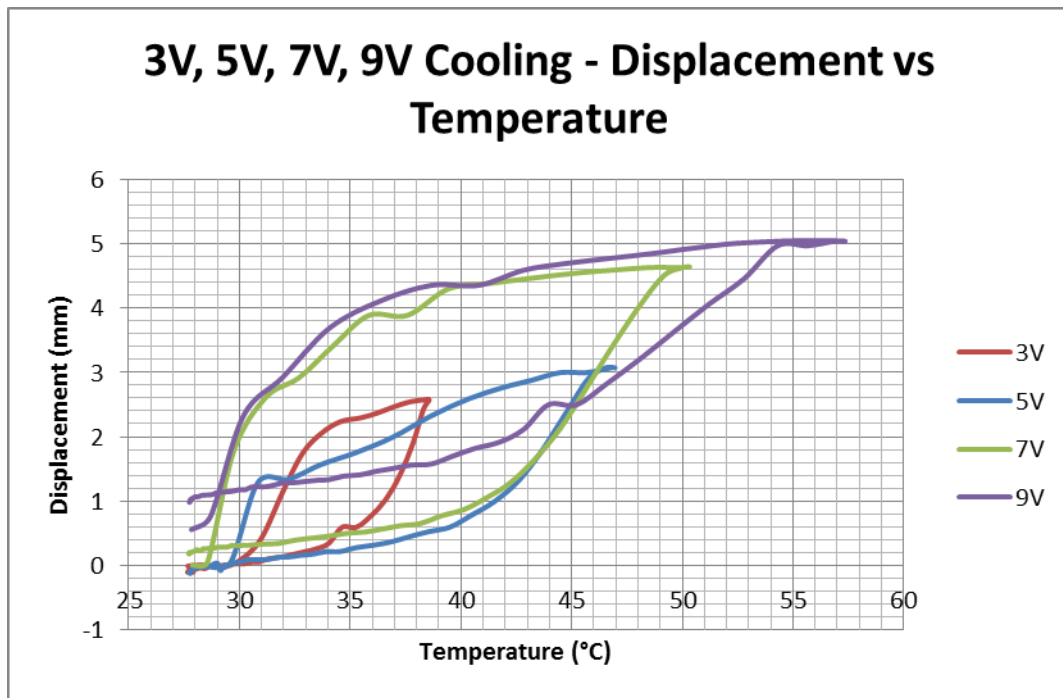


Figure 5.31: 3V, 5V, 7V, 9V cooling displacement with temperature

The graphs show the cooling time from the maximum temperature and retraction from the maximum displacement being higher with the increase in voltage. The temperature curves show a steeper decline slope with the higher voltages as higher maximum temperatures were achieved and thus greater heat loss was experienced. The displacement curves showed a similar trend. The hysteresis curves grow larger with increase in voltage, as the temperatures and displacements attained increased with higher voltage.

As expected, the fans increase the cooling rate and the actuator shaft retracted much faster, ready for the next actuation, improving cycle time. The cooling times were greater than the retraction times, due to the fact that while retracting, the martensite finish temperature is higher than the room temperature. Thus, the actuator fully retracted before the wires had cooled to room temperature. The retraction time generally showed an improvement of approximately 50%. Results obtained by Gedouin et al. [30] showed an improved retraction time of 60% with forced air. The cooling time generally showed an improvement of

approximately 65%. This result showed close correlation with Table 2.3 that shows a maximum improvement with cooling under forced air of 75%. The difference can be attributed to the room temperature. A higher room temperature would mean the rate of heat loss would be reduced. The number of wires in the bundle could also create a difference in cooling time, as more wires would result in a slower rate of cooling.

5.2.3 Radial Force Tests

The actuator placed in a vertically as shown in Figure 4.5 with masses placed on the shaft to provide a radial opposing force and supplied with a constant 3V. The 6 wire bundle provided a force of approximately 120N and the bias force 50N, giving the actuator a net force of 70N. When positioned vertically, this net force became 50N as the moveable block weighed 20N and opposed the wire motion.

A free test was first performed. The test was repeated with a 1kg (10N), 3kg (30N) and the maximum 5kg (50N) mass. The temperatures and displacements for the four tests were recorded and graphed (Figure 5.32, Figure 5.33 and Figure 5.34).

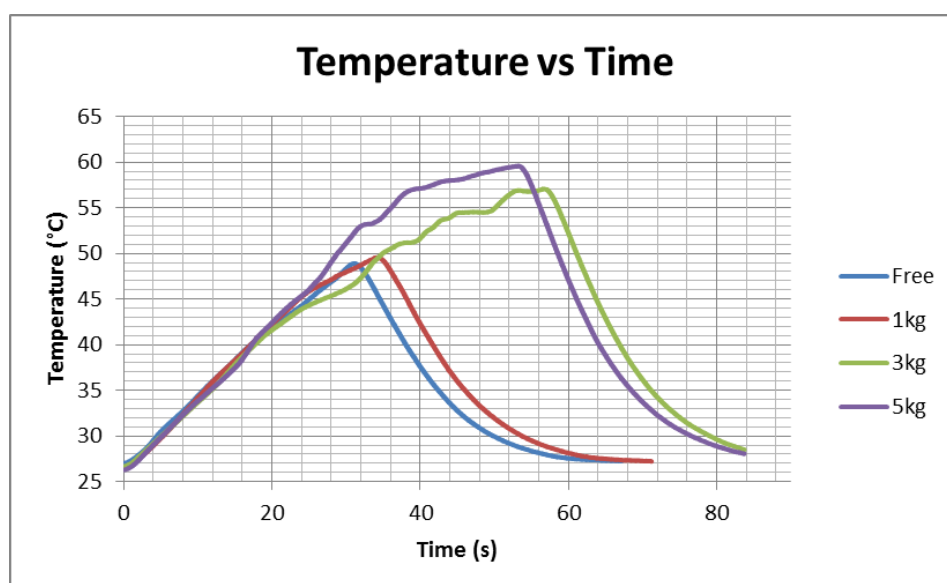


Figure 5.32: Temperature with time for radial forces

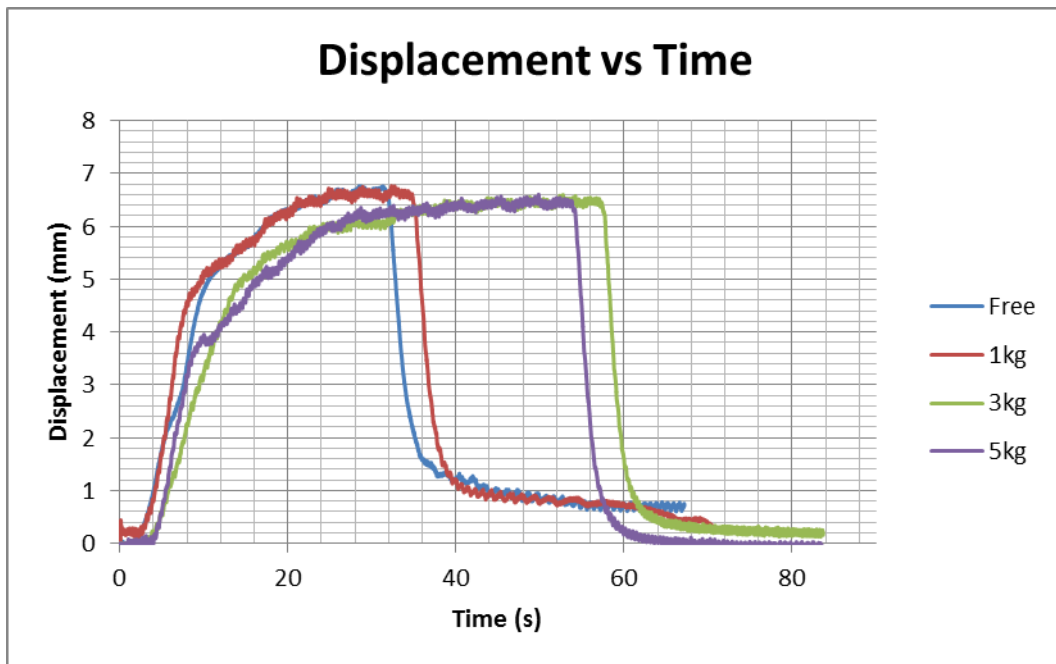


Figure 5.33: Displacement with time for radial forces

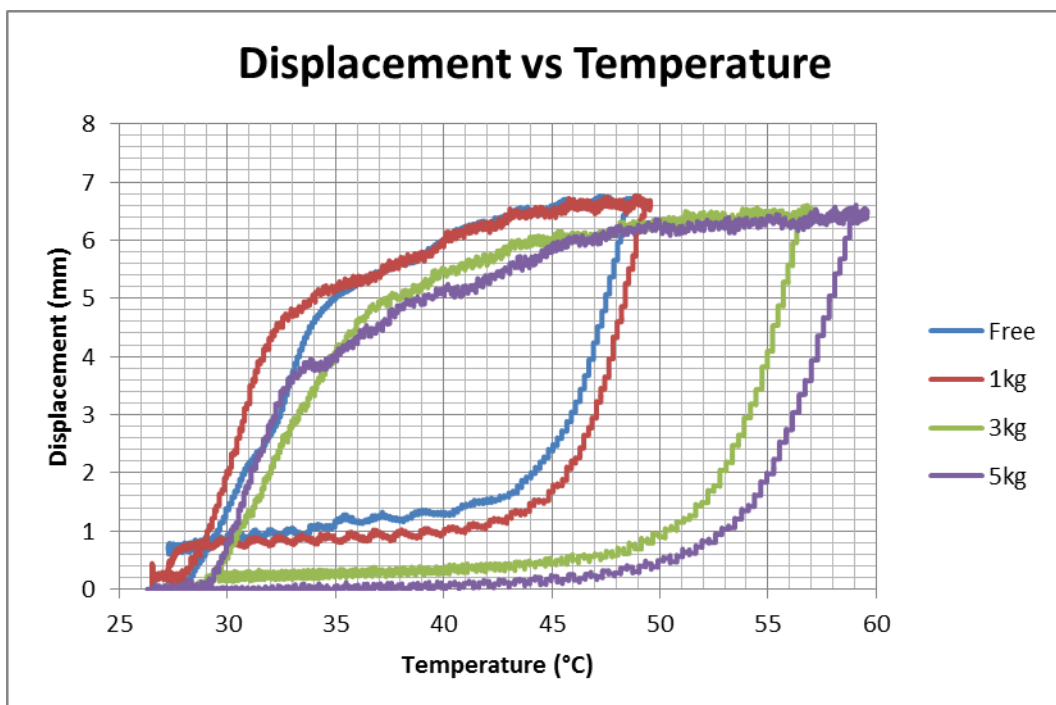


Figure 5.34: Displacement with temperature for radial forces

As the radial force acting on the shaft was increased the rise in temperature becomes steeper and the maximum temperature becomes higher. More heating is required for the actuator to reach maximum displacement. The maximum displacement of 6.5mm is

achieved irrespective of the force. Although, it took a slightly longer time for the actuator to reach maximum stroke with increase in force, with 1kg taking 24s and 5kg taking 40s, the maximum stroke remained unaffected by force. Anadon [7] obtained similar results with increase in force. The displacement curves appear shifted to the right with increase in force. The higher forces increase the bias force causing the actuator to retract faster creating steeper displacement curves during cooling. The temperature curves during cooling remain unaffected and have similar slopes. The temperature and displacement characteristics create hysteresis loops that appear shifted to the right and wider with increase in force. The hysteresis loops appear to have higher critical phase temperatures and greater loss in displacement during cooling with increase in force. This trend shows consistency with Figure 2.13 where the critical phase temperatures increase with increased stress. These results can thus be applied to determine γ and β for modelling in Equation 2.15 and Equation 2.18. The ability of the actuator wires to achieve maximum stroke under a radial force of 50N (5kg mass) while supporting the 20N moveable block proved that the 70N maximum radial force requirement is achieved.

5.3 Closed Loop Experiments

5.3.1 Controlled Position Tests

The closed loop tests involved applying PID control to maintain a user selected displacement setpoint with displacement feedback. The actuator was supplied with 3V and its performance in maintaining 1mm, 2mm, 3mm, 4mm and 5mm for approximately 10 seconds was recorded and graphed. The fans were used to assist cooling after actuation. This test was repeated for 5V, 7V and 9V. Before performing the closed loop tests, a tuning run was done to determine the PID gains. The PID controller was automatically tuned using

the Autotune Wizard and the gains were output as proportional 1.275, integral 0.011 and derivative 0.

The following graph (Figure 5.35) was plotted from the actuator's response to various setpoints when supplied with 3V.

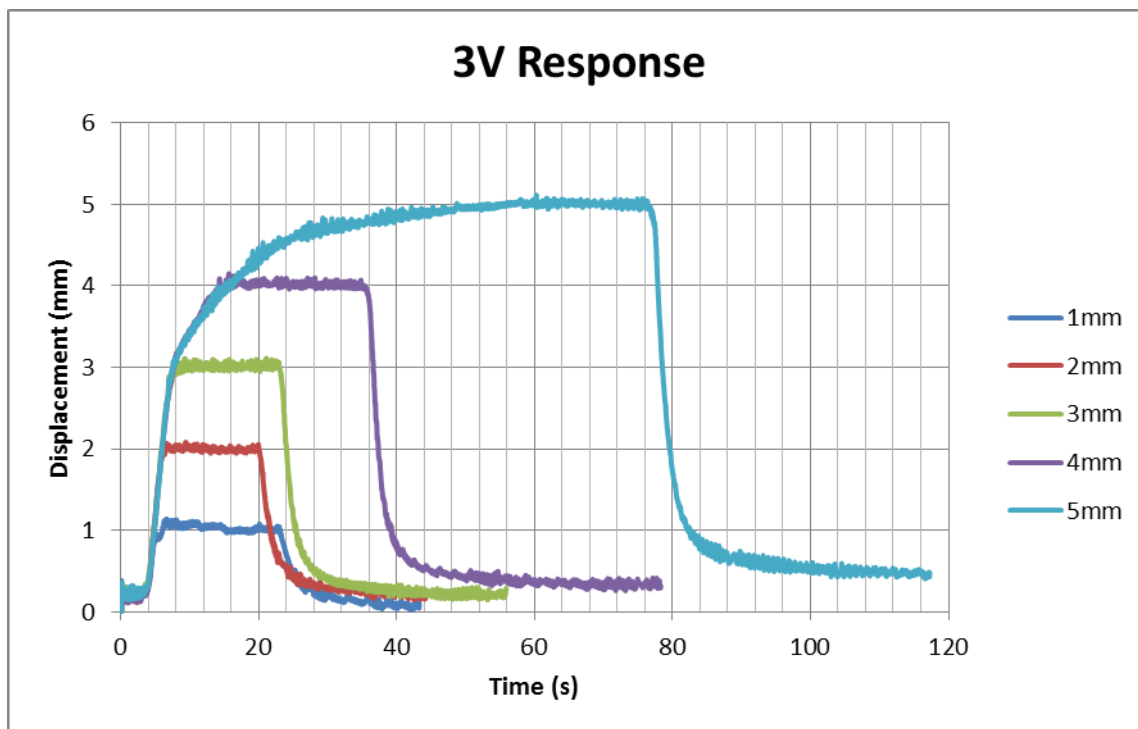


Figure 5.35: 3V displacement response with time

When supplied with 3V, the rise time increased with increase in displacement. From 6 seconds for 1mm to 40 seconds for 5mm. This was expected as higher temperatures are required to achieve higher displacements, thus more heating time. The chance of overshoot also decreased and the actuator showed a more gradual increase in displacement in attaining the setpoint as the setpoint displacement was increased.

The following graph (Figure 5.36) was plotted from the actuator's response to various setpoints when supplied with 5V.

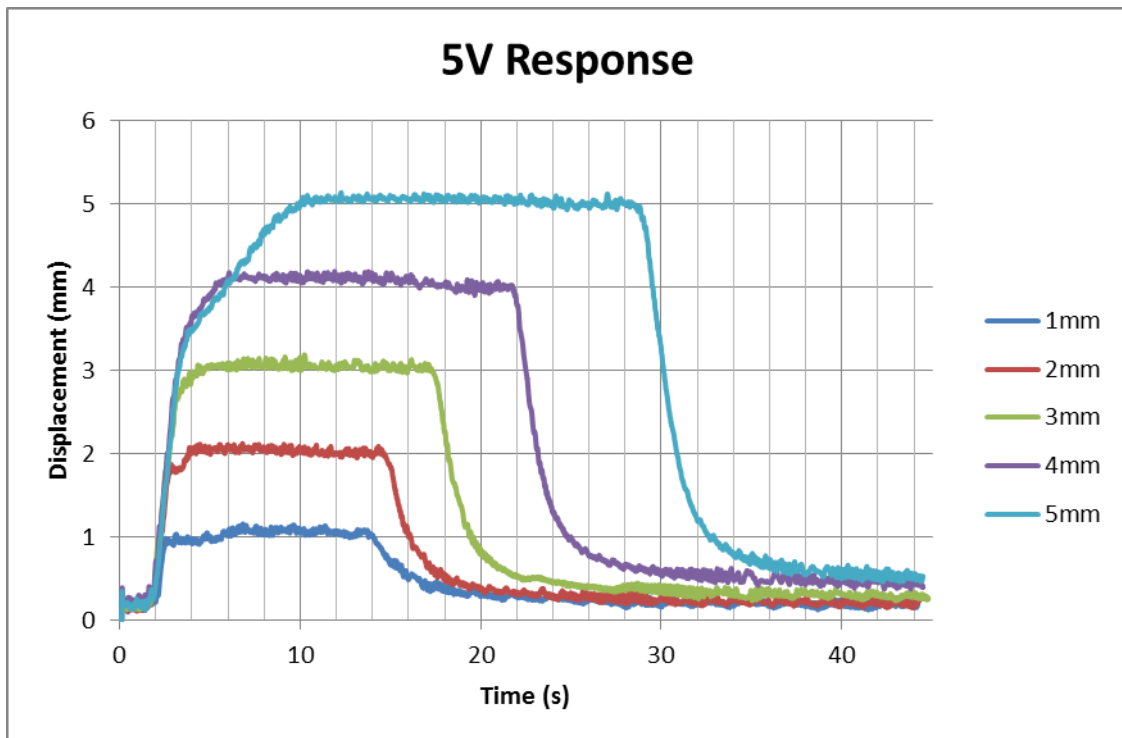


Figure 5.36: 5V displacement response with time

The actuator showed a similar trend when supplied with 5V. The rise time increased with increase in displacement. From 3 seconds for 1mm to 9 seconds for 5mm. The actuator showed a more gradual increase to the setpoint as the setpoint displacement was increased.

The following graph (Figure 5.37) was plotted from the actuator's response to various setpoints when supplied with 7V.

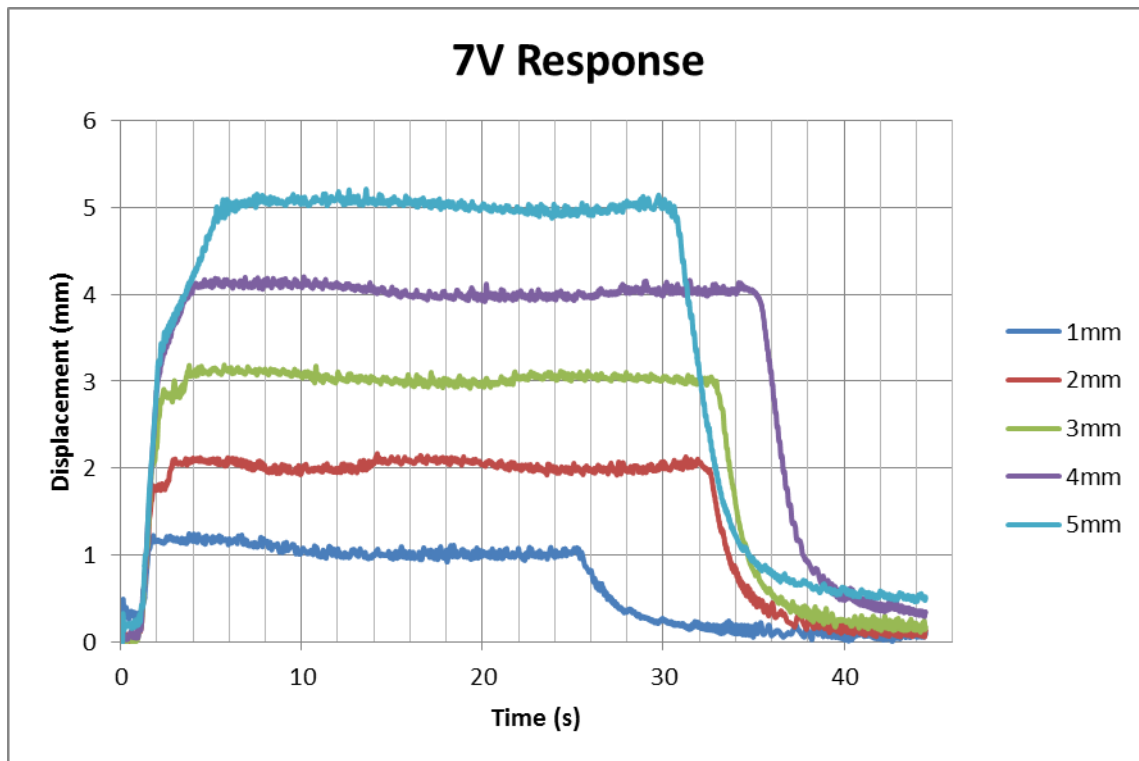


Figure 5.37: 7V displacement response with time

When supplied with 7V, the actuator performed in a similar manner. The rise time increased with increase in displacement. From 1.5 seconds for 1mm to 5 seconds for 5mm. The increase to attain the setpoint was more gradual with increase in setpoint displacement.

The following graph (Figure 5.38) was plotted from the actuator's response to various setpoints when supplied with 9V.

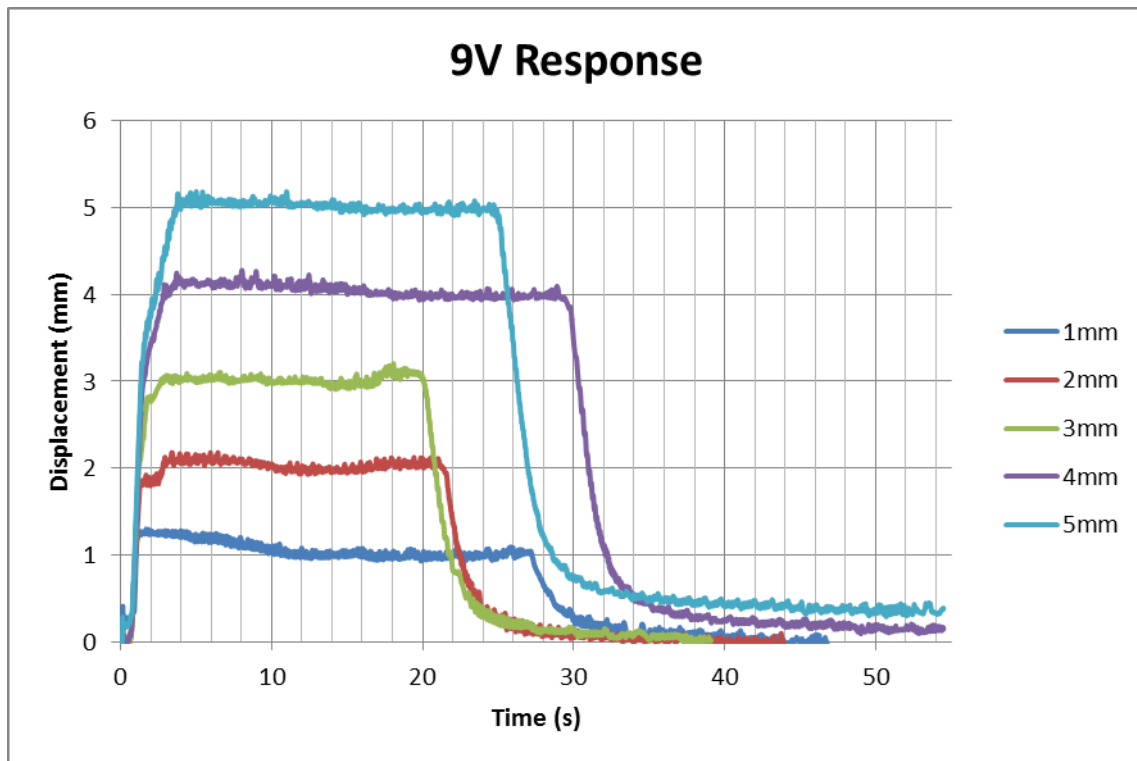


Figure 5.38: 9V displacement response with time

When supplied with 9V, the actuator maintained the previous trend. The rise time increased with increase in displacement. From 1 second for 1mm to 3 seconds for 5mm. The increase to attain the setpoint was more gradual with increase in setpoint displacement.

The data from each of the five setpoints with varying voltage were plotted (Figure 5.39-5.43). The time axis on the graphs was fixed from 0 to 100 seconds for comparison.

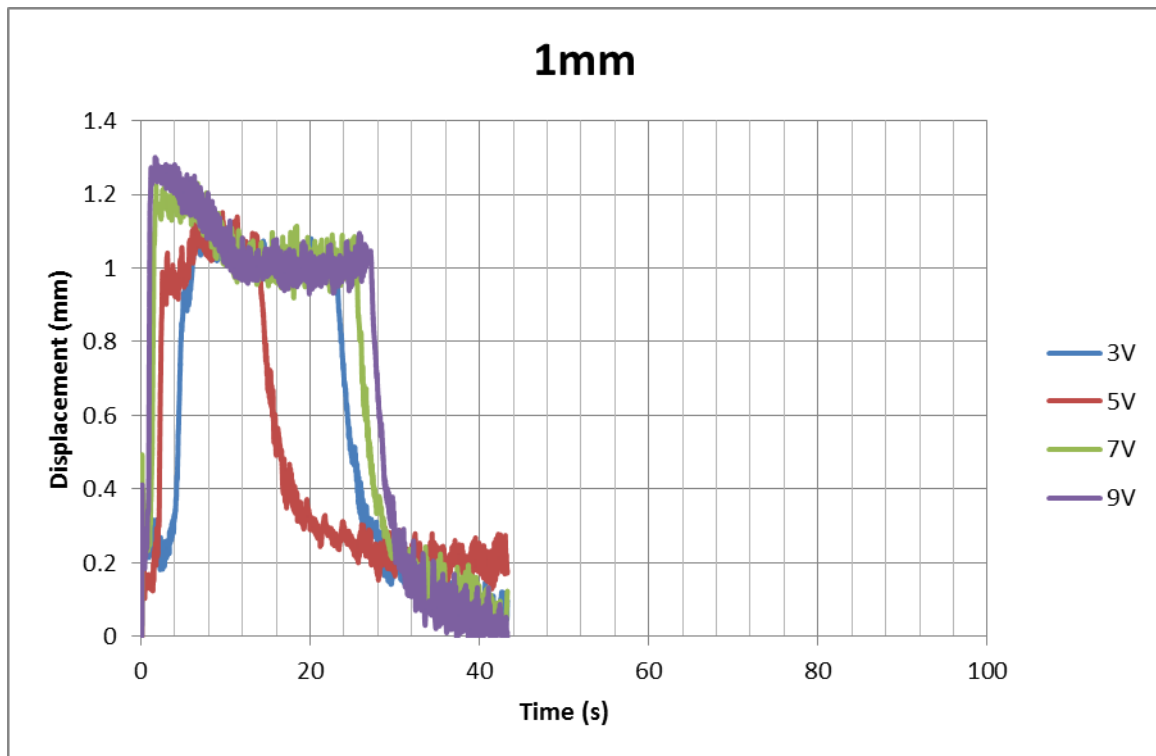


Figure 5.39: 1mm 3V, 5V, 7V, 9V displacement with time

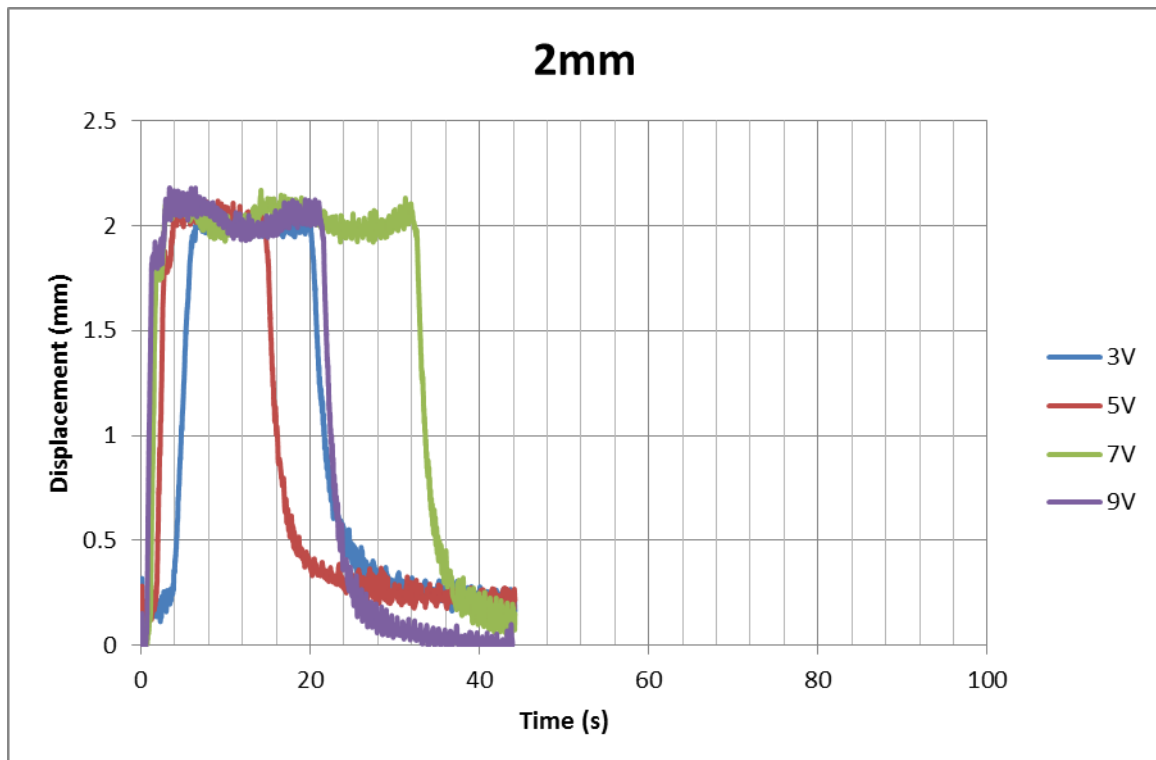


Figure 5.40: 2mm 3V, 5V, 7V, 9V displacement with time

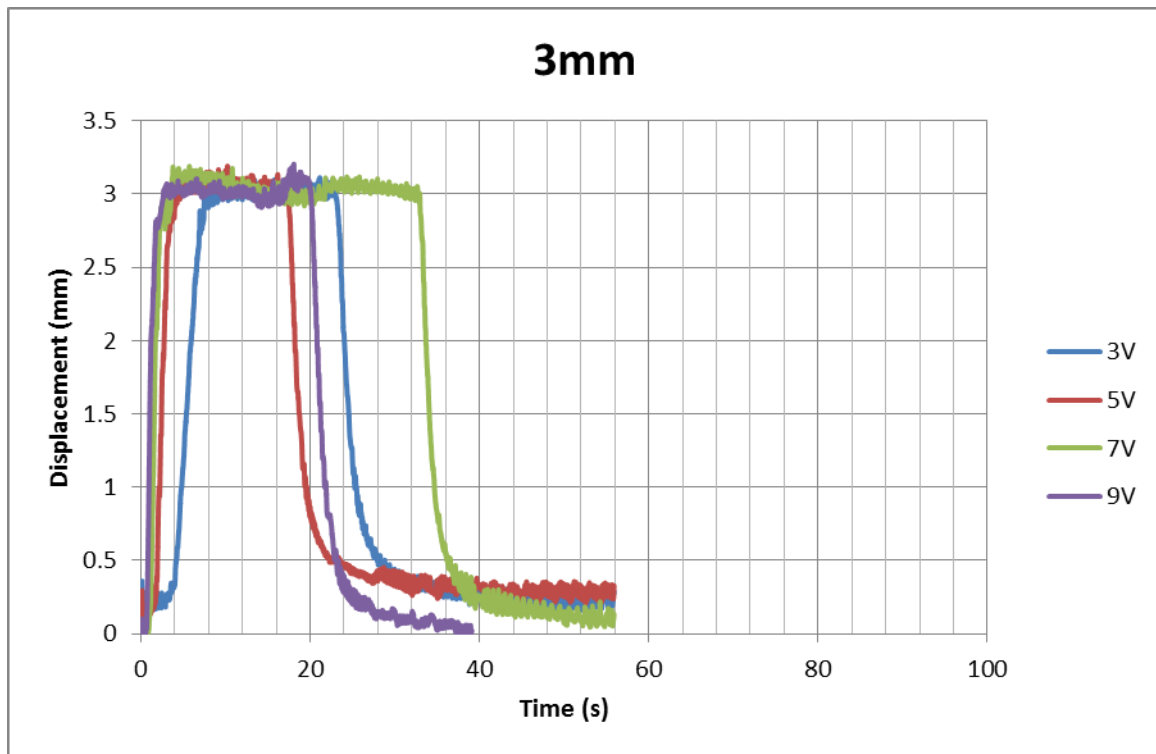


Figure 5.41: 3mm 3V, 5V, 7V, 9V displacement with time

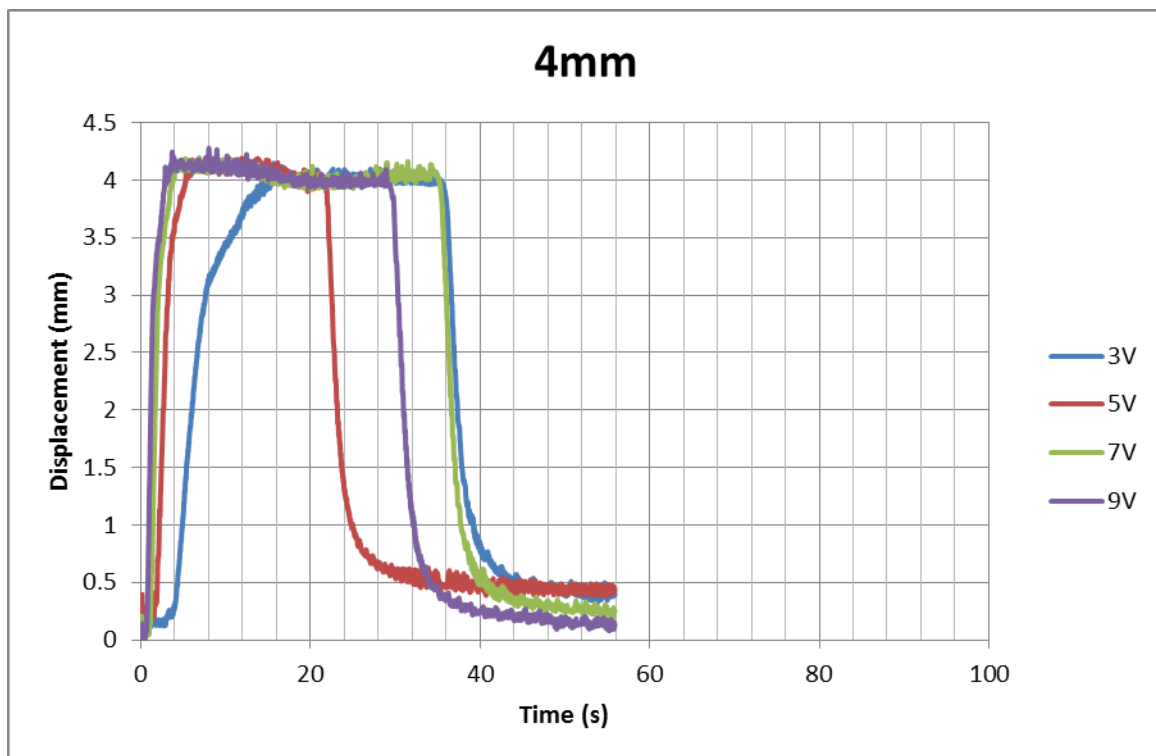


Figure 5.42: 4mm 3V, 5V, 7V, 9V displacement with time

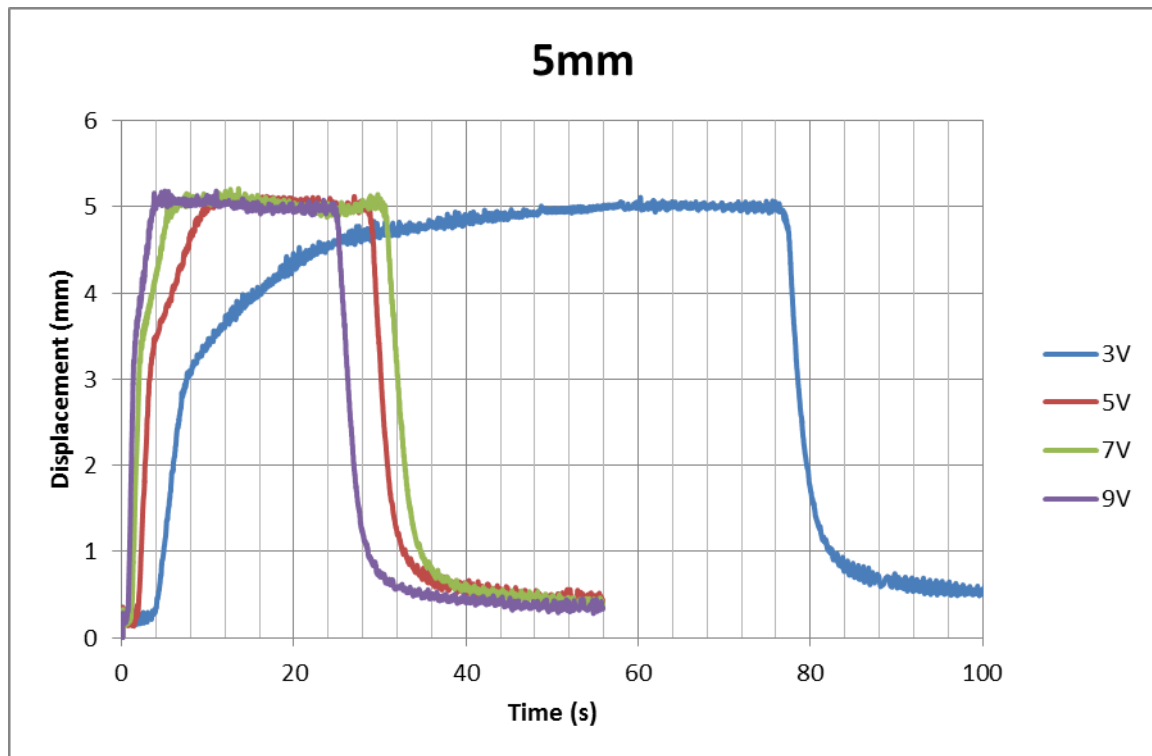


Figure 5.43: 5mm 3V, 5V, 7V, 9V displacement with time

The results show shorter rise times with higher voltages. The difference between the rise times of the 1mm setpoint and the 5mm setpoint are much smaller for the higher voltages. The higher voltages have a higher chance of producing large overshoots with smaller setpoint displacements. These results are due to the fact that higher voltages supply more current, thus the wires are heated faster, resulting in a faster response time. The quick rise in temperature leads to faster stroke time, increasing the probability of overshoot. The graphs show the actuator produced a more stable response when higher voltages are applied for higher displacement setpoints and lower voltages for lower displacement setpoints.

5.3.2 Steady-State Position Errors

The mean displacement errors (in millimetres) during the maintenance of the setpoints for the four different voltages were recorded as shown in Table 6.1. The error is the process

variable subtracted from the setpoint [51]. The mean of the absolute error in maintaining the setpoint was calculated to determine the accuracy of the actuator. The steady-state data was selected from the point the actuator achieved the desired displacement to the point just prior to cooling.

Table 5.1: Steady-state errors (mm) in displacement setpoints for different voltages

	1mm	2mm	3mm	4mm	5mm	Mean
3V	0.0398	0.0187	0.0264	0.0276	0.0164	0.0258
5V	0.0606	0.0432	0.0547	0.0871	0.0513	0.0594
7V	0.0711	0.0472	0.0554	0.0612	0.0540	0.0578
9V	0.0860	0.0515	0.0311	0.0657	0.0416	0.0552

Table 5.1 represented the actuator's mean actual displacement from the desired displacement, thus giving a measure of the accuracy. The table shows 3V having the least error over all the displacements, although, the slow rise times for the higher displacements make 3V unsuitable. The table generally provides a similar conclusion as the graphs in Figures 5.39-5.43, that the actuator produces a more accurate response when higher voltages are applied for higher displacement setpoints and lower voltages for lower displacement setpoints.

The PID control to maintain the required displacement is effective when the system is linear. This control is only applied during heating. Figures 6.15 and 6.16 show the actuator's displacement response to the various voltages used. It was observed that the curves were approximately linear for the various voltages between 2mm and 5mm. This also explains why the actuator produces are more accurate response for all the setpoint displacements

except 1mm, which lies within the non-linear region. Figure 5.39 shows the 1mm response having large overshoots and fluctuations as the controller experienced difficulties in maintaining this setpoint.

5.4 Recommended Operating Parameters

Based on the findings from the conducted open loop and closed tests, the best operating parameters for the system must be determined. From the open loop tests, it was observed that a saturation effect occurs with increase in voltage reducing the efficiency of the system. A large overshoot is unacceptable for this type of actuator system considering it is to be implemented in a machining application. From the closed loop tests, the higher voltages had larger errors and overshoots with small displacements. Thus, 5V was selected as the optimum operating voltage. To minimise overshoot the proportional gain must be decreased and to minimise setpoint error the integral gain must be increased [51]. Thus, to create a more stable system with minimal overshoot and error, the controller constants were adjusted to proportional gain 0.9, integral time 0.03 and derivative time 0.

The recommended settings were tested by varying the displacement setpoints and observing the actuator responses. The displacement setpoint was varied in steps of 1mm between 1mm and 3mm and held at each point for 20s. The result is shown in Figure 5.44.

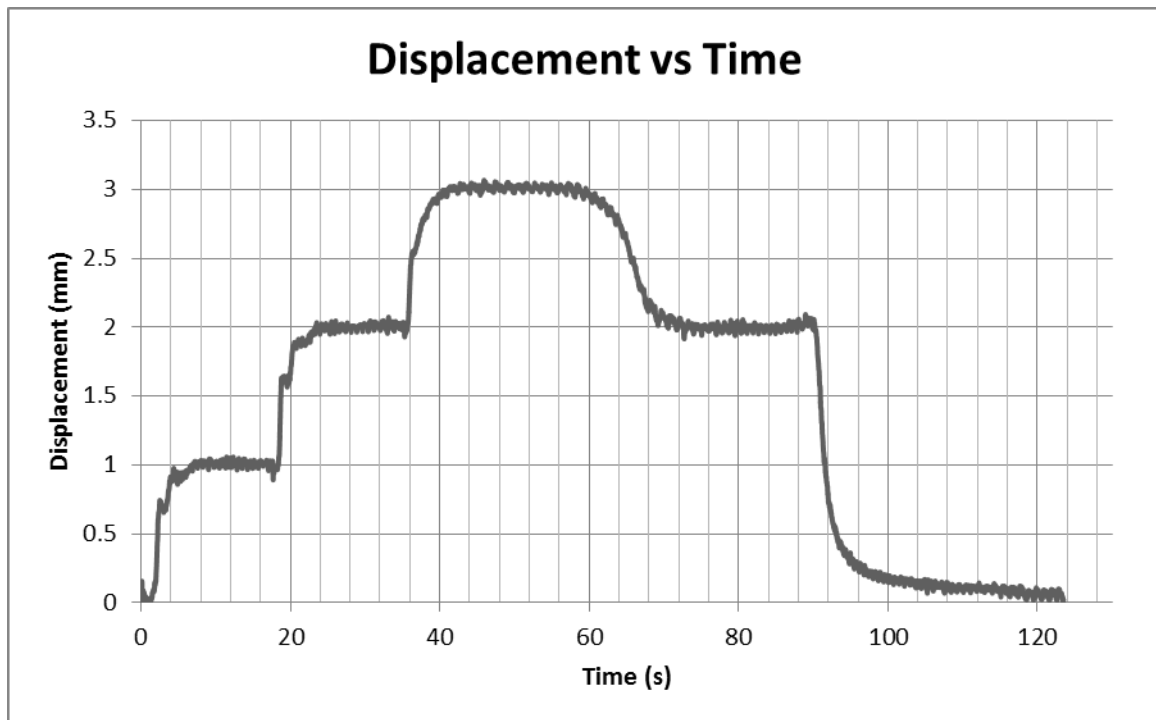


Figure 5.44: Varying displacement response with time for recommended settings

The plotted graph shows a stable system with no overshoot for various displacement setpoints. The actuator took approximately 4s each 1mm step, a rate of 0.25 mm/s. The mean errors in maintaining the various setpoints were calculated and shown in Table 5.2, which compared the system’s accuracy before and after optimisation.

Table 5.2: Steady-state errors (mm) with recommended settings

	1mm	2mm	3mm	Mean
5V	0.0606	0.0432	0.0547	0.0528
Optimised 5V	0.0148	0.0144	0.0167	0.0153

As seen in Table 5.2, the resulting errors for each of the setpoints with the optimised system were improved. The system accuracy had improved by 0.0375mm from a mean error of 0.0528mm to 0.0153mm. This result was within the acceptable accuracy of 0.013mm for turning operations mentioned in Section 2.8. Such high accuracies are difficult to obtain

using SMA actuators, for example, Ahn and Nyugen [36] generally obtained a steady-state error of 0.1mm from their results using a PID controller.

The errors associated with the various setpoints were approximately equal showing that the system had consistent repeatability. The errors could be attributed to the wires not being in equal tension. As seen in the results from Section 5.2.3, wires under varying stress exhibit different displacement characteristics. This could be improved by using vented screws to fix the actuator wires into the blocks so that the tension can be easily adjusted in individual wires.

Chapter 6. Conclusions

The research objective was successfully achieved and a shape memory alloy actuator was designed and fabricated. The radial force the SMA actuator wires was designed to oppose was selected based on the machining conditions in the turning process of aluminium finish cuts with a single point tool. Commercially available SMA wire form was selected to provide force and movement for the actuator. The actuator was designed to withstand a total cutting force of approximately 300N, of which 70N was the radial force that the SMA wire had to overcome. Dynalloy Flexinol actuator wire were bundled and fixed onto the actuator to produce a total force of 120N. A bias force of 50N was provided by a gas spring that retracted the actuator, thus the actuator produced a net force of 75N. The actuator was fitted with a current sensor, thermocouple, and linear potentiometer to provide feedback on the response. The data was collected and monitored in a PC running Labview software via DAQ modules. The control system was implemented within Labview with a PID controller outputting the duty cycle for a PWM signal which was the input of a MOSFET switching circuit varying the power supply to the SMA wire bundle. The cooling of the wires was assisted with fans which automatically switched on when the power supply was cut off.

Open loop tests were conducted to determine the maximum stroke, the effect of cooling and response to radial forces. These tests revealed the expected non-linearity of the SMA. For the maximum stroke tests, power was supplied to the actuator until the stroke became fairly constant then allowed to cool naturally. When supplied with voltages between 3V and 9V the actuator achieved the rated maximum stroke of 3-4%. A saturation phenomenon seemed to occur with higher voltages, with an increase in voltage showing a small change in

maximum displacement with the higher voltages. A sharper increase in temperature also occurred with increasing voltage. This showed a loss in efficiency at higher voltages.

The forced cooling test involved heating the wires for 10 seconds and allowing the wires to cool under the ambient temperature, then heating again for 10 seconds but with the cooling assisted by the fans. As expected, the results showed an increased cooling rate as a result of using the fans and the actuator shaft retracted much faster. The cooling time generally showed an improvement of approximately 65% with fans.

The radial force tests involved positioning the actuator vertically with masses placed on the shaft to provide the opposing force. The results showed more heating is required for the actuator to reach maximum displacement. It took a longer time for the actuator to reach maximum stroke with increase in force, but the value of the maximum stroke remained unaffected by force. The actuator wires were also capable of achieving maximum stroke under the maximum required radial force of 70N.

The closed loop tests involved applying PID control to maintain a user selected displacement setpoint with displacement feedback. After autotuning, the PID controller gains were set as proportional 1, integral 0.01 and derivative 0. The actuator was supplied with various voltages to maintain setpoints from 1mm to 5mm for approximately 10 seconds. The mean displacement errors in maintaining the setpoints for the various voltages were also calculated. The actuator generally produced a more accurate and stable response when higher voltages are applied for higher displacement setpoints and lower voltages for lower displacement setpoints.

Finally, the best operating parameters for the system was recommended. 5V was selected as the optimum voltage based on the loss in efficiency and larger overshoots with higher voltages. To minimise overshoot the proportional gain must be decreased and to minimise setpoint error the integral gain must be increased. The controller constants were adjusted to a proportional gain 0.9, integral time 0.03 and derivative time 0 to produce a more stable and accurate response. The resulting response showed a more stable system with no overshoot for various displacement setpoints. The actuator had a feed rate of 0.25 mm/s and an improved accuracy of 0.0153mm, which was within the acceptable accuracy for turning operations. The recommended system was deemed accurate for a conventional lathe machine cross feed. The system also showed to have a consistent repeatability which is more reliable and not operator dependent.

The actuator design could be improved by using vented screws to fix the actuator wires into the blocks so that the tension can be easily adjusted in individual wires reducing errors in displacement. Further work can be performed such as the effect of using various cooling methods and comparing various control schemes to improve performance.

References

1. Mavroidis C, Pfeiffer C, Mosley M. Conventional Actuators, Shape Memory Alloys, and Electrorheological Fluids. New Jersey: Rutgers University, Department of Mechanical and Aerospace Engineering; 1999.
2. Nespoli A, Besseghini S, Pittaccio S, Villa E, Viscuso S. The High Potential of Shape Memory Alloys in Developing Miniature Mechanical Devices: A Review on Shape Memory Alloy Mini-Actuators. *Sensors and Actuators A: Physical*. 2010; 158: p. 149-160.
3. Van Humbeeck J, Cederstrom J. The Present State of Shape Memory Materials and Barriers Still to be Overcome. In *Proceedings of the 1st International Conference on Shape Memory and Superelastic Technologies (SMST-94)*; 1994; California, USA. p. 1-6.
4. Wu MH, Schetky L. Industrial Applications For Shape Memory Alloys. *Proceedings of the International Conference on Shape Memory and Superelastic Technologies*. 2000;; p. 171-182.
5. Srinivasan AV, McFarland DM. *Smart Structures: Analysis and Design* Cambridge: Cambridge University Press; 2001.
6. Lagoudas DC, editor. *Shape Memory Alloys: Modeling and Engineering Applications* New York: Springer; 2008.
7. Anadon JRS. *Large Force Shape Memory Alloy Linear Actuator*. Florida: University of Florida, Department of Mechanical and Aerospace Engineering; 2002.
8. Reynaerts D, Van Brussel H. Design Aspects of Shape Memory Actuators. *Mechatronics*. 1998; 8: p. 635-656.

9. Novotny M, Kilpi J. Shape Memory Alloys, Introduction. Helsinki: Institute of Automation and Control , Department of Automation Science and Engineering; 2006.
10. Ishii T. Combinations and Applications of Bias Method. In Proceedings of the International Conference on Shape Memory and Superelastic Technologies; 2007. p. 443-446.
11. Strittmatter J, Gumpel P. Shape Memory Actuator for Hydraulic Valve. In ACTUATOR 2004 9th International Conference on New Actuators; 2004.
12. Donellan QA, Lagoudas DC. Design and Testing of Linear Shape Memory Alloy Actuator. Texas: Texas A&M University, Aerospace Engineering Department; 2005.
13. Colli M, Bellini A, Concarì C, Toscani A, Franceschini G. Current-Controlled Shape Memory Alloy Actuators for Automotive Tumble Flap. In Industrial Electronics Conference; 2006; Paris.
14. Elwaleed AK, Mohamed NA, Mohd MJ, Mohd MM. A New Concept of a Linear Smart Actuator. Sensors and Actuators A. 2007; 123: p. 244-249.
15. Williams E, Shaw G, Elahinia M. Control of an Automotive Shape Memory Alloy Mirror Actuator. Mechatronics. 2010; 20: p. 527-534.
16. Pöhlau F, Meier H. Extremely Compact High-Torque Drive with Shape Memory Actuators and Strain Wave Gear Wave Drive. In ACTUATOR 2004 9th International Conference on New Actuators; 2004; Bremen.
17. Jansen S, Breidert J, Welp EG. Positioning Actuator Based on Shape Memory Wires. In ACTUATOR 2004 9th International Conference on New Actuators; 2004; Bremen.

18. Miga Motor Company. [Online].; 2011 [cited 2011 May. Available from: <http://www.migamotors.com>.
19. Shin W, Ro S, Park H, Park J. Development of a Micro/Meso-Tool Clamp Using a Shape Memory Alloy for Applications in Micro-Spindle Units. *International Journal of Machine Tools & Manufacture*. 2009; 49: p. 579-585.
20. Hollerbach JM, Hunter I, Ballantyne J. A Comparative Analysis of Actuator Technologies for Robotics. *The Robotics Review*. 1991; 2: p. 299-342.
21. Waram TC. *Actuator Design Using Shape Memory Alloys* Ontario: Hamilton; 1993.
22. Furuya Y, Shimada H. Shape Memory Actuator for Robotic Applications. *Materials and Design*. 1991; 12(1): p. 21-28.
23. Asada HH, Mascaro S. *Wet Shape Memory Alloy Actuators for Active Vasculated Robotic Flesh*. Cambridge: Massachusetts Institute of Technology, Department of Mechanical Engineering; 2002.
24. Romano R, Tannuri EA. Modeling, Control and Experimental Validation of a Novel Actuator Based on Shape Memory Alloys. *Mechatronics*. 2009; 19: p. 1169-1177.
25. Dynalloy. *Technical Characteristics of Flexinol Actuator Wires*. California;; 2010.
26. Tchoupo G, Leang KK. *Hysteresis Compensation for High-Precision Positioning of a Shape Memory Alloy*. Richmond: Virginia Commonwealth University, Department of Mechanical Engineering; 2007.

27. Sittner P, Vokoun D, Dayananda GN, Stalmans R. Recovery Stress Generation in Shape Memory TiNiCu Thin Wires. *Materials Science and Engineering A*. 2000; 286: p. 298-311.
28. Chirani SA, Aleong D, Dumont C, McDowell D, Patoor E. Superelastic Behavior Modeling In Shape Memory Alloys. *Journal of Physics IV*. 2003; 112: p. 205-208.
29. Bouvet C, Calloch S, Lexcellent C. A Phenomenological for Pseudoelasticity of Shape Memory Alloys Under Multiaxial Proportional and Nonproportional Loadings. *European Journal of Mechanics A/Solids*. 2004; 23: p. 37-61.
30. Gedouin P, Delaleau E, Bourgeot J, Join C, Chirani SA, Calloch S. Experimental Comparison of Classical PID and Model-Free Control: Position Control of a Shape Memory Alloy Active Spring. *Control Engineering Practice*. 2011; 19(5): p. 433–441.
31. Majima S, Kodama K, Hasegawa T. Modeling of a Shape Memory Alloy Actuator and Tracking Control System with the Model. *IEEE Transactions on Control Systems Technology*. 2001; 9: p. 54-59.
32. Ahn KK, Kha NB. Internal Model Control for Shape Memory Alloy Actuators Using Fuzzy Based Presaich Model. *Sensors and Actuators A*. 2007; 18: p. 141-152.
33. Dutta SM, Ghorbel FH, Dabney JB. Modeling and Control of a Shape Memory Actuator. *International Symposium on Intelligent Control*. 2005;; p. 1007-1012.
34. DaSilva EP. Beam Shape Feedback Control by Means of a Shape Memory Actuator. *Materials and Design*. 2007; 28: p. 1592-1596.

35. Calin M, Bertsch A, Chaillet N, Zissi S, Ballandras S, Andre JC. Microrobots Realized By Microstereophotolithography and Actuated by shape Memory Alloys. In Proceedings of the 1997 IEEE/RSJ Intelligent Robots and Systems; 1997; Grenoble, France. p. 33-34.

36. Ahn KK, Nguyen BK. Position Control of Shape Memory Alloy Actuators Using Self Tuning Fuzzy PID Controller. International Journal of Control, Automation, and Systems. 2006; 4(6): p. 756-762.

37. Gharaybeh MA, Burdea GC. Investigation of a Shape Memory Alloy Actuator for Dextrous Force-Feedback Masters. Advanced Robotics. 1995; 9(3): p. 317-329.

38. Liang C, Rogers CA. One Dimensional Thermomechanical Constitutive Relations for Shape Memory Materials. Journal of Intelligent Materials System and Structures. 1990; 1: p. 207-234.

39. Liang C. The Constitutive Modelling of Shape Memory Alloys. Blacksburg: Virginia Polytechnic Institute and State University, Department of Engineering Science and Mechanics; 1990.

40. Baldwin G. Metal Cutting and Turning Theory. In Geng H. Manufacturing Engineering Handbook. New York: McGraw-Hill; 2004. p. 27.3-27.42.

41. Bothner R. An Optimization Model for Selecting the Economical Cutting Parameters in an External Forward Turning Operation. New York: Rochester Institute of Technology, Department of Mechanical Engineering; 1990.

42. Johne P. Machining of Products. Dusseldorf: Aluminium-Zentrale e.V.; 1994.

43. Marandet B, Verquin B, Saint-Chely J, Anderson C, Ryckeboer M. aluMATTER Website. [Online].; 2010 [cited 2011 May 16. Available from:

<http://aluminium.matter.org.uk/content/html/eng/default.asp?catid=128&pageid=2144416321>.

44. Sandvik. Dormer Tools Website. [Online].; 2010 [cited 2011 April. Available from: <http://www.dormertools.com/sandvik/2531/internet/s003591.nsf?OpenDatabase>.
45. Kalpakjian S, Schmid SR. Manufacturing Processes for Engineering Materials New Jersey: Prentice Hall; 2003.
46. Krar SF, Gill AR, Smid P. Technology of Machine Tools New York: McGraw-Hill; 2005.
47. Walsh RA. Machining and Metalworking Handbook New York: McGraw-Hill; 2006.
48. Mosley MJ, Mavroidis C, Pfeiffer C. Design And Dynamics of a Shape Memory Alloy Wire Bundle Actuator. New Jersey: Rutgers University, Department of Mechanical and Aerospace Engineering; 1999.
49. Stabilus. Standard Lift-O-Mat. Koblenz.; 2010.
50. Gere JM. Mechanics of Materials Toronto: Thomson; 2006.
51. Labview PID and Fuzzy Logic Toolkit User Manual. Austin: National Instruments; 2009.

Appendix A: Labview Programs

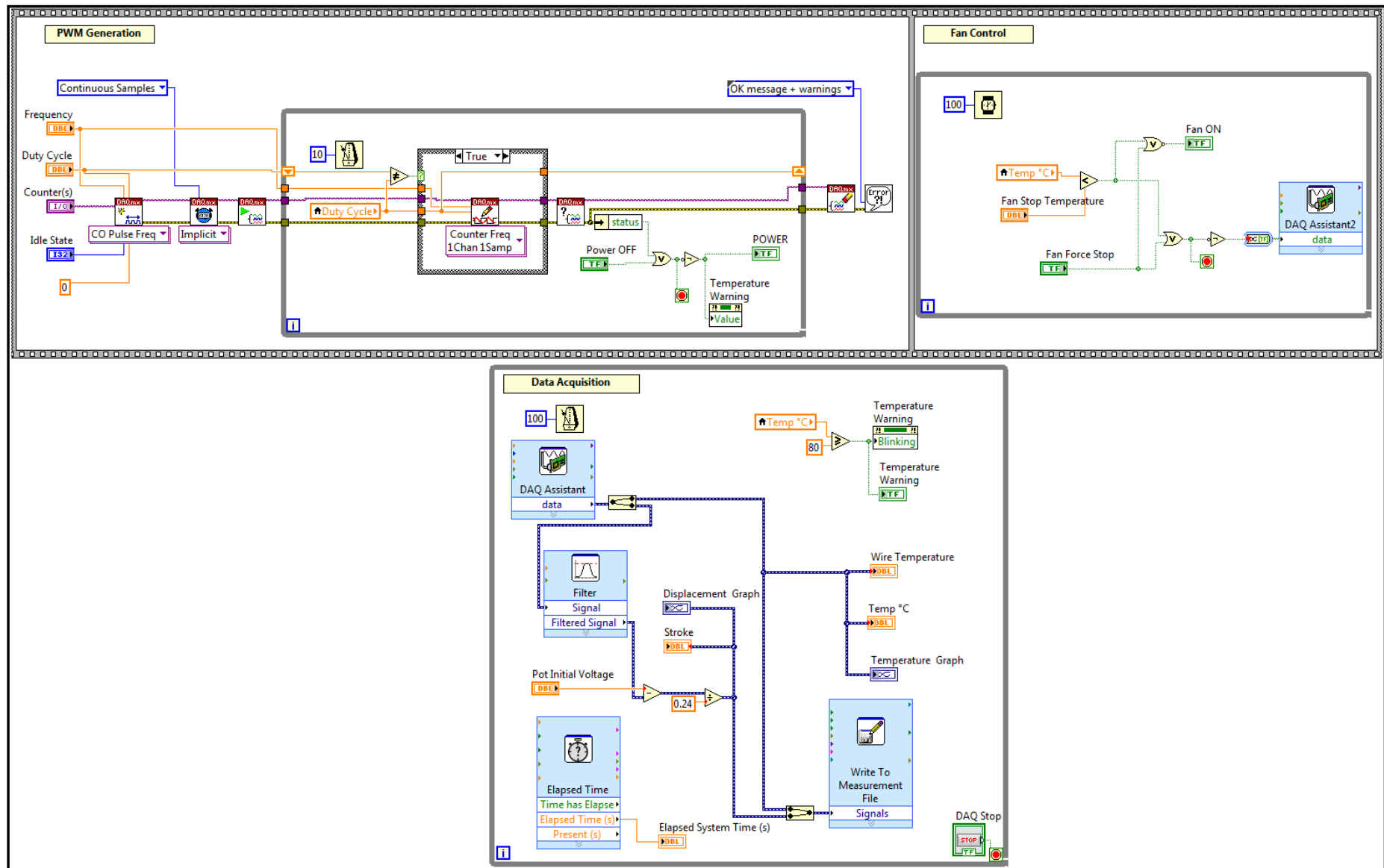


Figure A.1: Open loop block diagram

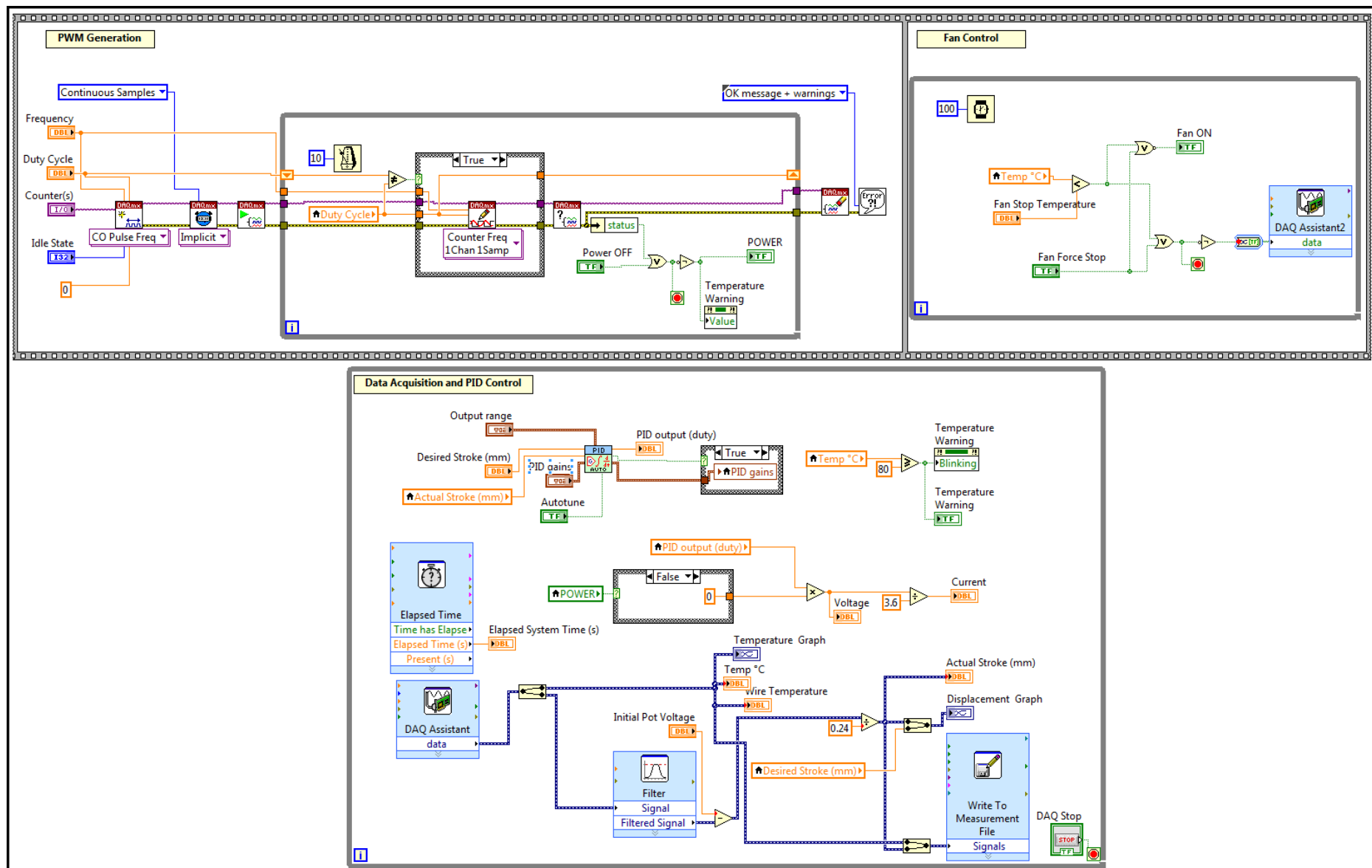
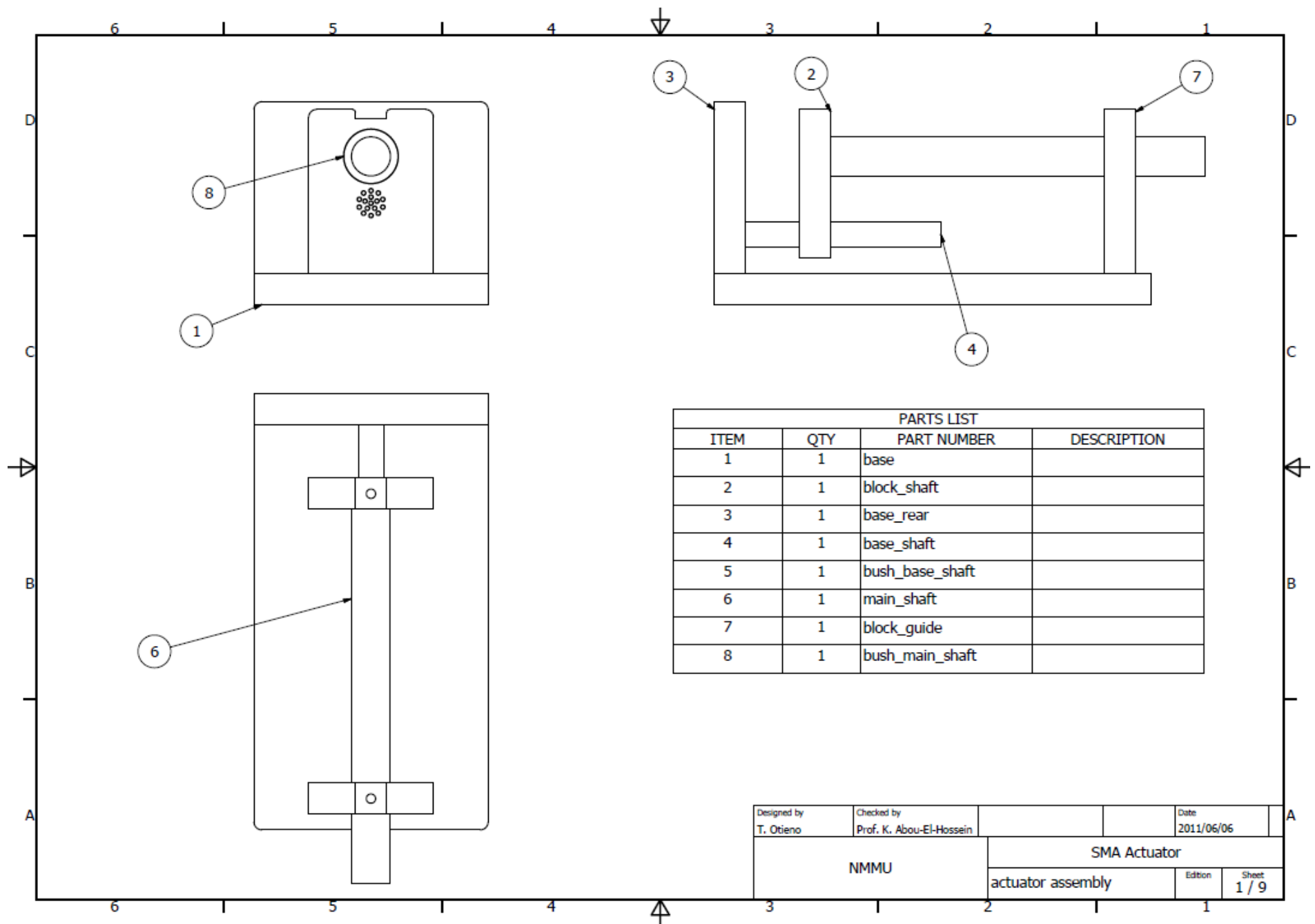
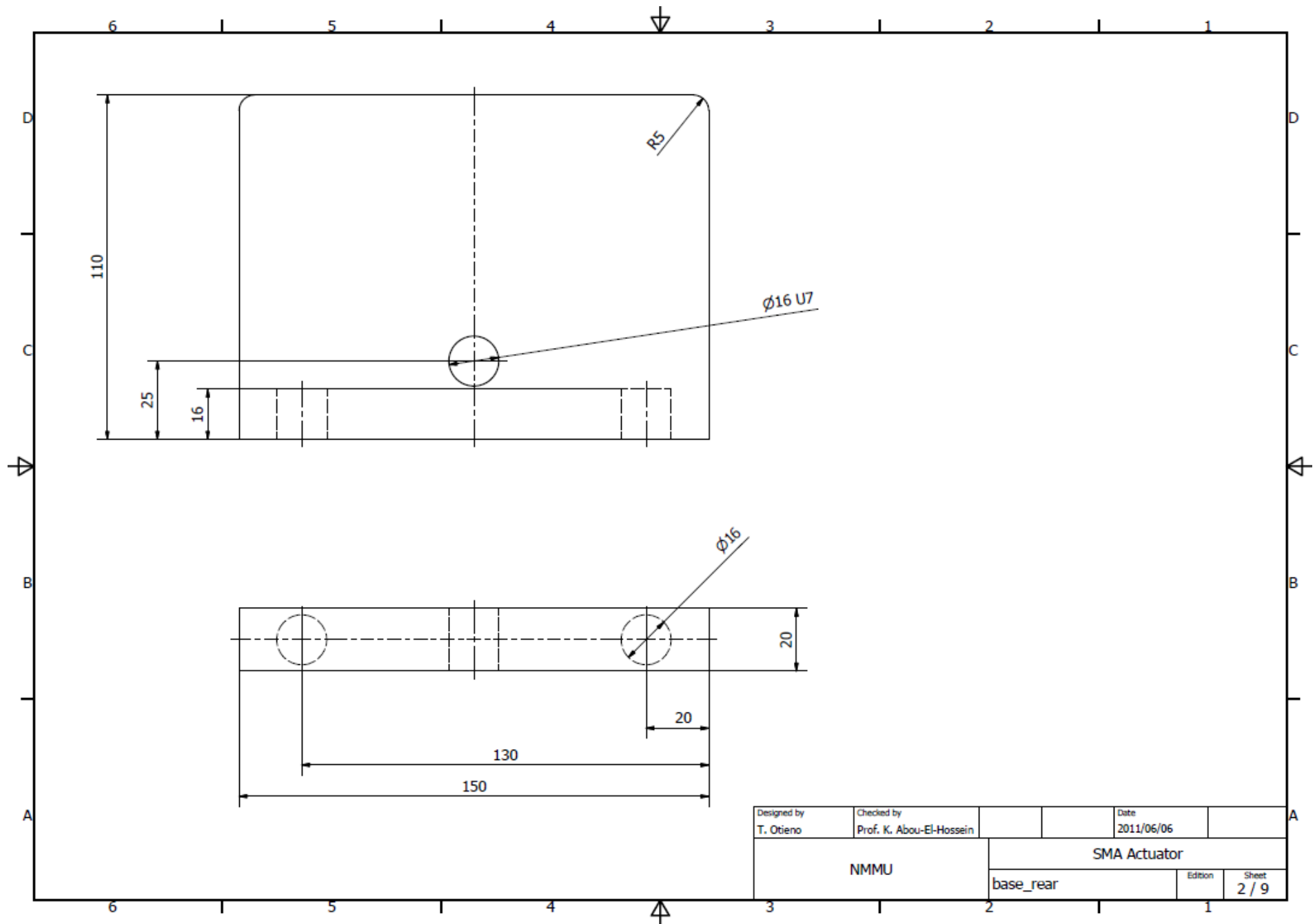
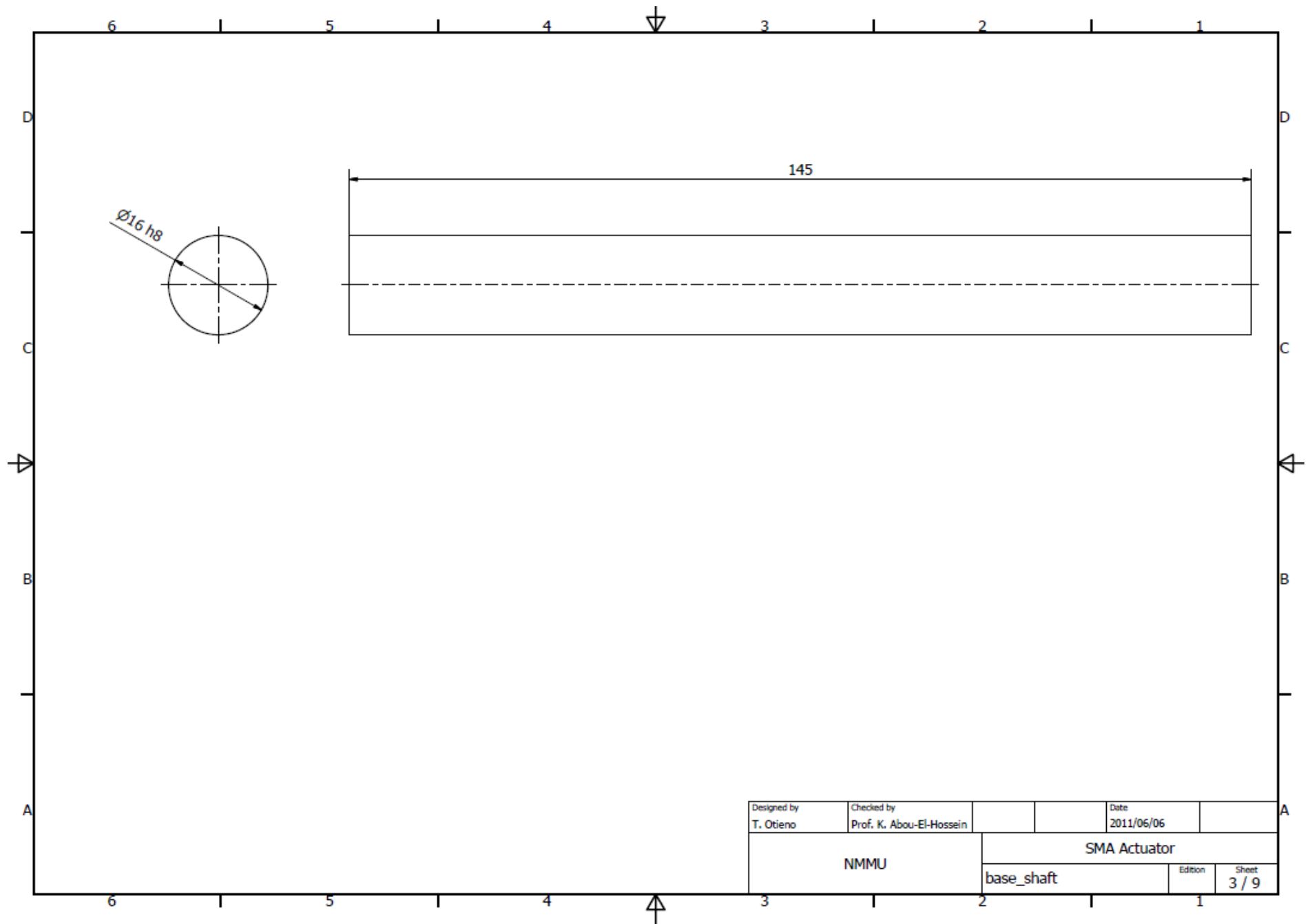


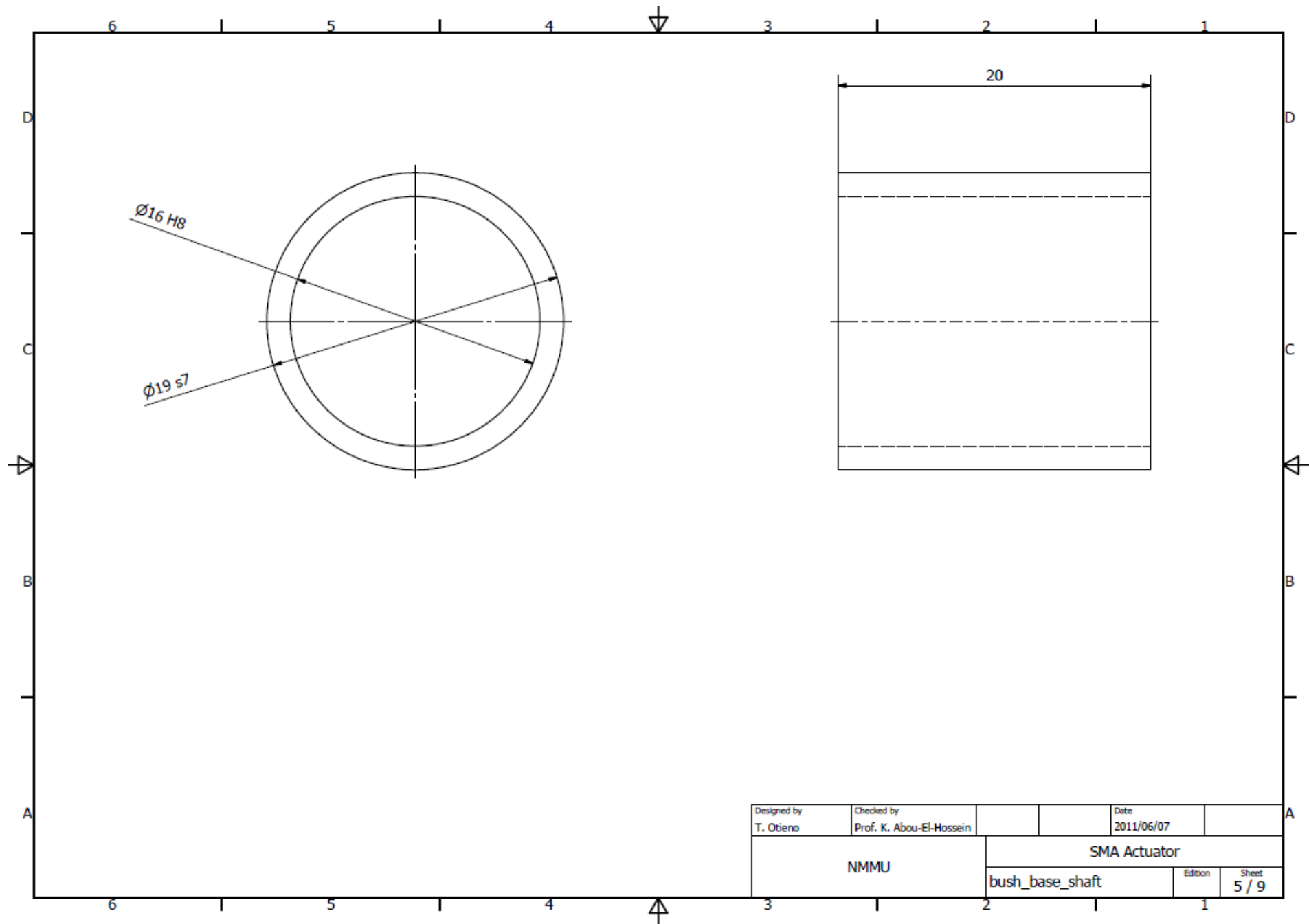
Figure A.2: Closed loop block diagram

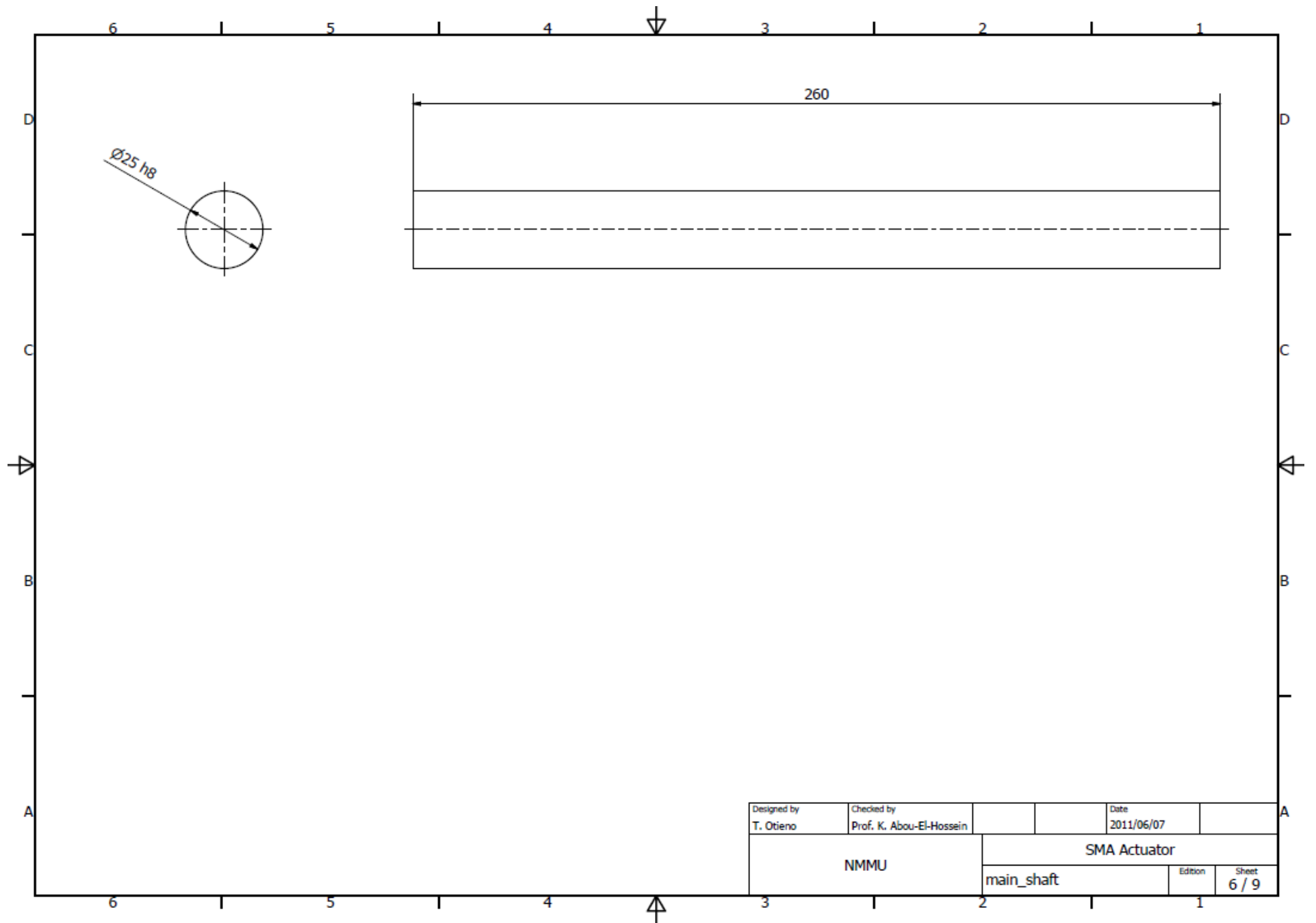
Appendix B: Drawings

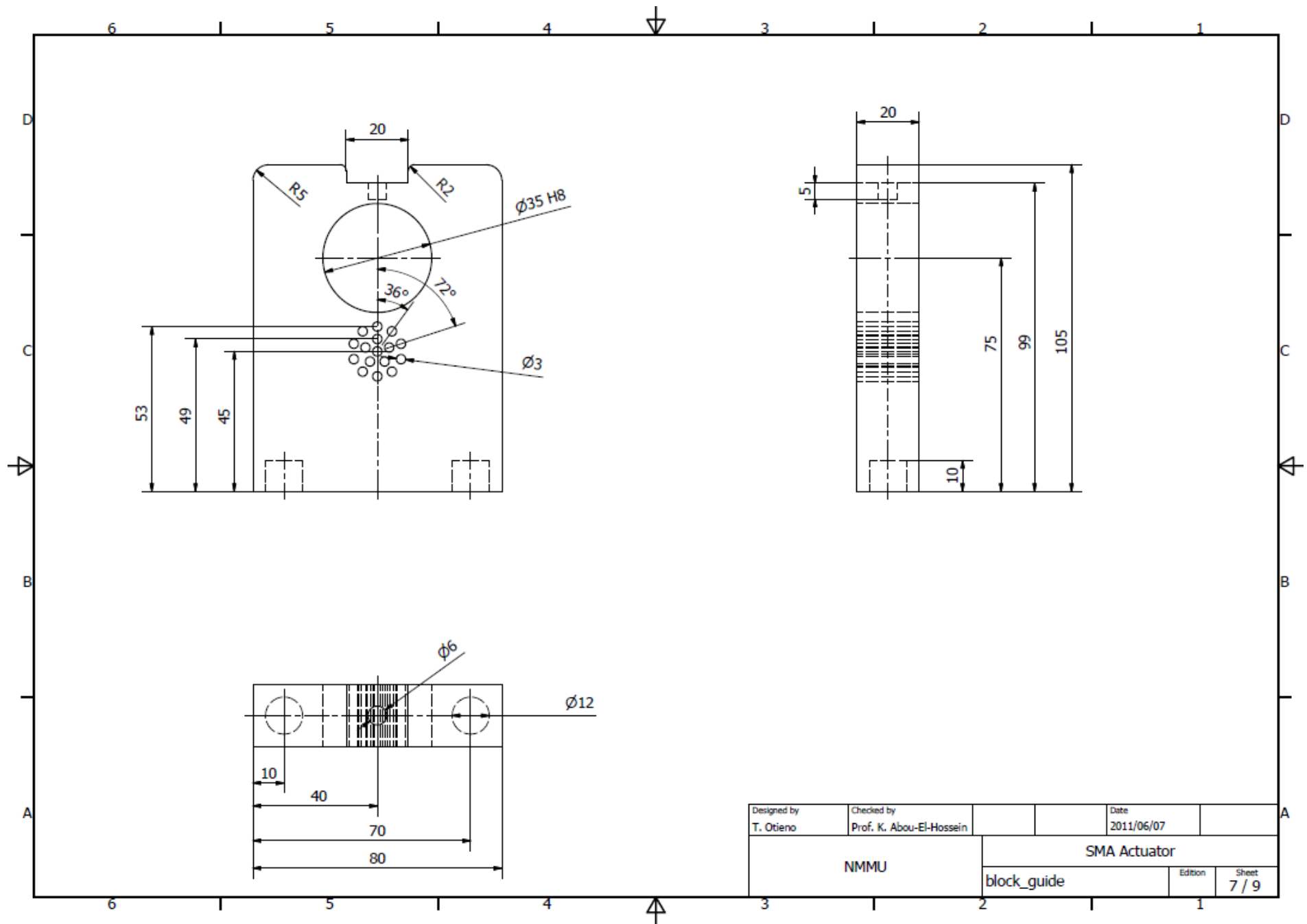


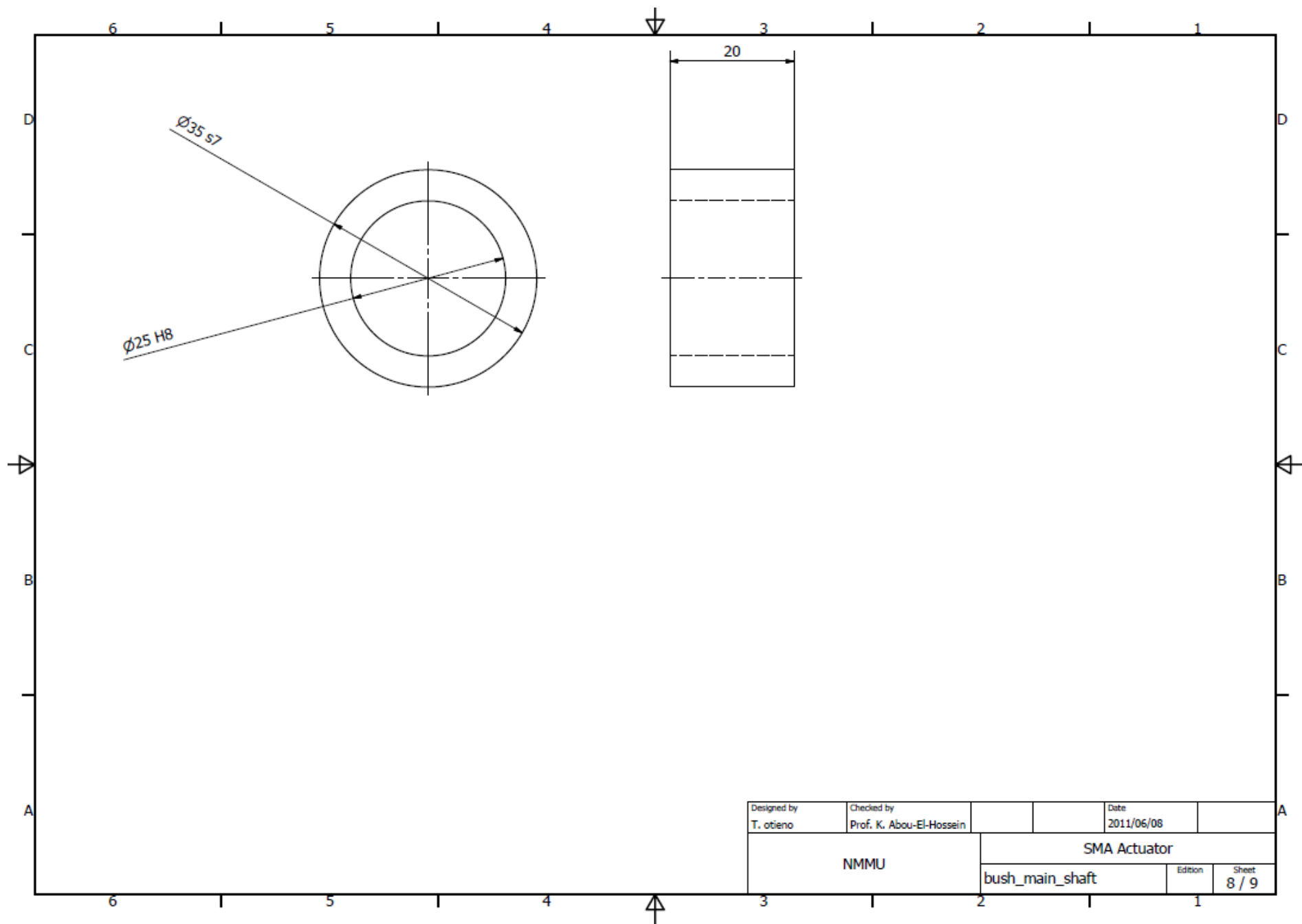












Appendix C: Finite Element Analysis Report

Material Properties

Name	Steel, Mild	
General	Mass Density	7.86 g/cm ³
	Yield Strength	207 MPa
	Ultimate Tensile Strength	345 MPa
Stress	Young's Modulus	220 GPa
	Poisson's Ratio	0.275
	Shear Modulus	86.2745 GPa
Stress Thermal	Expansion Coefficient	0.000012 1/c
	Thermal Conductivity	56 W/(m K)
	Specific Heat	460 J/(kg c)
Part Name(s)	block_shaft.ipt	

Operating Conditions

Force 1

Load Type	Force
Magnitude	120.000 N
Vector X	120.000 N
Vector Y	0.000 N

Force 2

Load Type	Force
Magnitude	50.000 N
Vector X	-50.000 N
Vector Y	0.000 N

Force 3

Load Type	Force
Magnitude	341.078 N
Vector X	-75.000 N
Vector Y	-150.000 N
Vector Z	-297.000 N

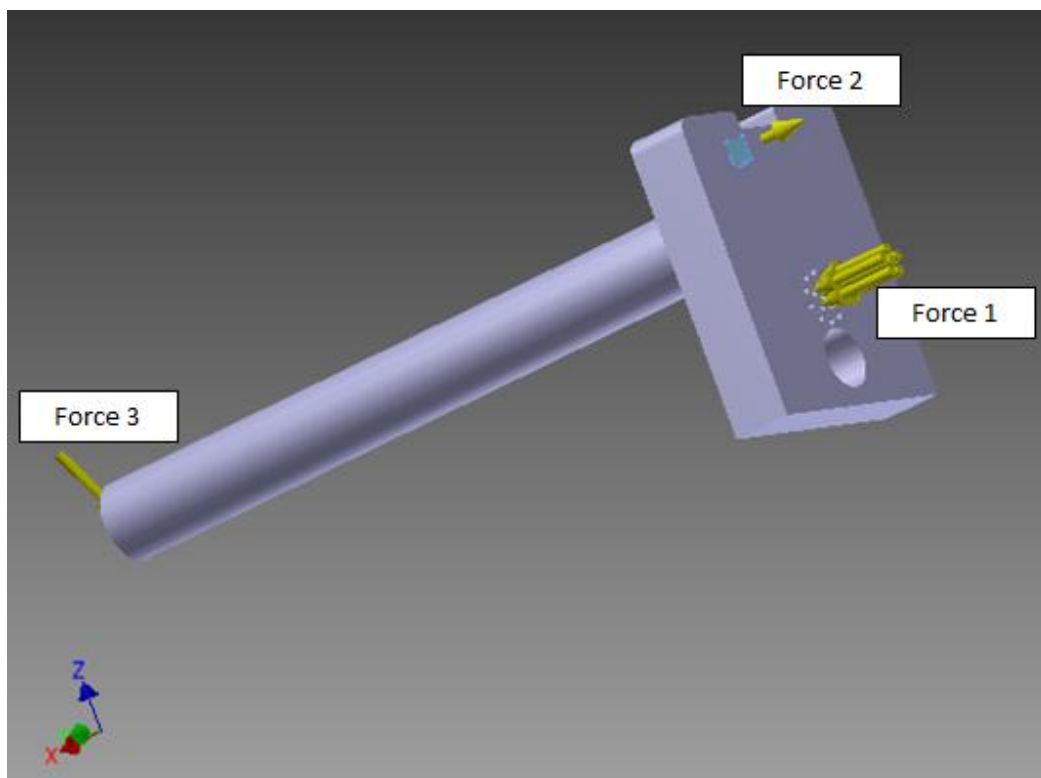


Figure C.1: FEA applied forces

Constraints

Constraint 1

Constraint Type	Pin Constraint
Fix Radial Direction	Yes
Fix Axial Direction	No
Fix Tangential Direction	Yes

Constraint 2

Constraint Type	Pin Constraint
Fix Radial Direction	No
Fix Axial Direction	Yes
Fix Tangential Direction	Yes

Constraint 3

Constraint Type	Pin Constraint
Fix Radial Direction	No
Fix Axial Direction	Yes
Fix Tangential Direction	Yes

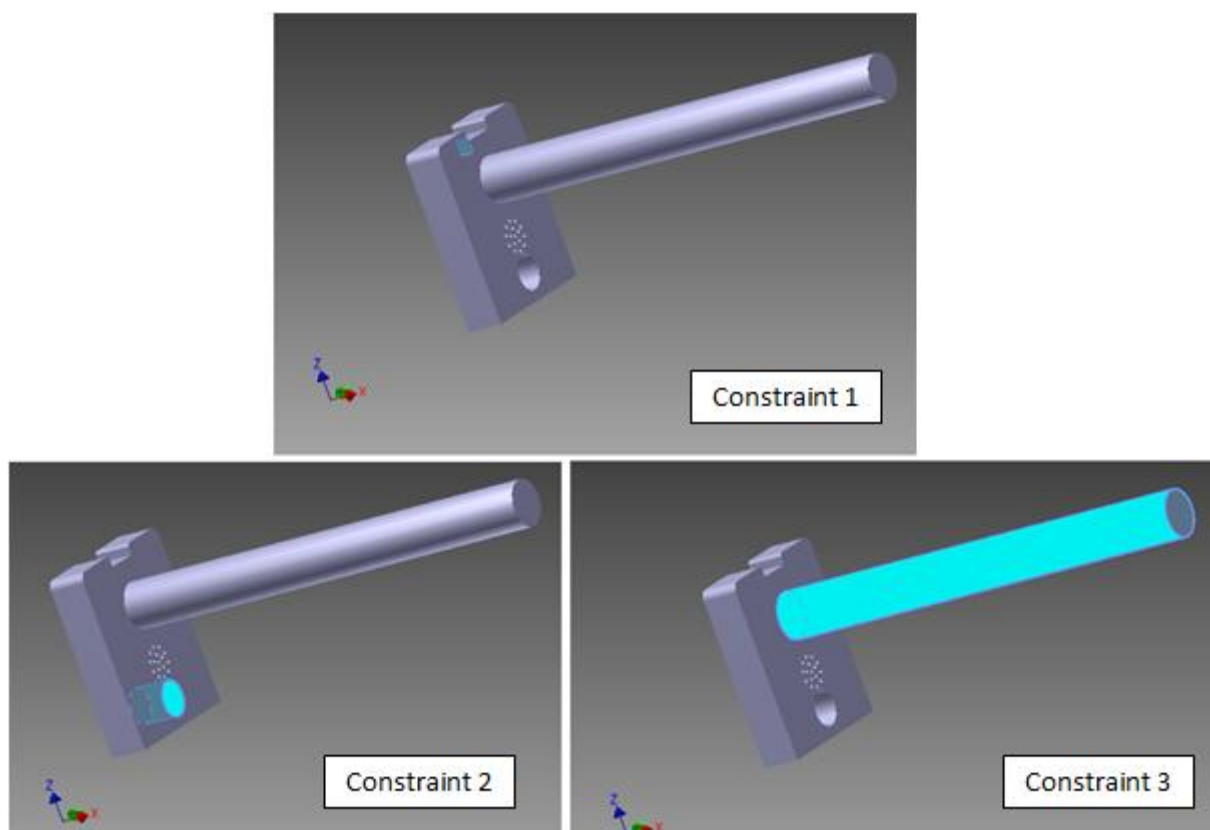


Figure C.2: FEA applied constraints

Results

Reaction Force and Moment on Constraints

Constraint Name	Reaction Force		Reaction Moment	
	Magnitude	Component (X,Y,Z)	Magnitude	Component (X,Y,Z)
Pin Constraint:1	50.9942 N	50.9942 N	0.000347451 N m	0 N m
		0 N		0.000347451 N m
		0 N		0 N m
Pin Constraint:2	12.6943 N	-12.4845 N	0.1279 N m	-0.000173029 N m
		0.0215982 N		-0.1279 N m
		2.2982 N		-0.00013177 N m
Pin Constraint:3	337.325 N	66.533 N	40.1251 N m	0 N m
		149.997 N		-35.8594 N m
		294.725 N		18.0034 N m

Result Summary

Name	Minimum	Maximum
Volume	259002 mm ³	
Mass	2.03576 kg	
Von Mises Stress	0.000000443435 MPa	5.71168 MPa
Displacement	0.000000000000751689 mm	0.0000970253 mm
Safety Factor	15 ul	15 ul
Equivalent Strain	0.00000000000175888 ul	0.0000221322 ul

Von Mises Stress

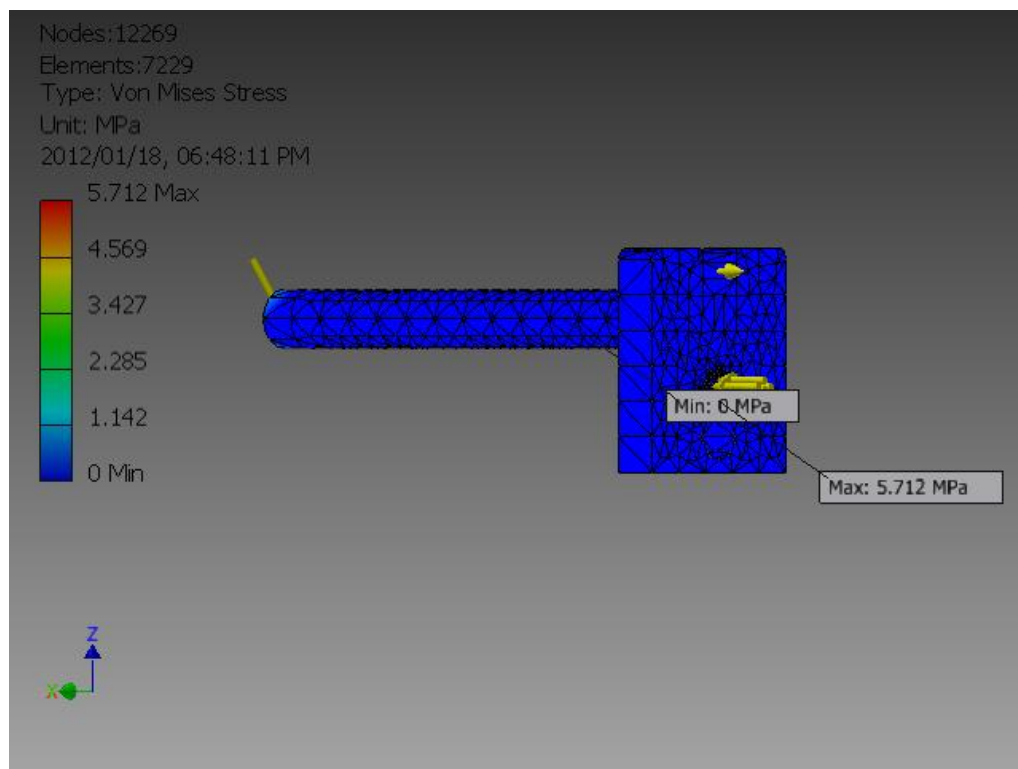


Figure C.3: FEA Von Mises stress results

Displacement

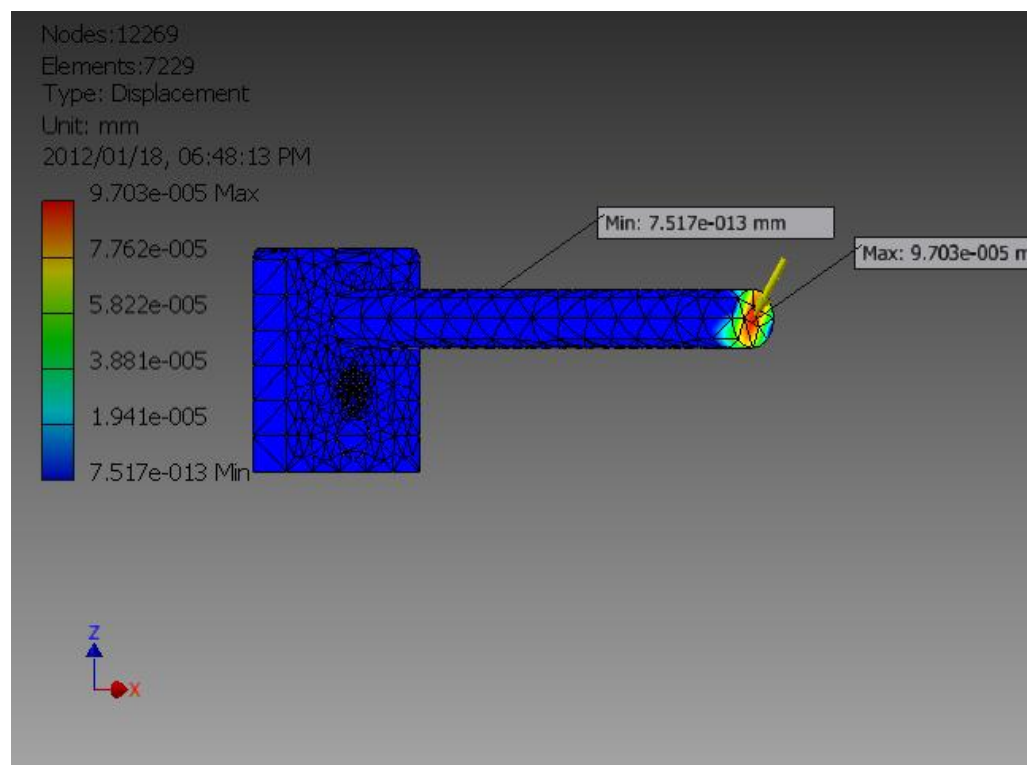


Figure C.4: FEA displacement results

Equivalent Strain

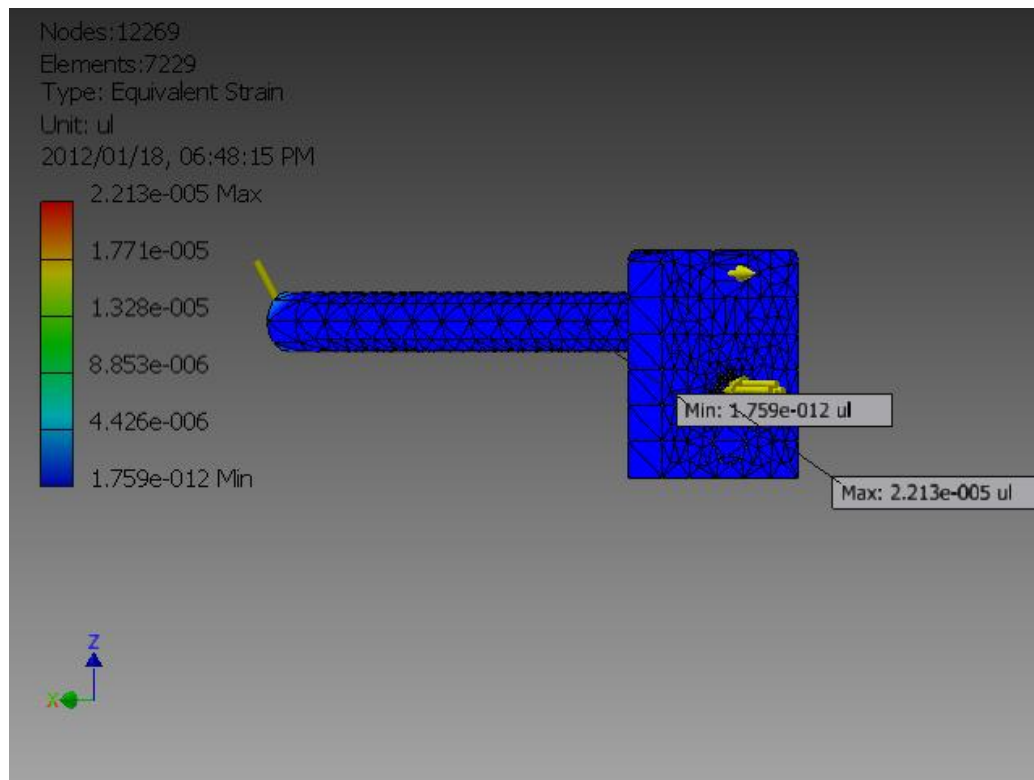


Figure C.5: FEA strain results